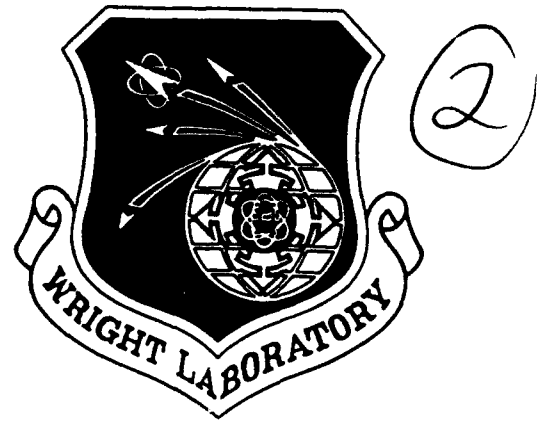


AD-A277 563



WL-TR-93-3097

METHOD FOR TRANSITION PREDICTION
IN HIGH-SPEED BOUNDARY LAYERS



TH. HERBERT
G. K. STUCKERT
N. LIN

DYNAFLOW, INC.
3040 RIVERSIDE DRIVE
COLUMBUS OH 43221

DTIC
ELECTE
MAR 29 1994
S F D

September 1993

Final Report for 09/27/90 - 09/27/93

Approved for public release; distribution is unlimited

94-09541



FLIGHT DYNAMICS DIRECTORATE
WRIGHT LABORATORY
AIR FORCE MATERIEL COMMAND
WRIGHT-PATTERSON AFB OH 45433-7562

DTIC

94 3 28 101

NOTICE

When Government drawings, specifications, or other data are used for any purpose other than in connection with a definitely Government-related procurement, the United States Government incurs no responsibility or any obligation whatsoever. The fact that the government may have formulated or in any way supplied the said drawings, specifications, or other data, is not to be regarded by implication, or otherwise in any manner construed, as licensing the holder, or any other person or corporation; or as conveying any rights or permission to manufacture, use, or sell any patented invention that may in any way be related thereto.

This report is releasable to the National Technical Information Service (NTIS). At NTIIS, it will be available to the general public, including foreign nations.

This technical report has been reviewed and is approved for publication.

Roger Kimmel
Roger Kimmel, Program Monitor
Aerothermodynamic Res Section
Aerothermodynamics & Flight Mech
Research Branch

Valentine Dahlem
Valentine Dahlem, Chief
Aerothermodynamics & Flight Mech
Research Branch

Dennis Sedlock
Dennis Sedlock, Actg Chief
Aeromechanics Division

If your address has changed, if you wish to be removed from our mailing list, or if the addressee is no longer employed by your organization, please notify WL/FIMH, WPAFB, OH 45433-7936 to help us maintain a current mailing list.

Copies of this report should not be returned unless return is required by security considerations, contractual obligations, or notice on a specific document.

REPORT DOCUMENTATION PAGE

Form Approved
OMB No. 0704-0188

Public reporting burden for this collection of information is estimated to average 1 hour per response, including the time for reviewing instructions, searching existing data sources, gathering and maintaining the data needed, and completing and reviewing the collection of information. Send comments regarding this burden estimate or any other aspect of this collection of information, including suggestions for reducing this burden, to Washington Headquarters Services, Directorate for Information Operations and Reports, 1215 Jefferson Davis Highway, Suite 1204, Arlington, VA 22202-4302, and to the Office of Management and Budget, Paperwork Reduction Project (0704-0188), Washington, DC 20503.

1. AGENCY USE ONLY (Leave blank)			2. REPORT DATE SEP 1993	3. REPORT TYPE AND DATES COVERED FINAL 09/27/90-09/27/93
4. TITLE AND SUBTITLE METHOD FOR TRANSITION PREDICTION IN HIGH-SPEED BOUNDARY LAYERS			5. FUNDING NUMBERS C F33615-90-C-3009 PE 62201 PR 2404 TA 07 WU B3	
6. AUTHOR(S) TH. HERBERT G. K. STUCKERT N. LIN			8. PERFORMING ORGANIZATION REPORT NUMBER	
7. PERFORMING ORGANIZATION NAME(S) AND ADDRESS(ES) DYNALFLOW, INC. 3040 RIVERSIDE DRIVE COLUMBUS OH 43221			9. SPONSORING / MONITORING AGENCY NAME(S) AND ADDRESS(ES) FLIGHT DYNAMICS DIRECTORATE WRIGHT LABORATORY AIR FORCE MATERIEL COMMAND WRIGHT PATTISON AFB OH 45433-7562	
10. SPONSORING / MONITORING AGENCY REPORT NUMBER WL-TR-93-3097				
11. SUPPLEMENTARY NOTES THIS IS A SMALL BUSINESS INNOVATION RESEARCH REPORT, PHASE 2				
12a. DISTRIBUTION / AVAILABILITY STATEMENT APPROVED FOR PUBLIC RELEASE; DISTRIBUTION UNLIMITED			12b. DISTRIBUTION CODE	
13. ABSTRACT (Maximum 200 words) The parabolized stability equations (PSE) are a new and more reliable approach to analyzing the stability of streamwise varying flows such as boundary layers. This approach has been previously validated for idealized incompressible flows. Here, the PSE are formulated for highly compressible flows in general curvilinear coordinates to permit the analysis of high-speed boundary-layer flows over fairly general bodies. Vigorous numerical studies are carried out to study convergence and accuracy of the linear-stability code LSH, and the linear/nonlinear PSE code, PSH. Physical interfaces are set up to analyze the $M_\infty = 8$ boundary layer over a blunt cone calculated by using a thin-layer Navier Stokes (TNLS) code, and the flow over a sharp cone at angle of attack calculated using the AFWAL Parabolized Navier-Stokes (PNS) code. While stability and transition studies at high speeds are far from routine, the method developed here is the best tool available to research the physical processes in high-speed boundary layers.				
14. SUBJECT TERMS PARABOLIZED STABILITY EQUATIONS COMPRESSIBLE FLOWS HIGH-SPEED BOUNDARY LAYERS GENERAL BODIES			15. NUMBER OF PAGES 102	
16. PRICE CODE				
17. SECURITY CLASSIFICATION OF REPORT UNCLASSIFIED	18. SECURITY CLASSIFICATION OF THIS PAGE UNCLASSIFIED	19. SECURITY CLASSIFICATION OF ABSTRACT UNCLASSIFIED	20. LIMITATION OF ABSTRACT UL	

Contents

1	Introduction	1
2	PSE Methodology	4
2.1	Nondimensionalizations	5
2.2	Navier-Stokes Equations	6
2.3	Disturbance Equations	6
2.4	Transformation of the Independent and Dependent Variables	8
2.5	Nonlinear Terms and Modal Decomposition	9
2.6	PSE Approximation	10
2.7	Constitutive Equations	12
2.8	Boundary Conditions and Initial Conditions	12
2.9	Numerical Method	13
3	Compressible Boundary Layer over the Flat Plate	14
3.1	Basic State Similarity Solution	15
3.1.1	Governing Equations and Similarity Transformation	15
3.2	Stability Analysis	18
3.2.1	Coordinate Systems	18
3.2.2	Dependent Disturbance State Variables	22
3.2.3	Basic State for Parallel and Quasi-Parallel Flows	24
3.2.4	Computed Results	31
3.2.5	Linear PSE	35
3.2.6	Nonlinear PSE	36
3.3	Summary	38
4	Hypersonic Flow over a Sharp Cone at Angle of Attack	40
4.1	Mean Flow Calculation	40
4.1.1	Coordinate System	41
4.1.2	Initial Conditions	41
4.1.3	Basic State Results	42
4.2	Disturbance Coordinate System	43
4.3	Local Linear Stability Analyses	43
4.3.1	Windward Meridian	43
4.3.2	Leeward Meridian	45
4.4	Linear PSE Analyses	45
4.4.1	Windward Meridian	45

4.4.2 Leeward Meridian	46
4.5 Summary	46
5 Hypersonic Flow over a Blunt Cone	57
5.1 Mean Flow Calculation	57
5.2 Reference Scales for Stability Analysis	65
5.3 Stability Analysis Coordinates	65
5.4 Dependent Variables	67
5.5 Linear Stability Analysis	67
5.6 Results of Linear PSE	72
5.7 Results of Nonlinear PSE	79
5.7.1 2D waves	79
5.7.2 3D waves	83
6 Concluding Remarks	89
7 References	91

Accession For	
NTIS CRA&I	<input checked="" type="checkbox"/>
DTIC TAG	<input type="checkbox"/>
Unannounced	<input type="checkbox"/>
Justification	
By	
Distribution /	
Availability Codes	
Dist	Avail and/or Special
A-1	

List of Figures

3.1	Root Mean Square of Disturbance Tangential Velocity Component as a Function of the Local Reynolds Number	37
3.2	Spatial Growth Rate at Maximum in rms Profiles. Amplitude of primary disturbance at neutral point = 0.1%. Frequency $F = 60$, spanwise wavenumber $b = 0.15$. \square : PSE primary mode (2,0), \diamond : PSE subharmonic mode (1,1). Solid line: Cartesian coordinates. Dashed line: similarity coordinates. \times : El-Hady (1991) primary mode (2,0), $*$: El-Hady (1991) subharmonic mode (1,1).	38
3.3	Spatial Growth Rate at Maximum in rms Profiles. Amplitude of primary disturbance at neutral point = 0.1%. Frequency $F = 60$, spanwise wavenumber $b = 0.15$. \square : PSE Primary mode (2,0), \diamond : PSE Subharmonic mode (1,1). Solid line: Cartesian coordinates. Dashed line: similarity coordinates. \times : El-Hady (1991) primary mode (2,0), $*$: El-Hady (1991) subharmonic mode (1,1).	39
4.1	Coordinate System Used in the Stability Analyses.	41
4.2	AFWAL PNS Basic State Profiles of the Flow Over a Sharp, 7° Half-Angle Cone at 2° Angle of Attack. Windward meridian, $R = 746$ (interpolated). Bow shock at $\xi^2 = 26.7$. a) Density. b) ξ^1 contravariant velocity component. c) Temperature. d) ξ^2 contravariant velocity component x 100.	47
4.3	AFWAL PNS Basic State Profiles of the Flow Over a Sharp, 7° Half-Angle Cone at 2° Angle of Attack. First derivatives with respect to ξ^2 , windward meridian, $R = 746$ (interpolated). Bow shock at $\xi^2 = 26.7$. a) Density. b) ξ^1 contravariant velocity component. c) Temperature. d) ξ^2 contravariant velocity component x 100.	48
4.4	AFWAL PNS Basic State Profiles of the Flow Over a Sharp, 7° Half-Angle Cone at 2° Angle of Attack. Second derivatives with respect to ξ^2 , windward meridian, $R = 746$ (interpolated). Bow shock at $\xi^2 = 26.7$. a) Density. b) ξ^1 contravariant velocity component. c) Temperature. d) ξ^2 contravariant velocity component x 100.	49
4.5	AFWAL PNS Basic State Profiles of the Flow Over a Sharp, 7° Half-Angle Cone at 2° Angle of Attack. Leeward meridian, $R = 712$ (interpolated). Bow shock at $\xi^2 = 37.44$. a) Density. b) ξ^1 contravariant velocity component. c) Temperature. d) ξ^2 contravariant velocity component x 100.	50

4.6 AFWAL PNS Basic State Profiles of the Flow Over a Sharp, 7° Half-Angle Cone at 2° Angle of Attack. First derivatives with respect to ξ^2 , leeward meridian, $R = 712$ (interpolated). Bow shock at $\xi^2 = 37.44$. a) Density. b) ξ^1 contravariant velocity component. c) Temperature. d) ξ^2 contravariant velocity component x 100.	51
4.7 AFWAL PNS Basic State Profiles of the Flow Over a Sharp, 7° Half-Angle Cone at 2° Angle of Attack. Second derivatives with respect to ξ^2 , leeward meridian, $R = 712$ (interpolated). Bow shock at $\xi^2 = 37.44$. a) Density. b) ξ^1 contravariant velocity component. c) Temperature. d) ξ^2 contravariant velocity component x 100.	52
4.8 Comparison of Spatial Growth Rates of 70 kHz Disturbance Along Windward Meridian. $\beta = 0$, length scale = $x^1/\sqrt{Re_{x^1}}$. \square Physical velocity components (parallel), \diamond Physical mass fluxes (parallel), \triangle Physical velocity components (quasi-parallel), ∇ Physical mass fluxes (quasi-parallel).	53
4.9 Comparison of Spatial Growth Rates of 70 kHz Disturbance Along Windward Meridian. Physical components, locally parallel flow, $\beta = 0$, length scale = $x^1/\sqrt{Re_{x^1}}$, fifth order interpolants in ξ^2 . Solid line: First order interpolants in ξ^1 and ξ^3 ; Dashed line: Third order interpolants in ξ^1 and ξ^3 ; Dot-dashed line: Fifth order interpolants in ξ^1 and ξ^3	53
4.10 Comparison of Spatial Growth Rates of 70 kHz Disturbance Along Windward Meridian. Physical components, quasi-parallel flow, $\beta = 0$, length scale = $x^1/\sqrt{Re_{x^1}}$, fifth order interpolants in ξ^2 . \square) First order interpolants in ξ^1 and ξ^3 , \diamond) Third order interpolants in ξ^1 and ξ^3 , \triangle) Fifth order interpolants in ξ^1 and ξ^3	54
4.11 Comparison of Spatial Growth Rates of 70 kHz Disturbance Along Windward Meridian. Physical components, quasi-parallel flow, $\beta = 0$, length scale = $x^1/\sqrt{Re_{x^1}}$, fifth order interpolants in ξ^2 . Solid line: First order interpolants in ξ^1 and ξ^3 ; Dashed line: Third order interpolants in ξ^1 and ξ^3 ; Dot-dashed line: Fifth order interpolants in ξ^1 and ξ^3	54
4.12 Comparison of Spatial Growth Rates of 30 kHz Disturbance Along Leeward Meridian. $\beta = 0$, length scale = $x^1/\sqrt{Re_{x^1}}$. \square Physical velocity components (parallel), \diamond Physical mass fluxes (parallel), \triangle Physical velocity components (quasi-parallel), ∇ Physical mass fluxes (quasi-parallel).	55
4.13 Comparison of Spatial Growth Rates of 70 kHz Disturbance Along Windward Meridian. $\beta = 0$, length scale = $x^1/\sqrt{Re_{x^1}}$. Dotted lines: locally parallel basic state. Solid lines: nonparallel basic state. \square) Physical velocity components, \diamond) Physical mass fluxes.	55
4.14 Comparison of Spatial Growth Rates of 70 kHz Disturbance Along Windward Meridian. $\beta = 0$, length scale = $x^1/\sqrt{Re_{x^1}}$. Solid lines: local analyses. Dot-dashed lines: linear PSE analyses. \square) Physical velocity components, \diamond) Physical mass fluxes.	56

4.15 Comparison of Spatial Growth Rates of 30 kHz Disturbance Along Leeward Meridian. $\beta = 0$, length scale = $x^1/\sqrt{Re_x}$. \square) Physical velocity components, local, \diamond) Physical mass fluxes, local, \triangleleft) Physical velocity components, PSE.	56
5.1 Comparison of TLNS and AFWAL PNS Basic State Profiles of the Flow Over a Blunt, 7° Half-Angle Cone. $s/R_N = 175$ (interpolated). Bow shock at $\xi^2 \approx 150$. Solid line: TLNS solution. Dotted line: AFWAL PNS solution. a) Density. b) ξ^1 contravariant velocity component. c) Temperature. d) ξ^2 contravariant velocity component x 100.	59
5.2 Comparison of TLNS and AFWAL PNS Basic State Profiles of the Flow Over a Blunt, 7° Half-Angle Cone. $s/R_N = 175$ (interpolated). Bow shock at $\xi^2 \approx 150$. First derivatives with respect to ξ^2 . Solid line: TLNS solution. Dotted line: AFWAL PNS solution. a) Density. b) ξ^1 contravariant velocity component. c) Temperature. d) ξ^2 contravariant velocity component x 100.	60
5.3 Comparison of TLNS and AFWAL PNS Basic State Profiles of the Flow Over a Blunt, 7° Half-Angle Cone. $s/R_N = 175$ (interpolated). Bow shock at $\xi^2 \approx 150$. Second derivatives with respect to ξ^2 . Solid line: TLNS solution. Dotted line: AFWAL PNS solution. a) Density. b) ξ^1 contravariant velocity component. c) Temperature. d) ξ^2 contravariant velocity component x 100.	61
5.4 Temperature Along the Cone Surface.	62
5.5 Basic State Streamwise Velocity Profiles at $s^*/R_N = 128$ and 94. . .	63
5.6 Shock Shape Comparison with Billig's Correlation and the STDS Experiment.	64
5.7 Body-Intrinsic Coordinate System Used for Stability Analysis	66
5.8 Families of Eigensolutions at Station $s^*/R_N = 175$	68
5.9 Amplitude Profiles of the Eigensolution at Station $s^*/R_N = 175$ and $F \times 10^6 = 82.7$	69
5.10 Growth Rate Variation with Frequency at $s^*/R_N = 175$	69
5.11 Comparison of Computed Spatial Growth Rates as a Function of Surface Arc Length Using Two Different Basic State Solutions. $F = 82.7$. \square) TLNS solution, 200 wall normal points. \diamond) AFWAL PNS solution, 501 radial points. \triangle) AFWAL PNS solution, 251 radial points.	71
5.12 Effect of Curvature on Second-Mode Growth Rate Variation with R at $F \times 10^6 = 82.7$	71
5.13 Effect of Nonparallel Basic State on Second-Mode Growth Rate Variation with R at $F \times 10^6 = 82.7$	72
5.14 Second-Mode Growth Rate Variation with R at Different Frequencies.	73
5.15 Wave Speed Variation with R at Different Frequencies.	73
5.16 N-Factor Variation with R at Different Frequencies.	74
5.17 Second-Mode Growth Rate Variation with R for Different Azimuthal Wavenumbers.	74

5.18 Neutral Stability Curve for Second-Mode 2D Disturbances.	75
5.19 Variation of Growth Rate of Maximum u with R at Different Frequencies.	76
5.20 Variation of Maximum Amplitude of u with R at Different Frequencies.	76
5.21 Profiles of Amplitude and Growth Rate of Massflow Fluctuations at $R = 2309, F \times 10^6 = 82.7$	77
5.22 Variation of Growth Rates with R at $F \times 10^6 = 100$	78
5.23 Variation of Maximum Amplitude of m with R at Different Frequencies.	79
5.24 Evolution of Maximum Amplitude with R for Different Variables at $F \times 10^6 = 100$	80
5.25 Variation of Amplitude of \tilde{u} with R for the Initial Amplitude of 10^{-4}	80
5.26 Variation of Amplitude of \tilde{u} with R for the Initial Amplitude of 2×10^{-4}	81
5.27 Variation of Amplitude of \tilde{u} with R for the Initial Amplitude of 4×10^{-4}	81
5.28 Variation of Growth Rates of \tilde{m} with R for the Initial \tilde{u} Amplitude of 2×10^{-4}	82
5.29 Variation of Growth Rate of \tilde{m} for Fundamental Mode with R for Different Initial \tilde{u} Amplitude.	83
5.30 Variation of Mean Skin Friction Coefficient with R for Different Initial Amplitudes.	84
5.31 Interaction Between 2D Second Mode and a 3D First Mode of Half Frequency; Growth Rates of Massflow Fluctuations Measured at the Maximum Massflow Fluctuation for the Fundamental (2,0) Mode.	85
5.32 Interaction Between 2D Second Mode and a 3D First Mode of Half Frequency; Amplitudes of Massflow Fluctuations Measured at the Maximum Massflow Fluctuation for the Fundamental (2,0) Mode.	86
5.33 Interaction Between 2D Second Mode and a 3D First Mode Including More Harmonics; Amplitudes of Massflow Fluctuations Measured at the Maximum Massflow Fluctuation for the Fundamental (2,0) Mode.	87
5.34 Nonlinear Interaction Between Two Oblique Second-Mode Waves: Amplitudes of Massflow Fluctuations Measured at the Maximum Massflow Fluctuation for the Fundamental (2,0) Mode.	88
5.35 Nonlinear Interaction Between Two Oblique Second-Mode Waves: Mean Skin Friction Coefficient at the Wall.	88

Preface

The parabolized stability equations (PSE) are a new and more reliable approach to analyzing the stability of streamwise varying flows such as boundary layers. This approach has been previously validated for idealized incompressible flows. Here, the PSE are formulated for highly compressible flows in general curvilinear coordinates to permit the analysis of high-speed boundary-layer flows over fairly general bodies. Vigorous numerical studies are carried out to study convergence and accuracy of the linear-stability code LSH, and the linear/nonlinear PSE code, PSH. Physical interfaces are set up to analyze the $M_\infty = 8$ boundary layer over a blunt cone calculated by using a thin-layer Navier Stokes (TLNS) code, and the flow over a sharp cone at angle of attack calculated using the AFWAL Parabolized Navier-Stokes (PNS) code. While stability and transition studies at high speeds are far from routine, the method developed here is the best tool available to research the physical processes in high-speed boundary layers.

Chapter 1

Introduction

Understanding and predicting the laminar-turbulent transition in flows over aerodynamic bodies is of great importance to many state-of-the-art technologies currently being pursued. Because skin friction and heat transfer in the two states of motion are very different, it is crucial to provide the practicing engineer or the researcher with the best tools to analyze transitional flow. These tools enable one to model and control the flow and, hence, optimally design modern aerospace vehicles.

The breakdown of the laminar to turbulent flow is a complex process. This process involves disturbances in the environment, receptivity mechanisms that internalize these disturbances into spatially varying basic flow, and streamwise evolution. Barring bypass transition, the initial evolution is strongly dependent on streamwise linear stability characteristics. The final breakdown is the result of nonlinear growth, secondary instability, and nonlinear interactions which create increasingly smaller scales of motion. If the freestream disturbance environment is known, the remaining transition process may be predicted.

Current tools for prediction may be roughly classified into the following groups:

1. Lump-parameter methods, based on the local boundary layer characteristics and empirical correlations.
2. The e^N criterion (Smith and Gamberoni 1956, Van Ingen 1956) based on the amplitude ratio obtained from the linear stability theory and experimentally correlated N factors.
3. Amplitude methods (Liepmann 1943, Mack 1975a, b) based not only on linear stability, but also on the level and spectral contribution of freestream disturbance (empirically).
4. Methods based on averaged transport equations, with an empirical/theoretical model for the transition region.
5. Direct Navier-Stokes (DNS) simulations and large-eddy simulations (LES) based on the expensive numerical solutions.

The first four groups neglect important streamwise variations and nonlinear mechanisms of transition process. They require sensitive correlations and extensive effort

to tune parameters for efficient and accurate use in complex design problems. The last group of numerical simulations require excessive computer memory and processing time to be feasible for engineering applications. The limitations for these methods are even more severe for high supersonic and hypersonic flows, where experimental data are scarce and the transition mechanisms are more complex. Hence, alternative methods should be developed for accurate and efficient engineering prediction of the transition process.

Alternative prediction methods based on the first principles while taking all physics into account would also require characterization of the freestream environment, surface requirement such as roughness, and qualitative and quantitative links between these disturbances and the initial conditions for the most dangerous modes of instability mechanisms. These data are largely unavailable, and receptivity mechanisms for supersonic flows are largely unknown. However, the existing base of transition data can be used to characterize the initial data at a given environment (altitude). A proper integration method of initial data shall connect this initial data to the transition process.

Therefore, in response to PRDA No. 90-07-PMRN, we proposed the development of a transition prediction method for high speed flows based on the solution of the Parabolized Stability Equations (PSE). The PSE can be solved efficiently using marching methods, while taking streamwise variations of the basic flow into account. The PSE are, therefore, much more efficient than DNS methods. It also accounts for the streamwise variations of the stability characteristics, using a streamwise adapting wavenumber for fast variations. The shape of the function accounts for the slow variations, and only the second streamwise derivatives are dropped. Moreover, it accounts for secondary instability and nonlinear growth and interactions, enabling it to predict the beginning of the breakdown process.

The concept was validated for incompressible flows (Bertolotti 1991) at the time of the proposal. The main objectives set in the proposal have been achieved and are outlined as follow:

1. Developing a new set of compressible equations accounting for variable thermal properties of air and body curvature by formulating the PSE in general curvilinear coordinates.
2. Capability to generate amplitude and growth rate curves with ease for comparison with traditional e^N methods.
3. Developing a numerical approach for good resolution of critical layers and wall viscous layers by replacing the spectral method by a 7th order Hermitian finite difference method. Better distribution of grid points is achieved, and the speed of calculations is improved by factors.
4. Setting the code in a modular form to permit use with different types of basic flows. This feature is incorporated by modular coding involving generic modules which apply to any stability problems and physics modules which interfaces between different flows/stability problems to the general modules. In particular, physics interfaces are already in place for flat plate flow, rotating disk flow, flow

over blunt cones and sharp cones. The user may add or modify these modules as new problems are encountered.

5. Addition of all nonlinear terms to the PSE and algorithms for introduction, dropping and interaction of different modes. Implementation of this module enables the code to predict secondary instabilities, nonlinear interactions, and beginning of breakdown.
6. Ability to predict transition for three dimensional (3D) disturbances in two dimensional (2D), Axisymmetric or quasi-3D basic flows. For example linear and nonlinear evolution of disturbances on swept wings (Stuckert et al. 1993) and disturbance evolution along a suitable path on a cone at angle of attack (Section 4) can be calculated.

Two codes are developed for this contract: a code for local linear stability analysis named LSH and a code for analysis using the PSE. These two codes are closely integrated, and use mostly the same general modules and physics modules. Solutions from LSH can be applied directly as initial conditions for PSH runs. In essence, we have developed a pair of highly flexible codes for stability and transition analysis that can be adapted to a variety of problems by the user. The code can be used with ease for problems with existing interfaces (provided with the codes by DynaFlow). For new problems, one must supply interface modules for metric terms of stability coordinate, basic state solution and boundary conditions. Sometimes the user may use the existing metric file, but only a new basic state file. The tradeoff for this flexibility is that the code requires the user to have knowledge of stability and transition to set up a new problem. This tradeoff should not be considered a disadvantage because this knowledge is helpful even for simple routine stability analyses.

A detailed description of the PSE formulation is given in the next chapter followed by the description and results of stability analyses using LSH and PSH for basic flows for which interfaces are already set up. Linear stability analysis of compressible flow over a flat plate are presented in Chapter 3. Results and discussions on linear stability and PSE analyses of hypersonic flow over a sharp cone at angle of attack are given in Chapter 4. In Chapter 5, linear stability, linear PSE and nonlinear PSE analyses of hypersonic flow over a blunt cone at zero angle of attack are described. Some general comments on the codes and results are given in the last chapter.

Chapter 2

PSE Methodology

The PSE predict the evolution of a rapidly changing, small scale disturbance superposed upon a steady, slowly varying laminar flow. The undisturbed laminar flow, referred to as the basic state, is presumed to be known, having been computed as an exact or approximate solution of the *steady-state* Navier-Stokes equations. The total flow:

$$\mathbf{Q} = \mathbf{Q}_0 + \tilde{\mathbf{Q}} \quad (2.1)$$

- the superposition of the basic state and the disturbance - is, on the other hand, to be determined by the solution of the *unsteady* Navier-Stokes equations. The unsteady Navier-Stokes equations really govern the evolution of the *disturbance* because the basic state is presumed known. Hence, when formulated directly in terms of the disturbances using equation (2.1), they are known as the disturbance equations.

The disturbance equations are nonlinear because the Navier-Stokes equations are nonlinear. Although the PSE can account for this nonlinearity, it is easier to first consider the situation when the disturbance has a vanishingly small amplitude. In this case, the equations are linear and the disturbance coefficients are independent of time because the basic state is steady. Assuming that the disturbance *boundary* conditions are also separable in time, a Fourier transform can be applied to the disturbance and its equations. More generally, a discrete or continuous Fourier transform may be applied in each dimension in which the basic flow and geometry do not vary. This decomposes the disturbance into a multidimensional spectrum of waves:

$$\tilde{\mathbf{Q}} = \sum_{m=0}^{nm} \left(\tilde{\mathbf{Q}}_m + \bar{\tilde{\mathbf{Q}}}_m \right) \quad (2.2)$$

each wave being governed by the linear disturbance equations transformed from the time and space domain to the frequency and wavenumber domain.

One dimension in which a Fourier transformation is not strictly valid is the distance, say s , in the streamwise direction. However, since the basic flow varies slowly with s , the functional dependence of each wave on s can be decomposed into a number of amplitude and wavenumber-modulated sinusoids, the modulations varying slowly in space. The governing equations for the modulated waves are then obtained by performing yet another transformation of the linear disturbance equations to this hybrid s -space, s -wavenumber domain.

This decomposition is one of the key elements in the development of the PSE. It provides one with a meaningful way to neglect the second derivatives with respect to s of the modulated amplitude and obtain a system of parabolized equations which can be solved very efficiently using a space marching technique. Note that usually *all* of the derivatives of the modulations with respect to s are neglected, yielding a system of ordinary equations and an eigenvalue problem to solve in the transformed domain. However, for crossflow vortices and other longitudinal vortices, this latter approximation can be inaccurate.

The derivation of the PSE is discussed in greater detail below. First, the pertinent variables are nondimensionalized. The Navier-Stokes equations are then presented in an inertial Cartesian coordinate system and linearized around the laminar basic state to yield the linear disturbance equations. A coordinate transformation is then made to identify meaningful independent variables for the Fourier transformations and subsequent approximations. The coordinate transformation also enables the boundary conditions to be enforced easily and accurately. Finally, some of the details of the nonlinear analyses are also presented.

2.1 Nondimensionalizations

$$x^k = x^{*k}/L^* \quad (2.3)$$

$$t = t^*/(L^*/U_\infty^*) \quad (2.4)$$

$$u^j = u^{*j}/U_\infty^* \quad (2.5)$$

$$p = p^*/(\rho_\infty^* U_\infty^{*2}) \quad (2.6)$$

$$T = T^*/T_\infty^* \quad (2.7)$$

$$\rho = \rho^*/\rho_\infty^* \quad (2.8)$$

$$h = h^*/R^*T_\infty^* \quad (2.9)$$

$$\mu = \mu^*/\mu_\infty^* \quad (2.10)$$

$$\lambda = \lambda^*/\mu_\infty^* \quad (2.11)$$

$$\kappa = \kappa^*/(\mu_\infty^* R^*) \quad (2.12)$$

$$S^{jk} = S^{*jk}/(\mu_\infty^* U_\infty^*/L^*) \quad (2.13)$$

$$q^k = q^{*k}/(\mu_\infty^* R^*T_\infty^*/L^*) \quad (2.14)$$

Note that the Prandtl number $Pr = \mu^* c_p^* / \kappa^* = \mu c_p / \kappa$.

For the cone calculations considered in this report, the reference temperature is the free-stream static temperature; the reference viscosity is the free-stream viscosity; the reference density is the free-stream density; the reference velocity is the free-stream velocity; and the reference length is the length of the model divided by the square root of the Reynolds number based upon the reference density, velocity, viscosity, and model length.

With these nondimensionalizations, the Navier-Stokes equations in an inertial Cartesian coordinate system can be written as follows.

2.2 Navier-Stokes Equations

$$\frac{\partial \rho}{\partial t} + \frac{\partial \rho u^k}{\partial x^k} = 0 \quad (2.15)$$

$$\rho \frac{\partial u^j}{\partial t} + \rho u^k \frac{\partial u^j}{\partial x^k} + \frac{\partial p}{\partial x^j} = \frac{1}{Re} \frac{\partial S^{jk}}{\partial x^k} \quad (2.16)$$

$$\begin{aligned} \rho \frac{\partial h}{\partial t} + \rho u^k \frac{\partial h}{\partial x^k} - \frac{U_\infty^{*2}}{R^* T_\infty^*} \left(\frac{\partial p}{\partial t} + u^k \frac{\partial p}{\partial x^k} \right) \\ = \frac{-1}{Re} \frac{\partial q^k}{\partial x^k} + \frac{1}{Re} \frac{U_\infty^{*2}}{R^* T_\infty^*} \Phi_v \end{aligned} \quad (2.17)$$

(For an ideal gas, the speed of sound $a^* = \sqrt{\gamma R^* T^*}$, and $U_\infty^{*2}/R^* T_\infty^* = \gamma M_\infty^2$.) Here, the index $k \in (1, 2, 3)$ and $\mathbf{x} = (x^1, x^2, x^3)$ is the position vector in the inertial Cartesian coordinate system. The viscous stress tensor S^{jk} is

$$S^{jk} = \mu \left(\frac{\partial u^k}{\partial x^j} + \frac{\partial u^j}{\partial x^k} \right) + \lambda \delta^{jk} \frac{\partial u^m}{\partial x^m} \quad (2.18)$$

The components q^k of the heat flux are

$$q^k = -\kappa \frac{\partial T}{\partial x^k} \quad (2.19)$$

Finally, the viscous dissipation is

$$\Phi_v = S^{jk} \frac{\partial u^j}{\partial x^k} \quad (2.20)$$

2.3 Disturbance Equations

The disturbance equations are obtained by substituting the disturbed flow field (2.1) into the Navier-Stokes equations. Nonlinear terms are then expanded in a truncated Taylor series about the basic state so that each is in the form of a sum of products of the disturbance variables.

A typical term in the momentum equations is of the form:

$$\rho \frac{\partial u^j}{\partial t} = (\rho + \tilde{\rho}) \left(\frac{\partial u^j}{\partial t} + \frac{\partial \tilde{u}^j}{\partial t} \right) \quad (2.21)$$

$$= \rho \frac{\partial u^j}{\partial t} + \tilde{\rho} \frac{\partial u^j}{\partial t} + \rho \frac{\partial \tilde{u}^j}{\partial t} + \tilde{\rho} \frac{\partial \tilde{u}^j}{\partial t} \quad (2.22)$$

$$\begin{aligned} &= \rho \frac{\partial u^j}{\partial t} + \sum_{m=0}^{nm} (\tilde{\rho}_m + \bar{\tilde{\rho}}_m) \frac{\partial u^j}{\partial t} \\ &\quad + \rho \sum_{m=0}^{nm} \left(\frac{\partial \tilde{u}_m^j}{\partial t} + \frac{\partial \bar{\tilde{u}}_m^j}{\partial t} \right) \end{aligned} \quad (2.23)$$

$$+ \sum_{m=0}^{nm} (\tilde{\rho}_m + \bar{\tilde{\rho}}_m) \sum_{l=0}^{nm} \left(\frac{\partial \tilde{u}_l^j}{\partial t} + \frac{\partial \bar{\tilde{u}}_l^j}{\partial t} \right)$$

The nonlinear disturbance equations are obtained by similarly expanding *all* of the terms in the Navier-Stokes equations. The equations will then contain three different types of products. Some products will involve basic state quantities only (i.e., the first of the terms in equation (2.22)), some will be linear in the disturbances (i.e., the second and third terms in equation (2.22)), and the rest will be nonlinear in the disturbances (i.e., the last term in equation (2.22)). These terms in the equations can then be grouped accordingly.

In each governing equation the group of basic state terms will sum to zero because the basic state is assumed to be an exact solution of the Navier-Stokes equations. The linear terms can then be placed on the right hand sides of the equations, and the nonlinear terms on the left hand sides of the equations. The nonlinear terms are then expanded in Fourier series using the elementary modes \tilde{Q}_m as the basis functions. Orthogonality conditions between the basis functions (or the principle of harmonic balancing - see Herbert (1991) and Bertolotti (1991) for more details) are then enforced to obtain the equations governing the evolution of each mode.

In the nonlinear case, the equations for different modes may be coupled to each other. However, the linear terms in the equations are the same regardless of the mode amplitudes. Hence, the linear terms are presented below in the form of the linear disturbance equations.

Denote the linearized material derivative acting on any quantity Q^j by:

$$\frac{\widetilde{D}Q^j}{Dt} = \frac{\partial \tilde{Q}^j}{\partial t} + u^k \frac{\partial \tilde{Q}^j}{\partial x^k} + \tilde{u}^k \frac{\partial Q^j}{\partial x^k} \quad (2.24)$$

where $\tilde{Q} = (\tilde{Q}^1, \tilde{Q}^2, \tilde{Q}^3, \tilde{Q}^4, \tilde{Q}^5) = (\tilde{\rho}, \tilde{T}, \tilde{u}^1, \tilde{u}^2, \tilde{u}^3)$.

The linear disturbance equations in inertial Cartesian coordinates are:

$$\frac{\widetilde{D}\rho}{Dt} + \tilde{\rho} \frac{\partial u^k}{\partial x^k} + \rho \frac{\partial \tilde{u}^k}{\partial x^k} = 0 \quad (2.25)$$

$$\begin{aligned} & \rho \sum_{s=1}^{nts} \left(\sum_{r=1}^{nts} \frac{\partial^2 h}{\partial Q^s \partial Q^r} \frac{DQ^r}{Dt} \right) \tilde{Q}^s + \rho \left(\sum_{r=1}^{nts} \frac{\partial h}{\partial Q^r} \frac{\widetilde{D}Q^r}{Dt} \right) \\ & + \tilde{\rho} \sum_{r=1}^{nts} \frac{\partial h}{\partial Q^r} \frac{DQ^r}{Dt} - \frac{U_\infty^{*2}}{R^* T_\infty^*} \sum_{r=1}^{nts} \frac{\partial p}{\partial Q^r} \frac{\widetilde{D}Q^r}{Dt} \\ & - \frac{U_\infty^{*2}}{R^* T_\infty^*} \sum_{s=1}^{nts} \left(\sum_{r=1}^{nts} \frac{\partial^2 p}{\partial Q^s \partial Q^r} \frac{DQ^r}{Dt} \right) \tilde{Q}^s \\ & + \frac{1}{Re} \frac{\partial \tilde{q}^k}{\partial x^k} - \frac{1}{Re} \left(\frac{U_\infty^{*2}}{R^* T_\infty^*} \right) \tilde{\Phi}_v = 0 \end{aligned} \quad (2.26)$$

$$\begin{aligned} & \tilde{\rho} \frac{Du^j}{Dt} + \rho \frac{\widetilde{D}u^j}{Dt} + \sum_{s=1}^{nts} \left(\sum_{r=1}^{nts} \frac{\partial^2 p}{\partial Q^s \partial Q^r} \frac{\partial Q^r}{\partial x^j} \right) \tilde{Q}^s \\ & + \sum_{r=1}^{nts} \frac{\partial p}{\partial Q^r} \frac{\partial \tilde{Q}^r}{\partial x^j} - \frac{1}{Re} \frac{\partial \tilde{S}^{jk}}{\partial x^k} = 0 \end{aligned} \quad (2.27)$$

The linear disturbance in the divergence of the heat flux is:

$$\begin{aligned}
 -\frac{\partial \tilde{q}^k}{\partial x^k} &= \sum_{s=1}^{nts} \left(\sum_{r=1}^{nts} \frac{\partial^2 \kappa}{\partial Q^s \partial Q^r} \frac{\partial Q^r}{\partial x^k} \frac{\partial T}{\partial x^k} \right) \tilde{Q}^s \\
 &+ \sum_{r=1}^{nts} \frac{\partial \kappa}{\partial Q^r} \frac{\partial \tilde{Q}^r}{\partial x^k} \frac{\partial T}{\partial x^k} + \sum_{r=1}^{nts} \frac{\partial \kappa}{\partial Q^r} \frac{\partial Q^r}{\partial x^k} \frac{\partial \tilde{T}}{\partial x^k} \\
 &+ \left(\sum_{r=1}^{nts} \frac{\partial \kappa}{\partial Q^r} \tilde{Q}^r \right) \frac{\partial^2 T}{\partial x^k \partial x^k} + \kappa \frac{\partial^2 \tilde{T}}{\partial x^k \partial x^k}
 \end{aligned} \tag{2.28}$$

The linear disturbance in the divergence of the shear stress tensor is:

$$\begin{aligned}
 \frac{\partial \tilde{S}^{jk}}{\partial x^k} &= \sum_{s=1}^{nts} \left\{ \sum_{r=1}^{nts} \frac{\partial^2 \mu}{\partial Q^s \partial Q^r} \frac{\partial Q^r}{\partial x^k} \left(\frac{\partial u^j}{\partial x^k} + \frac{\partial u^k}{\partial x^j} \right) \right\} \tilde{Q}^s \\
 &+ \sum_{s=1}^{nts} \left\{ \sum_{r=1}^{nts} \frac{\partial^2 \lambda}{\partial Q^s \partial Q^r} \frac{\partial Q^r}{\partial x^k} \left(\frac{\partial u^j}{\partial x^j} \right) \right\} \tilde{Q}^s \\
 &+ \sum_{r=1}^{nts} \frac{\partial \mu}{\partial Q^r} \frac{\partial \tilde{Q}^r}{\partial x^k} \left(\frac{\partial u^j}{\partial x^k} + \frac{\partial u^k}{\partial x^j} \right) \\
 &+ \sum_{r=1}^{nts} \frac{\partial \lambda}{\partial Q^r} \frac{\partial \tilde{Q}^r}{\partial x^k} \left(\frac{\partial u^j}{\partial x^j} \right) \\
 &+ \sum_{r=1}^{nts} \frac{\partial \mu}{\partial Q^r} \frac{\partial Q^r}{\partial x^k} \left(\frac{\partial \tilde{u}^j}{\partial x^k} + \frac{\partial \tilde{u}^k}{\partial x^j} \right) \\
 &+ \sum_{r=1}^{nts} \frac{\partial \lambda}{\partial Q^r} \frac{\partial Q^r}{\partial x^k} \left(\frac{\partial \tilde{u}^j}{\partial x^j} \right) \\
 &+ \sum_{r=1}^{nts} \frac{\partial \mu}{\partial Q^r} \frac{\partial^2 u^k}{\partial x^j \partial x^j} \tilde{Q}^r + \mu \frac{\partial^2 \tilde{u}^k}{\partial x^j \partial x^j} \\
 &+ \sum_{r=1}^{nts} \left(\frac{\partial \mu}{\partial Q^r} + \frac{\partial \lambda}{\partial Q^r} \right) \frac{\partial^2 u^j}{\partial x^k \partial x^j} \tilde{Q}^r \\
 &+ (\mu + \lambda) \frac{\partial^2 \tilde{u}^k}{\partial x^j \partial x^j}
 \end{aligned} \tag{2.29}$$

Next, the coordinate system is transformed to enable the accurate implementation of the PSE approximation and boundary conditions.

2.4 Transformation of the Independent and Dependent Variables

Let the coordinate transformation be given by:

$$x^k = x^k(\xi, t) \tag{2.30}$$

$$t = \tau \tag{2.31}$$

where the body surface is $\xi^2 = 0$. The index $k \in (1, 2, 3)$ and $\mathbf{x} = (x^1, x^2, x^3)$ is the position vector in the inertial Cartesian coordinate system.

The derivatives of the disturbance variables with respect to ξ^k can easily be computed using the chain rule for partial differentiation. Before this is actually done, however, the dependent variables are also transformed. This is because the approximations used to solve for the disturbances are not valid for every possible choice of dependent variables that one may choose to work with. In the actual software that we have developed, a number of reasonable options have been implemented. One that is commonly chosen uses the density and temperature:

$$\tilde{Q}_m^k = f_m^k(\xi, \tau) \exp \{i\theta_m(\xi^1, \xi^3, \tau)\} \quad (k = 1, 2) \quad (2.32)$$

and the physical values of the contravariant velocity components in the curvilinear coordinate system (i.e., Borisenko and Tarapov [1979], pp. 23-35):

$$\begin{aligned} \tilde{Q}_m^k &= \frac{1}{\sqrt{g_{jj}}} \frac{\partial x^{k-2}}{\partial \xi^j} f_m^{j+2}(\xi, \tau) \exp \{i\theta_m(\xi^1, \xi^3, \tau)\} \\ &\quad (k = 3, 4, 5) \end{aligned} \quad (2.33)$$

Here, f_m^j is the j th component of the *shape function* \mathbf{f} for the m^{th} elementary mode. The repeated index j in the previous equation indicates a summation from 1 to 3. g_{jj} (no summation) is the diagonal element in row j of the covariant metric tensor g_{ij} :

$$g_{ij} = \frac{\partial x^k}{\partial \xi^i} \frac{\partial x^k}{\partial \xi^j} \quad (2.34)$$

where the repeated index k also indicates a summation from 1 to 3. θ_m is the (complex) phase for the m^{th} mode and is assumed to be a function of $\xi^1(\mathbf{x}, t)$, $\xi^3(\mathbf{x}, t)$, and τ , but not of $\xi^2(\mathbf{x}, t)$. Its gradient is:

$$\alpha_m = \frac{\partial \theta}{\partial \xi^1} \quad (2.35)$$

$$\beta_m = \frac{\partial \theta}{\partial \xi^3} \quad (2.36)$$

$$\omega_m = -\frac{\partial \theta}{\partial \tau} \quad (2.37)$$

This assumed form for the disturbance modes is fundamental to the Parabolized Stability Equations and has arisen as an extension of the local linear stability analyses. The local linear stability analyses are more restrictive because they formally require that the disturbance equations be separable in τ , ξ^1 , and ξ^3 . Since the PSE account for the variations in the shape functions of the different modes, they are not bound by this restriction. Moreover, they can also account for inhomogeneous boundary conditions and nonlinearity.

2.5 Nonlinear Terms and Modal Decomposition

The means by which the nonlinear terms in the disturbance equations are incorporated can now be explained more fully. Assume for simplicity that Cartesian coordinates

are used. Substituting equations (2.32) and (2.33) into equation (2.23), one obtains sums of products of the form:

$$\begin{aligned} & \sum_{m=0}^{nm} \left(\tilde{\rho}_m + \bar{\tilde{\rho}}_m \right) \sum_{l=0}^{nm} \left(\frac{\partial \tilde{u}_l^j}{\partial t} + \frac{\partial \bar{\tilde{u}}_l^j}{\partial t} \right) \\ &= \sum_{m=0}^{nm} \sum_{l=0}^{nm} \left(\tilde{\rho}_m \frac{\partial \tilde{u}_l^j}{\partial t} + \tilde{\rho}_m \frac{\partial \bar{\tilde{u}}_l^j}{\partial t} + \bar{\tilde{\rho}}_m \frac{\partial \tilde{u}_l^j}{\partial t} + \bar{\tilde{\rho}}_m \frac{\partial \bar{\tilde{u}}_l^j}{\partial t} \right) \end{aligned} \quad (2.38)$$

If the underlying laminar flow is stationary and invariant in the circumferential direction, then ω_m and β_m are constants for each m . Moreover, if one chooses an equally spaced "grid" in the frequency and circumferential wavenumber domains, then the frequency and circumferential wavenumber for each mode are integral multiples of some corresponding fundamentals $\Delta\omega$ and $\Delta\beta$, respectively:

$$\omega_m = j(m)\Delta\omega \quad (2.39)$$

$$\beta_m = k(m)\Delta\beta \quad (2.40)$$

The product of two typical modes m_1 and m_2 in equation (2.38) above then yields terms *proportional* to

$$f_{m_1}^1 f_{m_2}^2 \exp [i \{j(m_1) + j(m_2)\} (\Delta\omega)\tau + i \{k(m_1) + k(m_2)\} (\Delta\beta)\xi^3] \quad (2.41)$$

Due to the orthogonality of the sinusoidal functions, this creates a nonlinear forcing term for the mode m_3 which simultaneously satisfies

$$j(m_3) = j(m_1) + j(m_2) \quad (2.42)$$

$$k(m_3) = k(m_1) + k(m_2) \quad (2.43)$$

Products of one complex mode with the *conjugate* of another mode generate *differences* in the phase functions instead of sums, etc. Also, higher order (i.e., cubic) nonlinearities are treated in the same way, yielding the nonlinear equations governing the evolution of each mode.

The final governing equations in the curvilinear coordinate system are obtained by substituting equations (2.32) and (2.33) into the disturbance equations and transforming the derivatives using the chain rule for partial differentiation. The nonlinear terms are computed as described above, and then the PSE approximation is made.

2.6 PSE Approximation

In linear stability theory the variations of the shape function f_m and α_m , β_m , and ω_m with ξ^1 and ξ^3 are usually neglected in order to reduce the governing system of partial differential equations to a system of ordinary differential equations. The boundary conditions are also usually assumed to be homogeneous. Two of the three parameters α_m , β_m and ω_m must then be specified and a complex eigenvalue problem solved for the third.

The PSE methodology still requires the specification of constant ω_m and β_m . However, the variations of the shape function with respect to ξ^1 are not neglected. Hence, the partition of the variations of the disturbance with respect to ξ^1 between the shape function and the exponential factor $\exp\{i\theta_m(\xi^1, \xi^3, \tau)\}$ must be specified. A method for doing this is described by Herbert (1991). It is motivated by a desire to make $\partial^2 f_m / \partial \xi^1 \partial \xi^1$ "small" relative to other terms in the governing equations so that it may be neglected.

Consider any component l of the m^{th} mode. Its logarithmic derivative is:

$$\begin{aligned} & \frac{\partial}{\partial \xi^1} \left\{ \ln[f_m^l(\xi) \exp\{i\theta_m(\xi^1, \xi^3, \tau)\}] \right\} \\ &= i\alpha_m + \frac{\partial}{\partial \xi^1} \left\{ \ln(f_m^l(\xi)) \right\} \end{aligned} \quad (2.44)$$

Since f_m^l depends upon both ξ^1 and ξ^2 , this equation in general implies a dependence of α upon both l and ξ^2 . If one specifies a particular value of l , the dependence of α upon ξ^2 may be eliminated by multiplying equation (2.44) by a weight factor $|f_m^l|^2 \equiv f_m^l \bar{f}_m^l$ and integrating over the entire domain $[0, \xi_{\max}^2]$ of ξ^2 :

$$\begin{aligned} & \frac{\int_0^{\xi_{\max}^2} |f_m^l|^2 \frac{\partial}{\partial \xi^1} \left\{ \ln[f_m^l(\xi) \exp(i\theta_m)] \right\} d\xi^2}{\int_0^{\xi_{\max}^2} |f_m^l|^2 d\xi^2} \\ &= i\alpha + \frac{\int_0^{\xi_{\max}^2} \bar{f}_m^l \frac{\partial f_m^l}{\partial \xi^1} d\xi^2}{\int_0^{\xi_{\max}^2} |f_m^l|^2 d\xi^2} \end{aligned} \quad (2.45)$$

The partition is now specified by setting

$$\int_0^{\xi_{\max}^2} \bar{f}_m^l \frac{\partial f_m^l}{\partial \xi^1} d\xi^2 \equiv 0 \quad (2.46)$$

Equation (2.45) then becomes:

$$\frac{\int_0^{\xi_{\max}^2} |f_m^l|^2 \frac{\partial}{\partial \xi^1} \left\{ \ln[f_m^l(\xi) \exp(i\theta_m)] \right\} d\xi^2}{\int_0^{\xi_{\max}^2} |f_m^l|^2 d\xi^2} = i\alpha_m \quad (2.47)$$

and is used to specify $\alpha(\xi^1)$.

Note that the partition depends upon l and the grid used for the calculations. However, different choices of l and different grids should lead to the same *physical* solution $\tilde{\mathbf{Q}}$ to within the order of error incurred by the PSE approximation.¹ This approximation is that the derivative $\partial^2 f_m / \partial \xi^1 \partial \xi^1$ is negligibly small in comparison with the remaining terms in the disturbance equations and, hence, can be dropped.² The linear PSE, thus, can be obtained from the disturbance equations by neglecting the (viscous) terms involving $\partial^2 f_m / \partial \xi^1 \partial \xi^1$.

For any particular disturbance calculation the equation of state, transport properties, boundary conditions and initial conditions, grid $\xi^k = \xi^k(\mathbf{x}, t)$, and basic state must be specified. These are described next.

¹We have used $l = 3$.

²Note that the shape function is independent of ξ^3 for an axisymmetric body at zero angle of attack because both the geometry and flow field are.

2.7 Constitutive Equations

The gas is assumed to be air and is modeled as perfect in this analysis. Hence, the equation of state is:

$$p(\rho, T) = \frac{\rho T}{\gamma M_\infty^2} \quad (2.48)$$

The enthalpy h is:

$$h(T) = \frac{\gamma T}{\gamma - 1} \quad (2.49)$$

$$c_p = \frac{\gamma}{\gamma - 1} \quad (2.50)$$

where $\gamma = 1.4$. Sutherland's law is used for the dynamic viscosity:

$$\mu(T) = (1 + 110.4K/T_\infty^*) \left(\frac{T^{3/2}}{T + 110.4K/T_\infty^*} \right) \quad (2.51)$$

The second coefficient of viscosity is obtained from Stokes' hypothesis:

$$\lambda = -\frac{2}{3}\mu \quad (2.52)$$

Finally, the thermal conductivity is computed assuming that the Prandtl number is a constant equal to 0.72:

$$k = \frac{\mu c_p}{0.72} \quad (2.53)$$

Other constitutive equations for the thermophysical properties of air can also be selected. See the Appendix: Constitutive Equations.

2.8 Boundary Conditions and Initial Conditions

The following general conditions are applied in `boundary.ins` files provided with the built-in sample applications. At the wall, disturbance temperature \tilde{Q}^2 and velocities are set to zero. At farfield, ξ_{max}^2 , disturbance temperature \tilde{Q}^2 , velocities in ξ^1 and ξ^3 directions are set to zero. Then ξ^2 -gradient of disturbance velocity in ξ^2 direction is determined from the continuity equation assuming that density \tilde{Q}^1 and gradients of density are zero implicitly.¹ No explicit boundary condition on density is required at either end of the boundaries. For the current version of the code, asymptotic conditions are implemented only for blunt-cone calculations using orthogonal body-intrinsic coordinates. Boundary conditions for the *stationary* ($\omega = 0$) modes may be different from those of oscillatory disturbances. For example, when the basic

¹The user may choose to set this velocity component to zero for oscillatory modes with little or no change in the solution.

laminar flow satisfies the adiabatic wall boundary condition, normal gradient of \tilde{T} for stationary modes may be set to zero (see Mack 1984).

The disturbance velocity and temperature gradient are assumed to vanish at the surface. Initial conditions are obtained by making the locally quasi-parallel flow approximation: the shape function is assumed to depend only upon ξ^2 ; the covariant components α_m and β_m of the wavenumber vector are all assumed to be constant; and all of the coefficients in the disturbance equations which depend on ξ^1 and ξ^3 are evaluated at the location of the initial data.

2.9 Numerical Method

The PSE approximation enables a solution for the disturbance to be obtained efficiently by integrating the equations in the ξ^1 direction with a space marching algorithm. Here, the implicit backward Euler method is used for discretization of derivatives with respect to ξ^1 . The nonlinear terms, however, have been treated explicitly as this saves a significant amount of computational time. Also, our earlier calculations had used a spectral collocation method for discretization of derivatives with respect to ξ^2 . We have since begun to use a seventh order accurate compact finite difference scheme on the interior which leads to a system of block tridiagonal equations. This system of block tridiagonal equations can be solved much more efficiently than the full matrices obtained with the spectral method while the seventh order accuracy maintains the quality of the solution. In summary, the solution algorithm is now much more efficient.

Nevertheless, since even the equations for a single mode are nonlinear in α_m due to its appearance in the differential operators acting upon the shape function, α_m must first be guessed at each new streamwise station, updated by imposing the norm on f , and then iterated upon until convergence. These iterations typically converge rapidly, but the rate of convergence depends upon the step size and flow and, in the case of nonlinear analyses, on the amplitudes of the disturbances.

Chapter 3

Compressible Boundary Layer over the Flat Plate

The stability of the compressible boundary layer on a flat plate is investigated as a test case for the insert files which incorporate general curvilinear coordinates. Two different coordinate systems are used. The first of these is a stretched rectilinear grid whose point distribution matches that of the wall normal similarity variable along the inflow boundary. The second coordinate system is curvilinear and nonorthogonal. It uses the wall normal similarity variable and the distance measured from the leading edge of the plate as its two coordinates.

While we now use the Hermitian finite difference method to discretize and solve the disturbance equations, the results presented in this section were obtained with the slower but extremely accurate spectral collocation technique. The high accuracy of the spectral method enables very careful comparisons to be made which can reveal errors in the formulation or software.

In addition, the *linear* disturbance equations are formulated in terms of $(\tilde{p}, \tilde{T}, \tilde{u}, \tilde{v}, \tilde{w})$, where \tilde{p} is the disturbance pressure, \tilde{T} the disturbance temperature, and $(\tilde{u}, \tilde{v}, \tilde{w})$ the disturbance velocity vector in Cartesian coordinates. This selection of dependent variables is useful because it makes it easier to study incompressible flows simply by changing the equation of state from the ideal gas law to $\rho \equiv 1$.¹ However, the subsequent nonlinear work uses as dependent variables: $(\tilde{p}, \tilde{T}, \tilde{u}, \tilde{v}, \tilde{w})$, the same set as appears in the formulation of the disturbance equations in Chapter 2. This latter choice makes it easier to formulate the nonlinear terms because it gives rise to *products* of sums of the basic state and disturbance modes rather than quotients. The drawback is that it seems to require many more Chebyshev polynomials than does the pressure formulation for the same level of accuracy. We observed this when we confirmed the changes in the linear equations by comparing the results from the density formulation to those from the pressure formulation.

¹Incompressible flows were studied and tested prior to performing the compressible flow tests outlined here.

3.1 Basic State Similarity Solution

The basic state compressible boundary layer is specified to be the Blasius similarity solution. This section presents some of the details of the similarity transformation and resulting equations.

3.1.1 Governing Equations and Similarity Transformation

The two-dimensional compressible boundary layer equations for steady flow over a flat plate are:

$$\frac{\partial \rho u}{\partial x} + \frac{\partial \rho v}{\partial y} = 0 \quad (3.1)$$

$$\rho u \frac{\partial u}{\partial x} + \rho v \frac{\partial u}{\partial y} = \frac{1}{Re_L} \frac{\partial}{\partial y} \left(\mu \frac{\partial u}{\partial y} \right) \quad (3.2)$$

$$\frac{\partial p}{\partial y} = 0 \quad (3.3)$$

$$\rho u \frac{\partial h}{\partial x} + \rho v \frac{\partial h}{\partial y} = \frac{1}{Re_L} \frac{\partial}{\partial y} \left(k \frac{\partial T}{\partial y} \right) + \mu \frac{\gamma_e M_e^2}{Re_L} \left(\frac{\partial u}{\partial y} \right)^2 \quad (3.4)$$

(See, for instance, White [1974].)

Here x is the distance from the leading edge of the plate and y is the distance measured normal to it. u and v are the corresponding velocity components, ρ is the density of the gas, and h is its enthalpy. p is the static pressure and T is the static temperature. μ and k are the dynamic viscosity and thermal conductivity of the gas, respectively.

The gas is assumed to be ideal so that the enthalpy is a function only of the temperature. The transport properties are also assumed to be functions of the temperature only.

All length scales have been nondimensionalized by $L_0^* = \sqrt{x_0^* \mu_e^* / \rho_e^* U_e^*}$ where x_0^* is the nominal distance from the leading edge of the plate and μ_e^* , ρ_e^* , and U_e^* are the dynamic viscosity, gas density, and flow speed, respectively, at the boundary layer edge. The pressure has been nondimensionalized by $\rho_e^* U_e^{*2}$, but the temperature has been nondimensionalized by its edge value T_e^* and the enthalpy has been nondimensionalized by $R^* T_e^*$. (R^* is the gas constant.) The viscosity has been nondimensionalized by μ_e^* and the thermal conductivity by $\mu_e^* R^*$. (Note, then, that the Prandtl number $= \mu^* c_p^* / k^* = \mu c_p / k$, where $c_p = dh/dT$ is the specific heat at constant pressure nondimensionalized by the gas constant R^* .)

Finally, $Re_L = \rho_e^* U_e^* L_0^* / \mu_e^*$ is the Reynolds number, $\gamma_e = c_{pe} / (c_{pe} - 1)$ is the ratio of specific heats at the boundary layer edge, and $M_e = U_e^* / \sqrt{\gamma_e R^* T_e^*}$ is the boundary layer edge Mach number.

A similarity solution for these equations can be found (again, see White [1974]) subject to the boundary conditions:

$$u(0, y) = 1 \quad (3.5)$$

$$T(0, y) = 1 \quad (3.6)$$

$$u(x, 0) = 0 \quad (3.7)$$

$$v(x, 0) = 0 \quad (3.8)$$

$$\frac{\partial T}{\partial y}(x, 0) = 0 \quad (3.9)$$

$$\lim_{y \rightarrow \infty} u(x, y) = 1 \quad (3.10)$$

$$\lim_{y \rightarrow \infty} T(x, y) = 1 \quad (3.11)$$

This involves (a modification of) the Illingsworth transformation of the independent variables:

$$x = \xi \quad (3.12)$$

$$y = \sqrt{\frac{2x}{x_0}} \int_0^\eta T(s) ds \quad (3.13)$$

Here, $T = T(\eta)$ is assumed to be a function only of η and not of x . Also, make note of the fact that $x_0 = Re_L$ with the present choice of length scale.

The derivative matrix of x and y with respect to ξ and η is

$$\begin{pmatrix} \frac{\partial x}{\partial \xi} & \frac{\partial x}{\partial \eta} \\ \frac{\partial y}{\partial \xi} & \frac{\partial y}{\partial \eta} \end{pmatrix} = \begin{pmatrix} 1 & 0 \\ \frac{1}{2x} \sqrt{\frac{2x}{x_0}} \int_0^\eta T(s) ds & \sqrt{\frac{2x}{x_0}} T(\eta) \end{pmatrix} \quad (3.14)$$

and its inverse is:

$$\begin{pmatrix} \frac{\partial \xi}{\partial x} & \frac{\partial \xi}{\partial y} \\ \frac{\partial \eta}{\partial x} & \frac{\partial \eta}{\partial y} \end{pmatrix} = \begin{pmatrix} 1 & 0 \\ \frac{-1}{2xT} \int_0^\eta T(s) ds & \frac{1}{\sqrt{2x/x_0 T(\eta)}} \end{pmatrix} \quad (3.15)$$

Now introduce the stream function ψ :

$$\rho u = \frac{\partial \psi}{\partial y} \quad (3.16)$$

$$\rho v = -\frac{\partial \psi}{\partial x} \quad (3.17)$$

In terms of ξ and η ,

$$\rho u = \frac{1}{\sqrt{2x/x_0 T}} \frac{\partial \psi}{\partial \eta} \quad (3.18)$$

$$\rho v = -\frac{\partial \psi}{\partial \xi} + \frac{1}{2xT} \int_0^\eta T(s) ds \frac{\partial \psi}{\partial \eta} \quad (3.19)$$

Since the pressure is constant through the boundary layer and the gas is ideal, $\rho(x, y)T(x, y) \equiv 1$. Hence, equation (3.18) can be written:

$$u = \frac{1}{\sqrt{2x/x_0}} \frac{\partial \psi}{\partial \eta} \quad (3.20)$$

Assuming that u is a function $df/d\eta$ of η alone (where $df/d\eta = 0$ at $\eta = 0$ to satisfy the no slip condition),

$$\frac{df}{d\eta}(\eta) = \frac{1}{\sqrt{2\xi/x_0}} \frac{\partial \psi}{\partial \eta} \quad (3.21)$$

Integrating with respect to η gives

$$\psi = \sqrt{\frac{2\xi}{x_0}} f(\eta) + \phi(\xi) \quad (3.22)$$

Substituting this into equation (3.19) and using $\rho T \equiv 1$ gives

$$v = \frac{1}{2x} \sqrt{\frac{2x}{x_0}} \left(f'(\eta) \int_0^\eta T(s) ds - f(\eta) T(\eta) \right) - \phi'(\xi) T(\eta) \quad (3.23)$$

Since there is no wall suction, one must have $\phi'(\xi) \equiv 0$ in order to satisfy $v = 0$ at the wall. For simplicity, then, set $\phi(\xi) \equiv 0$.

To summarize, the stream function is:

$$\psi = \sqrt{\frac{2x}{x_0}} f(\eta) \quad (3.24)$$

The tangential velocity component is:

$$u = \frac{df}{d\eta}(\eta) \quad (3.25)$$

and the normal velocity component is:

$$v = \frac{1}{2x} \sqrt{\frac{2x}{x_0}} \left(f'(\eta) \int_0^\eta T(s) ds - f(\eta) T(\eta) \right) \quad (3.26)$$

Using these expressions, the material derivative operator can be written

$$\frac{D}{Dt} = u \frac{\partial}{\partial x} + v \frac{\partial}{\partial y} \quad (3.27)$$

$$= f'(\eta) \frac{\partial}{\partial \xi} - \frac{f(\eta)}{2x} \frac{\partial}{\partial \eta} \quad (3.28)$$

The boundary layer equations thus become (with $\rho = 1/T$)

$$-\frac{ff'}{2xT} = \left(\frac{1}{Re_L} \right) \left(\frac{1}{2Tx/x_0} \right) \frac{d}{d\eta} \left(\frac{\mu f''}{T} \right) \quad (3.29)$$

$$-\frac{fc_p T'}{2xT} = \left(\frac{1}{Re_L} \right) \left(\frac{1}{2Tx/x_0} \right) \left\{ \frac{d}{d\eta} \left(\frac{kT'}{T} \right) + \gamma_e M_e^2 \left(\frac{\mu}{T} \right) (f'')^2 \right\} \quad (3.30)$$

Simplifying (while using $x_0 = Re_L$),

$$ff'' + \frac{d}{d\eta} \left(\frac{\mu f''}{T} \right) = 0 \quad (3.31)$$

$$fc_p T' + \frac{d}{d\eta} \left(\frac{kT'}{T} \right) + \gamma_e M_e^2 \left(\frac{\mu}{T} \right) (f'')^2 = 0 \quad (3.32)$$

If the specific heat and the Prandtl number are constant, then $c_p = \gamma_e/(\gamma_e - 1)$ and $k = \mu c_p/Pr$ so that

$$ff'' + \frac{d}{d\eta} \left(\frac{\mu f''}{T} \right) = 0 \quad (3.33)$$

$$fT' + \frac{1}{Pr} \frac{d}{d\eta} \left(\frac{\mu T'}{T} \right) + (\gamma_e - 1) M_e^2 \left(\frac{\mu}{T} \right) (f'')^2 = 0 \quad (3.34)$$

These equations were solved using the Chebyshev spectral collocation technique in the `bstate.ins` file for the stability analysis.

3.2 Stability Analysis

This section describes some stability analyses of the flat plate compressible boundary layer. Two different coordinate systems are used in conjunction with three different sets of dependent variables. Parallel, quasi-parallel, and PSE calculations are done for most of the cases. Finally, some nonlinear PSE computations are compared with the results of a linear secondary stability analysis (El Hady [1991]).

3.2.1 Coordinate Systems

Both a rectilinear grid and one obtained from the similarity transformation are used. Since the rectilinear grid makes use of some of the similarity transformation relations, the similarity transformation is presented first.

Similarity Transformation

The similarity transformation has already been described for the most part (equations (3.13), (3.14), and (3.15)). These equations are presented again here for convenience:

$$x = \xi \quad (3.35)$$

$$y = \sqrt{\frac{2x}{x_0}} \int_0^\eta T(s) ds \quad (3.36)$$

Again, $T = T(\eta)$ is assumed to be a function only of η and not of x . Remember too that $x_0 = Re_L$ with the present choice of length scale: $L_0^* = \sqrt{x_0^* \mu_e^* / \rho_e^* U_e^*}$.

The derivative matrix of x and y with respect to ξ and η is

$$\begin{pmatrix} \frac{\partial x}{\partial \xi} & \frac{\partial x}{\partial \eta} \\ \frac{\partial y}{\partial \xi} & \frac{\partial y}{\partial \eta} \end{pmatrix} = \begin{pmatrix} 1 & 0 \\ \frac{1}{2x} \sqrt{\frac{2x}{x_0}} \int_0^\eta T(s) ds & \sqrt{\frac{2x}{x_0}} T(\eta) \end{pmatrix} \quad (3.37)$$

and its inverse is:

$$\begin{pmatrix} \frac{\partial \xi}{\partial x} & \frac{\partial \xi}{\partial y} \\ \frac{\partial \eta}{\partial x} & \frac{\partial \eta}{\partial y} \end{pmatrix} = \begin{pmatrix} 1 & 0 \\ \frac{-1}{2xT} \int_0^\eta T(s) ds & \frac{1}{\sqrt{2x/x_0 T(\eta)}} \end{pmatrix} \quad (3.38)$$

The second derivatives of $x = x^1$ and $y = x^2$ with respect to $\xi = \xi^1, \eta = \xi^2$ are:

$$\left[\frac{\partial^2 x}{\partial \xi^i \partial \xi^j} \right] = \begin{pmatrix} 0 & 0 \\ 0 & 0 \end{pmatrix} \quad (3.39)$$

$$\left[\frac{\partial^2 y}{\partial \xi^i \partial \xi^j} \right] = \begin{pmatrix} \frac{-1}{4x^2} \sqrt{\frac{2x}{x_0}} \int_0^\eta T(s) ds & \frac{1}{2x} \sqrt{\frac{2x}{x_0}} T(\eta) \\ \frac{1}{2x} \sqrt{\frac{2x}{x_0}} T(\eta) & \sqrt{\frac{2x}{x_0}} T'(\eta) \end{pmatrix} \quad (3.40)$$

The third derivatives of y with respect to $\xi = \xi^1, \eta = \xi^2$ are:

$$\frac{\partial}{\partial \xi} \left[\frac{\partial^2 y}{\partial \xi^i \partial \xi^j} \right] = \begin{pmatrix} \frac{3}{8x^3} \sqrt{\frac{2x}{x_0}} \int_0^\eta T(s) ds & \frac{-1}{4x^2} \sqrt{\frac{2x}{x_0}} T(\eta) \\ \frac{-1}{4x^2} \sqrt{\frac{2x}{x_0}} T(\eta) & \frac{1}{2x} \sqrt{\frac{2x}{x_0}} T'(\eta) \end{pmatrix} \quad (3.41)$$

$$\frac{\partial}{\partial \eta} \left[\frac{\partial^2 y}{\partial \xi^i \partial \xi^j} \right] = \begin{pmatrix} \frac{-1}{4x^2} \sqrt{\frac{2x}{x_0}} T(\eta) & \frac{1}{2x} \sqrt{\frac{2x}{x_0}} T'(\eta) \\ \frac{1}{2x} \sqrt{\frac{2x}{x_0}} T'(\eta) & \sqrt{\frac{2x}{x_0}} T''(\eta) \end{pmatrix} \quad (3.42)$$

The covariant and contravariant components of the metric tensor as well as the Christoffel symbols of the first and second kinds are given here too. The derivatives of many of these quantities are also given. They are not needed as input in any way; they are included for comparison to the values which are computed by the program. In fact, the computed results were compared with those given here using the UNIX debugger - they are in complete agreement.

The covariant components of the metric tensor are

$$[g_{ij}] \equiv \left[\frac{\partial x^k}{\partial \xi^i} \frac{\partial x^k}{\partial \xi^j} \right] = \begin{pmatrix} 1 + \frac{1}{2x^2} \left(\frac{x}{x_0} \right) \{ \int_0^\eta T(s) ds \}^2 & \frac{T(\eta)}{x_0} \int_0^\eta T(s) ds \\ \frac{T(\eta)}{x_0} \int_0^\eta T(s) ds & 2 \left(\frac{x}{x_0} \right) T^2(\eta) \end{pmatrix} \quad (3.43)$$

The contravariant components of the metric tensor are

$$[g^{ij}] \equiv [g_{ij}]^{-1} = \begin{pmatrix} 1 & \frac{-1}{2xT(\eta)} \int_0^\eta T(s) ds \\ \frac{-1}{2xT(\eta)} \int_0^\eta T(s) ds & \frac{1}{2(x/x_0)T^2(\eta)} + \left\{ \frac{1}{2xT(\eta)} \int_0^\eta T(s) ds \right\}^2 \end{pmatrix} \quad (3.44)$$

The Jacobian of the coordinate transformation is

$$J \equiv \sqrt{g} \equiv \sqrt{\det[g_{ij}]} = \sqrt{\frac{2x}{x_0}} T(\eta) \quad (3.45)$$

Hence,

$$\ln(\sqrt{g}) = \ln(\sqrt{2}) + \frac{1}{2} \ln(x) - \frac{1}{2} \ln(x_0) + \ln(T(\eta)) \quad (3.46)$$

and

$$\frac{\partial \ln(\sqrt{g})}{\partial \xi^i} = \left(\frac{1}{2x} , \frac{T'(\eta)}{T(\eta)} \right) \quad (3.47)$$

$$\left[\frac{\partial^2 \ln(\sqrt{g})}{\partial \xi^i \partial \xi^j} \right] = \begin{pmatrix} \frac{-1}{2x^2} & 0 \\ 0 & \frac{1}{T(\eta)} \left(T''(\eta) - \frac{(T'(\eta))^2}{T(\eta)} \right) \end{pmatrix} \quad (3.48)$$

The Christoffel symbols of the first kind are defined by

$$[st, p] = \frac{1}{2} \left(\frac{\partial g_{tp}}{\partial \xi^s} + \frac{\partial g_{ps}}{\partial \xi^t} - \frac{\partial g_{st}}{\partial \xi^p} \right) \quad (3.49)$$

They are symmetric in s and t . The nonzero elements for the similarity transformation are:

$$[11, 1] = \frac{-1}{4x^2 x_0} \left\{ \int_0^\eta T(s) ds \right\}^2 \quad (3.50)$$

$$[12, 1] = \frac{T(\eta)}{2x x_0} \int_0^\eta T(s) ds \quad (3.51)$$

$$[22, 1] = \frac{T'(\eta)}{x_0} \int_0^\eta T(s) ds \quad (3.52)$$

$$[11, 2] = \frac{-T(\eta)}{2x x_0} \int_0^\eta T(s) ds \quad (3.53)$$

$$[12, 2] = \frac{T^2(\eta)}{x_0} \quad (3.54)$$

$$[22, 2] = 2 \left(\frac{x}{x_0} \right) T'(\eta) T(\eta) \quad (3.55)$$

The Christoffel symbols of the second kind are defined by

$$\left\{ \begin{array}{c} r \\ s \ t \end{array} \right\} \equiv g^{rp} [st, p] \quad (3.56)$$

They are also symmetric in s and t . The nonzero elements for the similarity transformation are:

$$\left\{ \begin{array}{c} 2 \\ 1 \ 1 \end{array} \right\} = \frac{-1}{4x^2 T(\eta)} \int_0^\eta T(s) ds \quad (3.57)$$

$$\left\{ \begin{array}{c} 2 \\ 1 \ 2 \end{array} \right\} = \frac{1}{2x} \quad (3.58)$$

$$\left\{ \begin{array}{c} 2 \\ 2 \ 2 \end{array} \right\} = \frac{T'(\eta)}{T(\eta)} \quad (3.59)$$

The derivatives of the Christoffel symbols of the second kind with respect to ξ and η are:

$$\frac{\partial}{\partial \xi^i} \left\{ \begin{array}{c} 2 \\ 1 \ 1 \end{array} \right\} = \left(\frac{1}{2x^3 T(\eta)} \int_0^\eta T(s) ds, \ \frac{-1}{4x^2 T(\eta)} \left(T(\eta) - \frac{T'(\eta)}{T(\eta)} \int_0^\eta T(s) ds \right) \right) \quad (3.60)$$

$$\frac{\partial}{\partial \xi^i} \left\{ \begin{array}{c} 2 \\ 1 \ 2 \end{array} \right\} = \left(\frac{-1}{2x^3}, \ 0 \right) \quad (3.61)$$

$$\frac{\partial}{\partial \xi^i} \left\{ \begin{array}{c} 2 \\ 2 \ 2 \end{array} \right\} = \left(0, \ \frac{1}{T(\eta)} \left(T''(\eta) - \frac{(T'(\eta))^2}{T(\eta)} \right) \right) \quad (3.62)$$

Again, all of the above values are computed correctly by the files used with the programs LSH and PSX.

Rectilinear Coordinate System

The rectilinear coordinate system is defined by the transformation

$$\tilde{\xi} = \xi = x \quad (3.63)$$

$$\tilde{\eta} = \eta(x_0, y) \quad (3.64)$$

Hence,

$$\begin{pmatrix} \frac{\partial \tilde{\xi}}{\partial x} & \frac{\partial \tilde{\xi}}{\partial y} \\ \frac{\partial \tilde{\eta}}{\partial x} & \frac{\partial \tilde{\eta}}{\partial y} \end{pmatrix} = \begin{pmatrix} 1 & 0 \\ 0 & \frac{\partial \eta}{\partial y}(x_0, y) \end{pmatrix} \quad (3.65)$$

Higher derivatives are computed similarly and are not given here. However, since the basic state is computed in terms of ξ and η , it is convenient to figure out the transformation laws between the ξ, η and the $\tilde{\xi}, \tilde{\eta}$ coordinates. These transformation laws are given below.

$$\frac{\partial \tilde{\xi}}{\partial \xi} = 1 \quad (3.66)$$

$$\frac{\partial \tilde{\xi}}{\partial \eta} = 0 \quad (3.67)$$

$$\frac{\partial \tilde{\eta}}{\partial \xi} = \frac{\partial \tilde{\eta}}{\partial x} \frac{\partial x}{\partial \xi} + \frac{\partial \tilde{\eta}}{\partial y} \frac{\partial y}{\partial \xi} \quad (3.68)$$

$$\frac{\partial \tilde{\eta}}{\partial \eta} = \frac{\partial \tilde{\eta}}{\partial x} \frac{\partial x}{\partial \eta} + \frac{\partial \tilde{\eta}}{\partial y} \frac{\partial y}{\partial \eta} \quad (3.69)$$

$$(3.70)$$

or, using (3.65),

$$\begin{pmatrix} \frac{\partial \tilde{\xi}}{\partial \xi} & \frac{\partial \tilde{\xi}}{\partial \eta} \\ \frac{\partial \tilde{\eta}}{\partial \xi} & \frac{\partial \tilde{\eta}}{\partial \eta} \end{pmatrix} = \begin{pmatrix} 1 & 0 \\ \frac{\partial \eta}{\partial y}(x_0, y) \frac{\partial y}{\partial \xi}(x, y) & \frac{\partial \eta}{\partial y}(x_0, y) \frac{\partial y}{\partial \eta}(x, y) \end{pmatrix} \quad (3.71)$$

The inverse of this matrix is:

$$\begin{pmatrix} \frac{\partial \xi}{\partial \tilde{\xi}} & \frac{\partial \xi}{\partial \tilde{\eta}} \\ \frac{\partial \eta}{\partial \tilde{\xi}} & \frac{\partial \eta}{\partial \tilde{\eta}} \end{pmatrix} = \begin{pmatrix} 1 & 0 \\ -\frac{\partial y}{\partial \tilde{\xi}}(x, y) / \frac{\partial y}{\partial \tilde{\eta}}(x, y) & 1 / \left\{ \frac{\partial y}{\partial \tilde{\eta}}(x_0, y) \frac{\partial y}{\partial \tilde{\xi}}(x, y) \right\} \end{pmatrix} \quad (3.72)$$

or, using (3.37),

$$\begin{pmatrix} \frac{\partial \xi}{\partial \tilde{\xi}} & \frac{\partial \xi}{\partial \tilde{\eta}} \\ \frac{\partial \eta}{\partial \tilde{\xi}} & \frac{\partial \eta}{\partial \tilde{\eta}} \end{pmatrix} = \begin{pmatrix} 1 & 0 \\ \frac{-1}{2xT(\eta)} \int_0^{\eta(x,y)} T(s) ds & \frac{T(\eta(x_0,y))}{\sqrt{x/x_0 T(\eta(x,y))}} \end{pmatrix} \quad (3.73)$$

$$= \begin{pmatrix} 1 & 0 \\ \frac{-1}{2xT(\eta)} \int_0^{\eta} T(s) ds & \frac{T(\tilde{\eta})}{\sqrt{x/x_0 T(\eta)}} \end{pmatrix} \quad (3.74)$$

The chain rule transformation law:

$$\frac{\partial}{\partial \tilde{\xi}} = \frac{\partial}{\partial \xi} \frac{\partial \xi}{\partial \tilde{\xi}} + \frac{\partial}{\partial \eta} \frac{\partial \eta}{\partial \tilde{\xi}} \quad (3.75)$$

$$\frac{\partial}{\partial \tilde{\eta}} = \frac{\partial}{\partial \xi} \frac{\partial \xi}{\partial \tilde{\eta}} + \frac{\partial}{\partial \eta} \frac{\partial \eta}{\partial \tilde{\eta}} \quad (3.76)$$

is thus:

$$\frac{\partial}{\partial \tilde{\xi}} = \frac{\partial}{\partial \xi} - \frac{1}{2xT(\eta)} \int_0^\eta T(s)ds \frac{\partial}{\partial \eta} \quad (3.77)$$

$$\frac{\partial}{\partial \tilde{\eta}} = \frac{T(\tilde{\eta})}{\sqrt{x/x_0 T(\eta)}} \frac{\partial}{\partial \eta} \quad (3.78)$$

The second derivative operators can be shown to be

$$\begin{aligned} \frac{\partial^2}{\partial \tilde{\xi}^2} &= \frac{\partial^2}{\partial \xi^2} + \frac{\int_0^\eta T(s)ds}{(2xT(\eta))^2} \left(3T(\eta) - \frac{T'(\eta)}{T(\eta)} \int_0^\eta T(s)ds \right) \frac{\partial}{\partial \eta} \\ &\quad - \frac{2}{2xT(\eta)} \int_0^\eta T(s)ds \frac{\partial^2}{\partial \xi \partial \eta} + \left\{ \frac{1}{2xT(\eta)} \int_0^\eta T(s)ds \right\}^2 \frac{\partial^2}{\partial \eta^2} \end{aligned} \quad (3.79)$$

$$\begin{aligned} \frac{\partial^2}{\partial \tilde{\xi} \partial \tilde{\eta}} &= \frac{T(\tilde{\eta})}{\sqrt{x/x_0 T(\eta)}} \left[\frac{\partial^2}{\partial \xi \partial \eta} + \frac{1}{2x} \left\{ \frac{T'(\eta)}{T^2(\eta)} \int_0^\eta T(s)ds - 1 \right\} \frac{\partial}{\partial \eta} \right] \end{aligned} \quad (3.80)$$

$$- \frac{1}{2xT(\eta)} \int_0^\eta T(s)ds \frac{\partial^2}{\partial \eta^2} \quad (3.81)$$

$$\begin{aligned} \frac{\partial^2}{\partial \tilde{\eta}^2} &= \frac{1}{\sqrt{x/x_0}} \left[\frac{T'(\tilde{\eta})}{T(\eta)} - \frac{1}{\sqrt{x/x_0}} \left(\frac{T(\tilde{\eta})}{T(\eta)} \right)^2 \frac{T'(\eta)}{T(\eta)} \right] \frac{\partial}{\partial \eta} \end{aligned} \quad (3.82)$$

$$+ \left\{ \frac{T(\tilde{\eta})}{\sqrt{x/x_0 T(\eta)}} \right\}^2 \frac{\partial^2}{\partial \eta^2} \quad (3.83)$$

This coordinate system was only used in actual computations for the local analyses (parallel, quasi-parallel). Similarity and Cartesian coordinates are used for the PSE calculations.

3.2.2 Dependent Disturbance State Variables

As mentioned at the beginning of this section, three different sets of dependent variables can be used.

The first set is: $(\tilde{p}, \tilde{T}, \tilde{u}, \tilde{v}, \tilde{w})$, where p is the pressure, T the temperature, and $\tilde{u}, \tilde{v}, \tilde{w}$ the velocity components in the x, y , and z (spanwise) coordinate directions, respectively. The $\tilde{\cdot}$ overstrike denotes the disturbance. These variables will be subsequently referred to as *primitive variables*.

The second set is $(\tilde{p} - \tilde{\rho}T_w/(\gamma_e M_e^2), \tilde{\rho}, \tilde{\rho}\tilde{u}, \tilde{\rho}\tilde{v}, \tilde{\rho}\tilde{w})$. Again, T_w is the basic state wall temperature. Assuming that the equation of state is the ideal gas law, the first disturbance variable is proportional to the disturbance temperature and, hence, is zero at the wall. This first variable is used instead of the pressure itself because the spectral code requires that the boundary conditions for each variable be the same at each boundary. With this restriction, if \tilde{p} and $\tilde{\rho}$ were used as the disturbance thermodynamic variables there would be no means of enforcing the wall temperature boundary condition.

The second choice of dependent variables makes the inviscid terms in the original governing equations homogeneous functions of degree one and the viscous terms homogeneous functions of degree zero. (See, for instance, Gelfand and Fomin [1963] for a definition of homogeneous functions of degree k . See also Schiff and Steger, [1979].) These variables were mainly used as a programming stepping stone to the third choice. They will be subsequently referred to as *conservative variables*.

The third set of dependent variables is $\sqrt{g}(\tilde{p} - \tilde{\rho}T_w/(\gamma_e M_e^2), \tilde{\rho}, \tilde{\rho}\tilde{v}^1, \tilde{\rho}\tilde{v}^2, \tilde{\rho}\tilde{v}^3)$. Here v^1 , v^2 , and v^3 are the contravariant velocity components:

$$v^i = \frac{\partial \xi^i}{\partial x} u + \frac{\partial \xi^i}{\partial y} v + \frac{\partial \xi^i}{\partial z} w + \frac{\partial \xi^i}{\partial t} \quad (3.84)$$

These variables will be subsequently referred to as *scaled conservative variables*.

The third choice is available made because the continuity equation in general curvilinear coordinates is linear in these variables. In fact, all of the coefficients of the dependent variables in the continuity equation are constant. Hence, the disturbance satisfies conservation of mass exactly (and uniformly) even when the parallel flow approximation is made. (The parallel flow approximation still is required because of nonparallel terms in the momentum and energy equations.)

The main input required for each of these sets of disturbance variables is the matrix M_j^i . This matrix transforms the original (default) disturbance dependent variables $\tilde{Q} = (\tilde{Q}^1, \tilde{Q}^2, \tilde{Q}^3, \tilde{Q}^4, \tilde{Q}^5) = (\tilde{p}, \tilde{T}, \tilde{u}, \tilde{v}, \tilde{w})$ into the new dependent variables:

$$\tilde{Q}^i = M_j^i(\mathbf{x}, t) f^j(\xi, \tau) \exp(i\theta(\xi^1, \xi^3, \tau)) + \text{complex conjugate} \quad (3.85)$$

The matrix M_j^i for each set of disturbance variables is given in the following subsections.

Primitive Variables

In this case, the matrix M_j^i is particularly simple: it is just the identity matrix

$$M_j^i = \begin{cases} 1 & \text{if } i = j \\ 0 & \text{if } i \neq j \end{cases} \quad (3.86)$$

All of its spatial and temporal derivatives are zero.

Conservative Variables

The matrix M_j^i for the conservative variables is

$$[M_j^i] = \begin{pmatrix} 1 & \frac{T_w}{\gamma_e M_e^2} & 0 & 0 & 0 \\ -\frac{\partial \rho / \partial p}{\partial \rho / \partial T} & \frac{1}{\partial \rho / \partial T} - \left(\frac{\partial \rho / \partial p}{\partial \rho / \partial T} \right) \left(\frac{T_w}{\gamma_e M_e^2} \right) & 0 & 0 & 0 \\ 0 & -\frac{u}{\rho} & \frac{1}{\rho} & 0 & 0 \\ 0 & -\frac{v}{\rho} & 0 & \frac{1}{\rho} & 0 \\ 0 & -\frac{w}{\rho} & 0 & 0 & \frac{1}{\rho} \end{pmatrix} \quad (3.87)$$

The spatial and temporal first and second derivatives of this matrix can be computed using the chain rule and the derivatives of the basic state. The derivatives of the basic state are given in Section 3.2.3.

Scaled Conservative Variables

The matrix M_j^i for the scaled conservative variables is

$$[M_j^i] = \frac{1}{\sqrt{g}} \begin{pmatrix} 1 & \frac{T_w}{\gamma_e M_e^2} & 0 & 0 & 0 \\ -\frac{\partial \rho / \partial p}{\partial \rho / \partial T} & \frac{1}{\partial \rho / \partial T} - \left(\frac{\partial \rho / \partial p}{\partial \rho / \partial T} \right) \left(\frac{T_w}{\gamma_e M_e^2} \right) & 0 & 0 & 0 \\ 0 & -\frac{u}{\rho} & \frac{1}{\rho} \frac{\partial x}{\partial \xi^1} & \frac{1}{\rho} \frac{\partial x}{\partial \xi^2} & \frac{1}{\rho} \frac{\partial x}{\partial \xi^3} \\ 0 & -\frac{v}{\rho} & \frac{1}{\rho} \frac{\partial y}{\partial \xi^1} & \frac{1}{\rho} \frac{\partial y}{\partial \xi^2} & \frac{1}{\rho} \frac{\partial y}{\partial \xi^3} \\ 0 & -\frac{w}{\rho} & \frac{1}{\rho} \frac{\partial z}{\partial \xi^1} & \frac{1}{\rho} \frac{\partial z}{\partial \xi^2} & \frac{1}{\rho} \frac{\partial z}{\partial \xi^3} \end{pmatrix} \quad (3.88)$$

(Note that even if the grid is time dependent (i.e., $\partial x / \partial \tau \neq 0$, etc.), as long as $\tau = t$ and there is no disturbance in the grid speed, the disturbance in the fourth contravariant velocity component $v^4 = 1 + u \partial \tau / \partial x + v \partial \tau / \partial y + w \partial \tau / \partial z$ is identically zero.) The spatial and temporal first and second derivatives of this matrix can be computed using the chain rule and the derivatives of the grid and basic state. The derivatives of the grid were given earlier in Section 3.2.1. The derivatives of the basic state are given in Section 3.2.3.

3.2.3 Basic State for Parallel and Quasi-Parallel Flows

The basic state and its spatial and temporal derivatives must also be specified for the stability analysis. The particular values assigned depend upon whether the parallel or quasi-parallel flow approximation is made. Also, the directions in which the derivatives are taken depend upon the coordinate system used. Since the basic state is computed using the similarity coordinates, its derivatives in this coordinate system are presented first.

Basic State Derivatives in Similarity Coordinates

The similarity coordinate system has already been described in Section 3.2.1. Also, the dependence of the basic state on these coordinates has been described in Section 3.1.1. In particular,

$$p = \rho(\eta)T(\eta)/(\gamma_e M_e^2) = 1/(\gamma_e M_e^2) \quad (3.89)$$

$$T = T(\eta) \quad (3.90)$$

$$\rho = 1/T(\eta) \quad (3.91)$$

$$u = f'(\eta) \quad (3.92)$$

$$v = \frac{1}{2x} \sqrt{\frac{2x}{x_0}} \left(f'(\eta) \int_0^\eta T(s) ds - f(\eta)T(\eta) \right) \quad (3.93)$$

$$w = 0 \quad (3.94)$$

(See equations (3.13), (3.25), and (3.26).) Hence,

$$\frac{\partial p}{\partial \xi} = 0 \quad (3.95)$$

$$\frac{\partial T}{\partial \xi} = 0 \quad (3.96)$$

$$\frac{\partial u}{\partial \xi} = 0 \quad (3.97)$$

$$\frac{\partial v}{\partial \xi} = -\frac{v}{2x} \quad (3.98)$$

$$\frac{\partial w}{\partial \xi} = 0 \quad (3.99)$$

and

$$\frac{\partial p}{\partial \eta} = 0 \quad (3.100)$$

$$\frac{\partial T}{\partial \eta} = T'(\eta) \quad (3.101)$$

$$\frac{\partial u}{\partial \eta} = f''(\eta) \quad (3.102)$$

$$\frac{\partial v}{\partial \eta} = \frac{1}{2x} \sqrt{\frac{2x}{x_0}} \left(f''(\eta) \int_0^\eta T(s) ds - f(\eta)T'(\eta) \right) \quad (3.103)$$

$$\frac{\partial w}{\partial \eta} = 0 \quad (3.104)$$

The second derivatives are

$$\frac{\partial^2 p}{\partial \xi^2} = 0 \quad (3.105)$$

$$\frac{\partial^2 T}{\partial \xi^2} = 0 \quad (3.106)$$

$$\frac{\partial^2 u}{\partial \xi^2} = 0 \quad (3.107)$$

$$\frac{\partial^2 v}{\partial \xi^2} = \frac{3v}{4x^2} \quad (3.108)$$

$$\frac{\partial^2 w}{\partial \xi^2} = 0 \quad (3.109)$$

$$\frac{\partial^2 p}{\partial \xi \partial \eta} = 0 \quad (3.110)$$

$$\frac{\partial^2 T}{\partial \xi \partial \eta} = 0 \quad (3.111)$$

$$\frac{\partial^2 u}{\partial \xi \partial \eta} = 0 \quad (3.112)$$

$$\frac{\partial^2 v}{\partial \xi \partial \eta} = -\frac{1}{2x} \frac{\partial v}{\partial \eta} \quad (3.113)$$

$$\frac{\partial^2 w}{\partial \xi \partial \eta} = 0 \quad (3.114)$$

$$\frac{\partial^2 p}{\partial \eta^2} = 0 \quad (3.115)$$

$$\frac{\partial^2 T}{\partial \eta^2} = T''(\eta) \quad (3.116)$$

$$\frac{\partial^2 u}{\partial \eta^2} = f'''(\eta) \quad (3.117)$$

$$\begin{aligned} \frac{\partial^2 v}{\partial \eta^2} = \frac{1}{2x} \sqrt{\frac{2x}{x_0}} & \left(f'''(\eta) \int_0^\eta T(s) ds + f''(\eta) T(\eta) \right. \\ & \left. - f'(\eta) T'(\eta) - f(\eta) T''(\eta) \right) \end{aligned} \quad (3.118)$$

$$\frac{\partial^2 w}{\partial \eta^2} = 0 \quad (3.119)$$

Basic State Derivatives in Rectilinear Coordinates

The values assigned to the basic state and its derivatives in the rectilinear coordinate system depend upon whether the parallel or quasi-parallel flow approximation is made.

Parallel Flow

When the basic state flow is approximated as being *locally* parallel, it depends only upon the coordinate y ; it is independent of x . Equivalently, it depends only upon $\tilde{\eta}$; it is independent of ξ . (See equations (3.63) and (3.64).) Hence,

$$p = \rho(\eta)T(\eta)/(\gamma_e M_e^2) = 1/(\gamma_e M_e^2) \quad (3.120)$$

$$T = T(\eta) \quad (3.121)$$

$$u = u(\eta) \quad (3.122)$$

$$v = 0 \quad (3.123)$$

$$w = 0 \quad (3.124)$$

Hence,

$$\frac{\partial p}{\partial \xi} = 0 \quad (3.125)$$

$$\frac{\partial T}{\partial \xi} = 0 \quad (3.126)$$

$$\frac{\partial u}{\partial \xi} = 0 \quad (3.127)$$

$$\frac{\partial v}{\partial \xi} = 0 \quad (3.128)$$

$$\frac{\partial w}{\partial \xi} = 0 \quad (3.129)$$

$$\frac{\partial p}{\partial \tilde{\eta}} = 0 \quad (3.130)$$

$$\frac{\partial T}{\partial \tilde{\eta}} = \frac{T(\tilde{\eta})}{\sqrt{x/x_0 T(\eta)}} T'(\eta) \quad (3.131)$$

$$\frac{\partial u}{\partial \tilde{\eta}} = \frac{T(\tilde{\eta})}{\sqrt{x/x_0 T(\eta)}} f''(\eta) \quad (3.132)$$

$$\frac{\partial v}{\partial \tilde{\eta}} = 0 \quad (3.133)$$

$$\frac{\partial w}{\partial \tilde{\eta}} = 0 \quad (3.134)$$

$$\frac{\partial^2 p}{\partial \xi^2} = 0 \quad (3.135)$$

$$\frac{\partial^2 T}{\partial \xi^2} = 0 \quad (3.136)$$

$$\frac{\partial^2 u}{\partial \tilde{\xi}^2} = 0 \quad (3.137)$$

$$\frac{\partial^2 v}{\partial \tilde{\xi}^2} = 0 \quad (3.138)$$

$$\frac{\partial^2 w}{\partial \tilde{\xi}^2} = 0 \quad (3.139)$$

$$\frac{\partial^2 p}{\partial \tilde{\xi} \partial \tilde{\eta}} = 0 \quad (3.140)$$

$$\frac{\partial^2 T}{\partial \tilde{\xi} \partial \tilde{\eta}} = 0 \quad (3.141)$$

$$\frac{\partial^2 u}{\partial \tilde{\xi} \partial \tilde{\eta}} = 0 \quad (3.142)$$

$$\frac{\partial^2 v}{\partial \tilde{\xi} \partial \tilde{\eta}} = 0 \quad (3.143)$$

$$\frac{\partial^2 w}{\partial \tilde{\xi} \partial \tilde{\eta}} = 0 \quad (3.144)$$

$$\frac{\partial^2 p}{\partial \tilde{\eta}^2} = 0 \quad (3.145)$$

$$\begin{aligned} \frac{\partial^2 T}{\partial \tilde{\eta}^2} &= \frac{1}{\sqrt{x/x_0}} \left[\frac{T'(\tilde{\eta})}{T(\eta)} - \frac{1}{\sqrt{x/x_0}} \left(\frac{T(\tilde{\eta})}{T(\eta)} \right)^2 \frac{T'(\eta)}{T(\eta)} \right] T'(\eta) \\ &\quad + \left\{ \frac{T(\tilde{\eta})}{\sqrt{x/x_0} T(\eta)} \right\}^2 T''(\eta) \end{aligned} \quad (3.146)$$

$$\begin{aligned} \frac{\partial^2 u}{\partial \tilde{\eta}^2} &= \frac{1}{\sqrt{x/x_0}} \left[\frac{T'(\tilde{\eta})}{T(\eta)} - \frac{1}{\sqrt{x/x_0}} \left(\frac{T(\tilde{\eta})}{T(\eta)} \right)^2 \frac{T'(\eta)}{T(\eta)} \right] f''(\eta) \\ &\quad + \left\{ \frac{T(\tilde{\eta})}{\sqrt{x/x_0} T(\eta)} \right\}^2 f'''(\eta) \end{aligned} \quad (3.147)$$

$$\begin{aligned} \frac{\partial^2 v}{\partial \tilde{\eta}^2} &= \frac{1}{\sqrt{x/x_0}} \left[\frac{T'(\tilde{\eta})}{T(\eta)} - \frac{1}{\sqrt{x/x_0}} \left(\frac{T(\tilde{\eta})}{T(\eta)} \right)^2 \frac{T'(\eta)}{T(\eta)} \right] \frac{\partial v}{\partial \eta} \\ &\quad + \left\{ \frac{T(\tilde{\eta})}{\sqrt{x/x_0} T(\eta)} \right\}^2 \frac{\partial^2 v}{\partial \eta^2} \end{aligned} \quad (3.148)$$

$$\frac{\partial^2 w}{\partial \tilde{\eta}^2} = 0 \quad (3.149)$$

Quasi-Parallel Flow

When the basic state flow is approximated as being quasi-parallel, all of the coefficients in the disturbance equations which are functions of x are assumed to be locally constant. In other words, they are retained in the equations, but are assumed constant and evaluated at the particular station where the local stability analysis is performed. In this case,

$$p = \rho(\eta)T(\eta)/(\gamma_e M_e^2) = 1/(\gamma_e M_e^2) \quad (3.150)$$

$$T = T(\eta) \quad (3.151)$$

$$\rho = 1/T(\eta) \quad (3.152)$$

$$u = f'(\eta) \quad (3.153)$$

$$v = \frac{1}{2x} \sqrt{\frac{2x}{x_0}} \left(f'(\eta) \int_0^\eta T(s)ds - f(\eta)T(\eta) \right) \quad (3.154)$$

$$w = 0 \quad (3.155)$$

(See equations (3.13), (3.25), and (3.26).) Applying the transformation laws (3.77), (3.78), (3.79), (3.81), and (3.83) to this approximation of the basic state yields:

$$\frac{\partial p}{\partial \tilde{\xi}} = 0 \quad (3.156)$$

$$\frac{\partial T}{\partial \tilde{\xi}} = -\frac{T'(\eta)}{2xT(\eta)} \int_0^\eta T(s)ds \quad (3.157)$$

$$\frac{\partial u}{\partial \tilde{\xi}} = -\frac{f''(\eta)}{2xT(\eta)} \int_0^\eta T(s)ds \quad (3.158)$$

$$\frac{\partial v}{\partial \tilde{\xi}} = \frac{\partial v}{\partial \xi} - \frac{1}{2xT(\eta)} \int_0^\eta T(s)ds \frac{\partial v}{\partial \eta} \quad (3.159)$$

$$\frac{\partial w}{\partial \tilde{\xi}} = 0 \quad (3.160)$$

$$\frac{\partial p}{\partial \tilde{\eta}} = 0 \quad (3.161)$$

$$\frac{\partial T}{\partial \tilde{\eta}} = \frac{T(\tilde{\eta})}{\sqrt{x/x_0}T(\eta)} T'(\eta) \quad (3.162)$$

$$\frac{\partial u}{\partial \tilde{\eta}} = \frac{T(\tilde{\eta})}{\sqrt{x/x_0}T(\eta)} f''(\eta) \quad (3.163)$$

$$\frac{\partial v}{\partial \tilde{\eta}} = \frac{T(\tilde{\eta})}{\sqrt{x/x_0}T(\eta)} \frac{\partial v}{\partial \eta}(\xi, \eta) \quad (3.164)$$

$$\frac{\partial w}{\partial \tilde{\eta}} = 0 \quad (3.165)$$

The second derivatives are:

$$\frac{\partial^2 p}{\partial \tilde{\xi}^2} = 0 \quad (3.166)$$

$$\begin{aligned} \frac{\partial^2 T}{\partial \tilde{\xi}^2} &= T'(\eta) \frac{\int_0^\eta T(s)ds}{(2xT(\eta))^2} \left(3T(\eta) - \frac{T'(\eta)}{T(\eta)} \int_0^\eta T(s)ds \right) \\ &\quad + \left\{ \frac{1}{2xT(\eta)} \int_0^\eta T(s)ds \right\}^2 T''(\eta) \end{aligned} \quad (3.167)$$

$$\begin{aligned} \frac{\partial^2 u}{\partial \tilde{\xi}^2} &= f''(\eta) \frac{\int_0^\eta T(s)ds}{(2xT(\eta))^2} \left(3T(\eta) - \frac{T'(\eta)}{T(\eta)} \int_0^\eta T(s)ds \right) \\ &\quad + \left\{ \frac{1}{2xT(\eta)} \int_0^\eta T(s)ds \right\}^2 f'''(\eta) \end{aligned} \quad (3.168)$$

$$\begin{aligned} \frac{\partial^2 v}{\partial \tilde{\xi}^2} &= \frac{\partial^2 v}{\partial \xi^2} + \frac{\int_0^\eta T(s)ds}{(2xT(\eta))^2} \left(3T(\eta) - \frac{T'(\eta)}{T(\eta)} \int_0^\eta T(s)ds \right) \frac{\partial v}{\partial \eta} \\ &\quad - \frac{2}{2xT(\eta)} \int_0^\eta T(s)ds \frac{\partial^2 v}{\partial \xi \partial \eta} + \left\{ \frac{1}{2xT(\eta)} \int_0^\eta T(s)ds \right\}^2 \frac{\partial^2 v}{\partial \eta^2} \end{aligned} \quad (3.169)$$

$$\frac{\partial^2 w}{\partial \tilde{\xi}^2} = 0 \quad (3.170)$$

$$\frac{\partial^2 p}{\partial \tilde{\xi} \partial \tilde{\eta}} = 0 \quad (3.171)$$

$$\frac{\partial^2 T}{\partial \tilde{\xi} \partial \tilde{\eta}} = \frac{T(\tilde{\eta})}{\sqrt{x/x_0 T(\eta)}} \left[\frac{T'(\eta)}{2x} \left\{ \frac{T'(\eta)}{T^2(\eta)} \int_0^\eta T(s)ds - 1 \right\} \right. \quad (3.172)$$

$$\left. - \frac{T''(\eta)}{2xT(\eta)} \int_0^\eta T(s)ds \right] \quad (3.173)$$

$$\frac{\partial^2 u}{\partial \tilde{\xi} \partial \tilde{\eta}} = \frac{T(\tilde{\eta})}{\sqrt{x/x_0 T(\eta)}} \left[\frac{f''(\eta)}{2x} \left\{ \frac{T'(\eta)}{T^2(\eta)} \int_0^\eta T(s)ds - 1 \right\} \right. \quad (3.174)$$

$$\left. - \frac{f'''(\eta)}{2xT(\eta)} \int_0^\eta T(s)ds \right] \quad (3.175)$$

$$\frac{\partial^2 v}{\partial \tilde{\xi} \partial \tilde{\eta}} = \frac{T(\tilde{\eta})}{\sqrt{x/x_0 T(\eta)}} \left[\frac{\partial^2 v}{\partial \xi \partial \eta} + \frac{1}{2x} \left\{ \frac{T'(\eta)}{T^2(\eta)} \int_0^\eta T(s) ds - 1 \right\} \frac{\partial v}{\partial \eta} \right] \quad (3.176)$$

$$- \frac{1}{2x T(\eta)} \int_0^\eta T(s) ds \frac{\partial^2 v}{\partial \eta^2} \quad (3.177)$$

$$\frac{\partial^2 w}{\partial \tilde{\xi} \partial \tilde{\eta}} = 0 \quad (3.178)$$

$$\frac{\partial^2 p}{\partial \tilde{\eta}^2} = 0 \quad (3.179)$$

$$\begin{aligned} \frac{\partial^2 T}{\partial \tilde{\eta}^2} = & \frac{1}{\sqrt{x/x_0}} \left[\frac{T'(\tilde{\eta})}{T(\eta)} - \frac{1}{\sqrt{x/x_0}} \left(\frac{T(\tilde{\eta})}{T(\eta)} \right)^2 \frac{T'(\eta)}{T(\eta)} \right] T'(\eta) \\ & + \left\{ \frac{T(\tilde{\eta})}{\sqrt{x/x_0 T(\eta)}} \right\}^2 T''(\eta) \end{aligned} \quad (3.180)$$

$$\begin{aligned} \frac{\partial^2 u}{\partial \tilde{\eta}^2} = & \frac{1}{\sqrt{x/x_0}} \left[\frac{T'(\tilde{\eta})}{T(\eta)} - \frac{1}{\sqrt{x/x_0}} \left(\frac{T(\tilde{\eta})}{T(\eta)} \right)^2 \frac{T'(\eta)}{T(\eta)} \right] f''(\eta) \\ & + \left\{ \frac{T(\tilde{\eta})}{\sqrt{x/x_0 T(\eta)}} \right\}^2 f'''(\eta) \end{aligned} \quad (3.181)$$

$$\begin{aligned} \frac{\partial^2 v}{\partial \tilde{\eta}^2} = & \frac{1}{\sqrt{x/x_0}} \left[\frac{T'(\tilde{\eta})}{T(\eta)} - \frac{1}{\sqrt{x/x_0}} \left(\frac{T(\tilde{\eta})}{T(\eta)} \right)^2 \frac{T'(\eta)}{T(\eta)} \right] \frac{\partial v}{\partial \eta} \\ & + \left\{ \frac{T(\tilde{\eta})}{\sqrt{x/x_0 T(\eta)}} \right\}^2 \frac{\partial^2 v}{\partial \eta^2} \end{aligned} \quad (3.182)$$

$$\frac{\partial^2 w}{\partial \tilde{\eta}^2} = 0 \quad (3.183)$$

3.2.4 Computed Results

Some results are presented in this subsection. They were obtained using the Sutherland viscosity law for air, constant specific heat $c_p = \gamma_e / (\gamma_e - 1)$ (with $\gamma_e = 1.4$), and constant Prandtl number = 0.70. The transformation parameter η_0 was set to $4.5/\sqrt{2} \approx 3.181980516$ in order to make comparisons with results for the incompressible boundary layer.¹

¹where the definition of η does not include a factor of $\sqrt{2}$.

Parallel Flow, Rectilinear Coordinates

Primitive Variables

A special insert file for LSH was written to implement the equations for primitive variables in rectilinear coordinates in order to make direct comparisons between its results and those of the more general insert file. After debugging, both of them produced identical results (since they use the same formulation of the equations).

Particular flows investigated are some of those published in the literature by Malik (1990). The first is for a two-dimensional disturbance (Malik's test case #5): $M_e = 10$, $T_e = 111.111K$, $R = 1000$, adiabatic wall. A temporal analysis of all of the eigenvalues of the discretized system (using 31 collocation points) for $\alpha = (0.12, 0)$, $\beta = (0, 0)$ yields:

$$\omega = (0.1158601206, 1.367658245E - 04) \quad (3.184)$$

Malik reports $\omega = (0.1158647, 1.529E - 04)$ using his 4CD scheme and $\omega = (0.1158519, 1.357E - 04)$ using his MDSP method. However, Esfahanian (1991), who also used the same rectilinear coordinates for his stability analysis with a spectral collocation method and 101 points, reports a value:

$$\omega = (0.115861436, 1.37657E - 04) \quad (3.185)$$

which agrees much better with our results as well as with Malik's MDSP calculation.

Having obtained ω , a spatial eigenvalue calculation yields:

$$\omega = (0.1158, 0), \alpha = (0.11994036, -1.3877400E - 04) \quad (3.186)$$

along with the corresponding eigenvector. The PSE code PSX reproduces this result when marched in a parallel mode with this as the initial condition. A comparison¹ of the derivative of the linear operator used in the local analysis with respect to α and the coefficient of the derivative of the shape function with respect to x in the PSX code also yields complete agreement. (The analytical derivative used in the local analysis also agrees very well with second order accurate finite differences.)

Results for Malik's test case #3 for a three-dimensional disturbance have also been obtained. This test case is for an adiabatic wall with a boundary layer edge Mach number $M_e = 2.5$. The edge temperature is $T_e = 148.148148K$. The Reynolds number is $R = 3000$. Again, 31 collocation points were used. A temporal analysis for the entire spectrum of the discretized system for $\alpha = (0.06, 0)$, $\beta = (0, 10, 0)$ yields as one of the eigenvalues:

$$\omega = (3.673723764E - 02, 5.895818712E - 04) \quad (3.187)$$

Malik reports $\omega = (3.67340E - 02, 5.840E - 04)$. LSH gives as the corresponding spatial mode for $\omega = (3.67E - 02, 0)$, $\beta = (0.10, 0)$:

$$\alpha = (5.9977439E - 02, -8.0711300E - 04) \quad (3.188)$$

¹using the UNIX *diff* command

Marching with the PSE code in a parallel flow mode using the spatial eigenvalue and eigenvector as initial conditions reproduces the same result. Also, the coefficients of the derivatives of the local linear operator with respect to α and β in LSH again agree very well with the derivatives of the shape function with respect to x and z , respectively, in the PSE code (as well as finite difference calculations).

Our final test case is a comparison with the local stability results produced by an independently developed fourth order accurate compact finite difference code written at DynaFlow. This code uses the Euler-MacLaurin finite difference formula (e.g., Malik 1990).

The conditions are the same as those studied by El-Hady (1980) and Bertolotti (1991). The boundary layer edge Mach number is $M_e = 1.6$. The edge temperature is $T_e = 206K$, and the Reynolds number is $R = 400$.

When $\omega = (0.016, 0)$, $\beta = (0, 0)$, and the outer computational domain is taken to be $\eta_{max} = 100$, the compact finite difference code yields:

$$\alpha = (3.509E - 02, 8.63E - 04) \quad (3.189)$$

When $\eta_{max} = 200$, it yields:

$$\alpha = (3.5E - 02, 8.76E - 04) \quad (3.190)$$

Using 51 collocation points to compute the same spatial eigenvalue, LSH gives

$$\alpha = (3.5187357E - 02, 8.7718022E - 04) \quad (3.191)$$

The accuracy of the spatial growth rate substantially deteriorates if only 31 collocation points are used. This case is considered further in the following section.

Conservative Variables¹

The last test case described above has also been used to check the correctness of the insert files when the conservative variables are used. Again, this is a Mach 1.6 boundary layer edge flow with an edge temperature of 206K. $\omega = (0.016, 0)$ and $\beta = (0, 0)$. Since the discretization error is different than for the primitive variables, the grid can be consecutively refined and the results compared to see whether they approach one another:

no. pts.	$\alpha = (\alpha_r, \alpha_i)$	
	primitive	conservative
51	(3.5187357E-02, 8.7718022E-04)	(3.5187377E-02, 8.7707594E-04)
81	(3.5190580E-02, 8.7671680E-04)	(3.5190577E-02, 8.7673937E-04)
101	(3.5190440E-02, 8.7695450E-04)	(3.5190431E-02, 8.7696982E-04)
121	(3.5190019E-02, 8.7687392E-04)	(3.5190015E-02, 8.7687837E-04)

The results seem to be converging, albeit slower than one might expect. We conclude that the equations insert files pass this test.

¹One must carefully specify the boundary conditions in the Definitions file in this case. Here, the first disturbance variable must be zero at the wall. Also, there is no boundary condition on the second disturbance variable (ρ).

Quasi-Parallel Flow, Rectilinear Coordinates

Primitive Variables

Continuing with the same test case described above, the quasi-parallel flow approximation yields:

$$\alpha = (3.4436138E - 02, 1.0105549E - 03) \quad (3.192)$$

using 121 collocation points.

Conservative Variables

Again, for the same boundary layer (adiabatic wall, $M_e = 1.6$, $T_e = 206K$), the quasi-parallel flow approximation yields:

$$\alpha = (3.4660556E - 02, 1.1219040E - 03) \quad (3.193)$$

using the conservative variables with $\omega = (0.016, 0)$, $\beta = (0, 0)$ and 121 collocation points. This obviously is in slight disagreement with (3.192). This is precisely because the basic state depends on x . In particular, the transformation between the primitive and conservative variables depends upon u and ρ , which in turn depend upon x for any fixed value of y . Hence, it is not possible for both sets of variables to be normal modes, yet this is what is assumed by the local analysis. The disturbance equations are, thus, slightly different, leading to slightly different results. Additional support for this can be found in the following subsection.

Quasi-Parallel Flow, Similarity Coordinates

Primitive Variables

Again, continuing with the adiabatic wall Mach 1.6 boundary layer (with edge temperature $T_e = 206K$), one obtains

$$\alpha = (3.4967897E - 02, 9.0065327E - 04) \quad (3.194)$$

for the two-dimensional disturbance $\omega = (0.016, 0)$, $\beta = (0, 0)$ using 51 collocation points, and

$$\alpha = (3.4969567E - 02, 8.9995719E - 04) \quad (3.195)$$

using 121 collocation points. This last result should be compared to that obtained using the conservative variables.

Conservative Variables

For the same test case, using the conservative variables and 121 collocation points gives:

$$\alpha = (3.4967547E - 02, 8.9993425E - 04) \quad (3.196)$$

This is virtually the same as (3.195). This can be explained as follows. In the similarity coordinates, u and ρ depend upon η only. The normal velocity component (which is very small) does, however, depend weakly upon x . Hence, the transformation between the primitive and conservative variables is (almost) independent of x . This, in turn, means that the variables should have (virtually) the same spectrum.

Scaled Conservative Variables

Continuing with the same test case, but using 51 collocation points for greater efficiency, one obtains

$$\alpha = (3.4966572E - 02, -1.5638850E - 04) \quad (3.197)$$

using the scaled conservative variables. This is approximately what one should expect because, from (3.47),

$$\frac{\partial}{\partial \xi} (\ln \sqrt{g}) = \frac{1}{2x} = \frac{1}{800} = 1.25E - 03 \quad (3.198)$$

Hence,

$$\frac{\partial \tilde{\rho}}{\partial \xi} = \frac{\partial}{\partial \xi} \left\{ \ln \left(\frac{\sqrt{g} \rho}{\sqrt{g}} \right) \right\} \quad (3.199)$$

$$= \frac{\partial}{\partial \xi} \{ \ln \sqrt{g} \tilde{\rho} - \ln \sqrt{g} \} \quad (3.200)$$

$$= i\alpha + \frac{i^2}{2x} \quad (3.201)$$

$$= i \left(\alpha + \frac{i}{2x} \right) \quad (3.202)$$

$$= (3.4966572E - 02, 1.09361150E - 03) \quad (3.203)$$

This compares better with (3.194).

Again, the spatial eigenvalue (3.197) can be reproduced by the PSE code by marching in a parallel mode starting with the correct eigenvalue and eigenvector. Also, the UNIX debugger has been used to check that the coefficients of the disturbance quantities in the conservation of mass equation are correct when the scaled disturbance variables are used. This is a significant (although not comprehensive) check because of the many intermediate algebraic manipulations that the code performs to achieve the final (in this case, simple) result.

3.2.5 Linear PSE

The same flat plate boundary layer considered in the previous sections was also analyzed with the linear PSE. Again, this is a Mach 1.6 boundary layer edge flow with an edge temperature of 206K, $\omega = (0.016, 0)$ and $\beta = (0, 0)$. The results obtained with a step size $\Delta \xi = 30$ are shown in Figure 3.1. Similar results are obtained when a step size of 20 is used, but with a step size of 10 the computed growth rate begins to oscillate in the streamwise direction due to the pressure gradient $\partial p / \partial \xi$.

The linear PSE integration used approximate initial conditions obtained from a quasi-parallel local analysis in similarity coordinates. Figure 3.1 compares these results with those obtained from another program which uses the compact Euler-MacLaurin finite difference formula (i.e., Malik, [1990]) to solve the PSE specifically for the flat plate compressible boundary layer. The transients for the two PSE calculations are different because the initial conditions were different: the compact finite

difference program used initial conditions generated from a local quasi-parallel analysis in Cartesian coordinates. The amplitudes shown were, thus, scaled so that the last data point computed by the compact scheme agreed with the spectral calculation. This makes it clearer that the differences are due to the transients.

3.2.6 Nonlinear PSE

Finally, the nonlinear PSE were used to predict the spatial evolution of a subharmonic disturbance in a laminar flow modulated by a two-dimensional primary instability. The boundary conditions are the same as those of El-Hady (1991), with whom we compare our results. The edge temperature is $300K$, the Sutherland viscosity law is used, the Prandtl number is 0.70, and the edge Mach number varies from 0 to 1.2.¹ In each case, the mean flow distortion and harmonics created by the primary wave are neglected. The primary wave itself is assumed to grow linearly.

The results for an edge Mach number = 1.2 are shown in Figures 3.2 and 3.3. The frequency of the primary disturbance is $F = 10^6\omega/R$ is 60 and the spanwise wavenumber of the subharmonic is $b = 10^3\beta/R$ is 0.15. R is the square root of the x Reynolds number.

Two different PSE results are shown in Figures 3.2 and 3.3. The solid lines illustrate the results obtained when Cartesian coordinates are used, and the dashed lines show the results obtained when similarity coordinates are used. The \times and $*$ symbols represent El-Hady's results.

Figure 3.2 compares the spatial growth rate predictions at the local maximum in the rms profiles. One can see that, apart from some initial transients, the results using Cartesian and similarity coordinates agree very well. This is an important test because the Cartesian coordinates are orthogonal whereas the similarity coordinates are not. The agreement with El-Hady's results is not as good, however. This is commented on in further detail later.

Figure 3.3 compares the values of $\Im(\partial\theta/\partial\xi^1) = \alpha$, predicted by the PSE in Cartesian and similarity coordinates to El-Hady's results. Since $-\alpha$ is really the growth rate of the *norm* of the variable which is used to partition the ξ^1 dependence,² and all of the disturbances vanish in the far-field, it can be shown that the norm should be the same regardless of whether Cartesian or similarity coordinates are used. While the agreement between the Cartesian and similarity results in Figure 3.3 is not as good as the local results shown in Figure 3.2, it still appears reasonable given the size of the transients.

Some of the discrepancies between the PSE results and El-Hady's results may be due to the following. While the PSE calculations neglect the ξ^1 derivatives and the normal velocity component of the basic state to better simulate El-Hady's theoretical results, they retain the ξ^1 derivatives of the mode shape functions. This introduces a nonlocal effect which is not present in El-Hady's results. In fact, El-Hady's analysis assumes that the basic flow modulated by the primary disturbance is locally a periodic function of time τ and distance ξ^1 . Hence, it neglects the spatial growth rate of the

¹El-Hady also investigated some other edge Mach numbers.

²here taken to be u^1

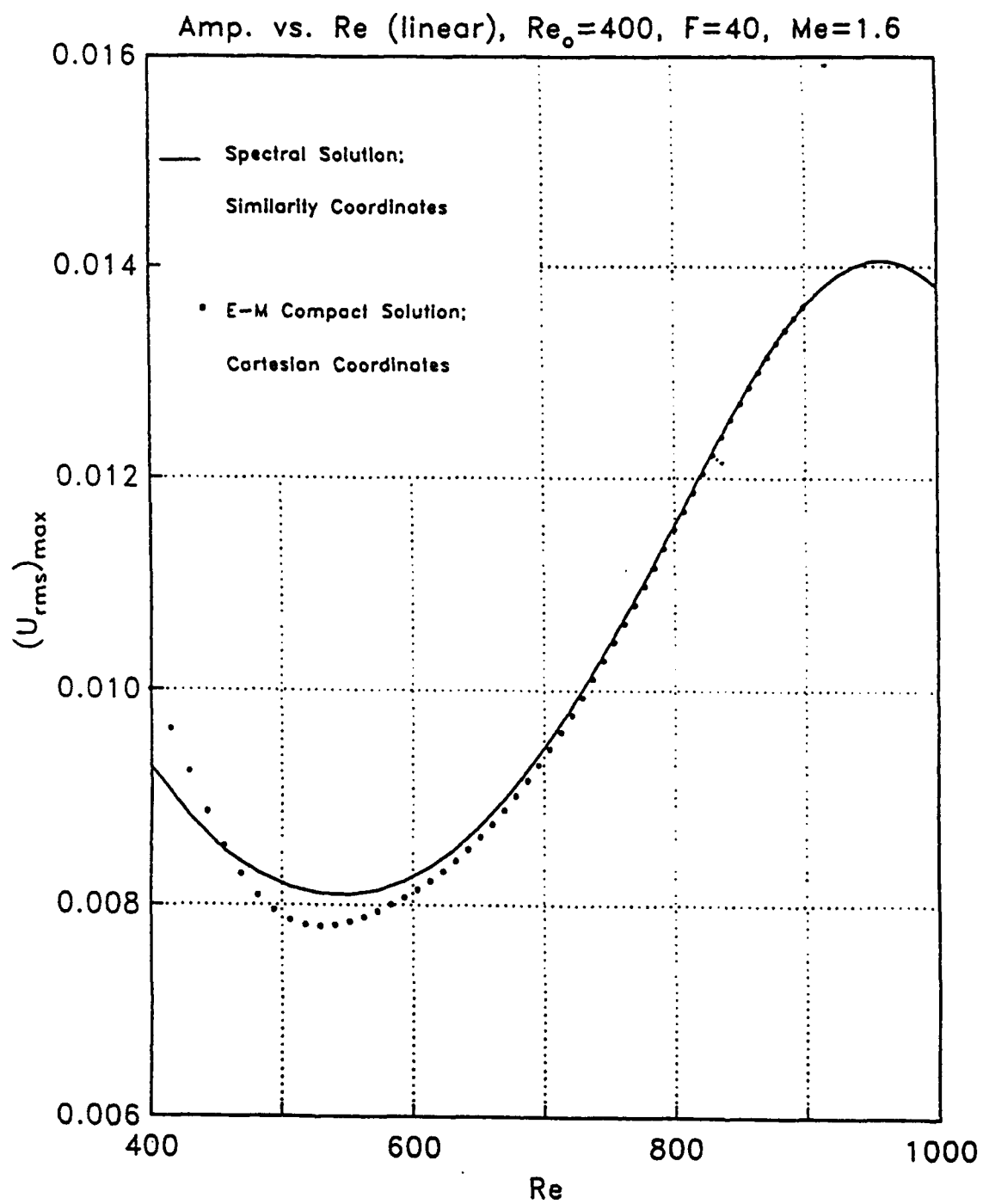


Figure 3.1: Root Mean Square of Disturbance Tangential Velocity Component as a Function of the Local Reynolds Number

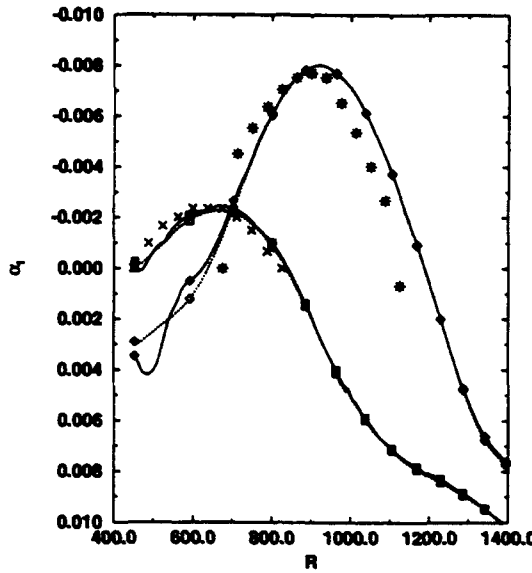


Figure 3.2: Spatial Growth Rate at Maximum in rms Profiles. Amplitude of primary disturbance at neutral point = 0.1%. Frequency $F = 60$, spanwise wavenumber $b = 0.15$. \square : PSE primary mode (2,0), \diamond : PSE subharmonic mode (1,1). Solid line: Cartesian coordinates. Dashed line: similarity coordinates. \times : El-Hady (1991) primary mode (2,0), $*$: El-Hady (1991) subharmonic mode (1,1).

primary disturbance. The PSE calculations, however, include the spatial growth rate of the primary disturbance. The transport and thermodynamic properties are also different than what El-Hady used. El-Hady computed the viscosity from the Sutherland law. However, he determined the thermal conductivity not from the constant Prandtl number and specific heat but from $k^* = 0.6325 \times 10^{-5} \sqrt{T} / (1 + (245.4/T) \times 10^{-12})$, where k is measured in calories per centimeter per second per degrees Celsius and T is in Kelvin. He also used the National Bureau of Standards perfect-gas tables to specify the Prandtl number. He then computed the specific heat and enthalpy from the Prandtl number knowing the viscosity and thermal conductivity.

3.3 Summary

After having performed the following tests:

1. Manually cross-checked the calculation of the metric terms.
2. Computed some of the differential operators two different ways.
3. Compared with results available in the literature.
4. Compared with calculations of different software written at DynaFlow by different personnel.

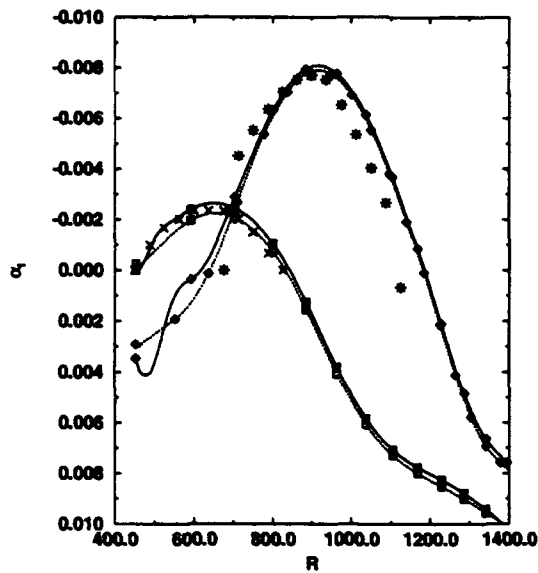


Figure 3.3: Spatial Growth Rate at Maximum in rms Profiles. Amplitude of primary disturbance at neutral point = 0.1%. Frequency $F = 60$, spanwise wavenumber $b = 0.15$. \square : PSE Primary mode (2,0), \diamond : PSE Subharmonic mode (1,1). Solid line: Cartesian coordinates. Dashed line: similarity coordinates. \times : El-Hady (1991) primary mode (2,0), $*$: El-Hady (1991) subharmonic mode (1,1).

5. Compared PSE results obtained in Cartesian (orthogonal) and similarity (non-orthogonal) coordinates.

the suite of local linear stability analysis and PSE software appears to be working as designed. This should help give more confidence in the following applications which have more relevance to hypersonic flight.

Chapter 4

Hypersonic Flow over a Sharp Cone at Angle of Attack

The stability of the Mach 8 flow past a sharp 7° half-angle cone at angle of attack has been studied experimentally by Stetson et al. (1985,1992). They measured the mass flux and total temperature fluctuations along the windward and leeward meridians at 2° angle of attack but only along the windward meridian at 4° angle of attack. The free-stream static temperature was approximately $95^\circ R$, and the surface temperature was allowed to reach equilibrium (adiabatic wall). Finally, the free-stream Reynolds number of the flow for the windward meridian measurements was 1 million per foot. However, they lowered the free-stream Reynolds number to 0.5 million per foot for their measurements along the leeward meridian to obtain a greater length of laminar flow.

The numerical analyses presented here simulate the conditions of their experiment at 2° angle of attack. However, the unit Reynolds number is 0.5 million per foot for both the windward and leeward meridians and, hence, different than the value for the windward meridian experiment. Since the unit Reynolds number has no bearing on the present *theoretical* results, this will not affect the comparison of the *dimensionless* results with the experimental data.

Only limited linear local and nonlocal numerical results were obtained because of the unexpected size of the nonparallel effects. These nonparallel effects are so large that we spent a good deal of time confirming them by performing a number of unique tests which are documented below. The tests reveal that the stability codes produce self-consistent results and that the nonparallel effects are indeed large.

4.1 Mean Flow Calculation

The mean flow was calculated using the AFWAL Parabolized Navier-Stokes (PNS) code. This code has been developed by a number of different workers since 1979 and has been documented by Kaul and Chaussee (1983); Stalnaker, Nicholson, Hanline, and McGraw (1986); and Rajendran (1989). It uses a space-marching technique and body-fitted coordinates to integrate the PNS equations downstream of data specified in an initial axial plane $x^1 = x_0^1$.

4.1.1 Coordinate System

The permissible body-fitted coordinates are all of the form:

$$x^1 = x^1(I) \quad (4.1)$$

$$x^2 = x^2(J, K) \quad (4.2)$$

$$x^3 = x^3(J, K) \quad (4.3)$$

where x^1 is the body axis. (See Figure 4.1.) This means that the solution is marched

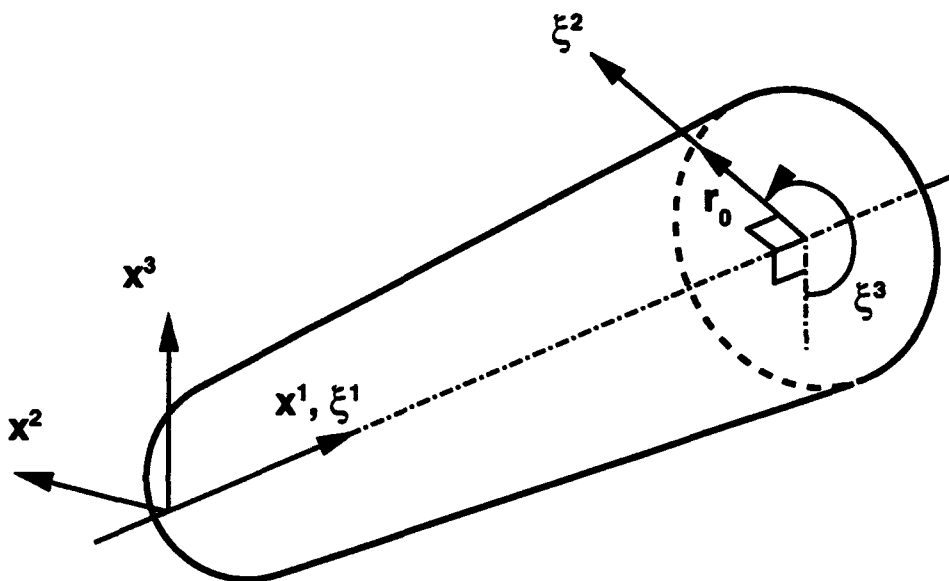


Figure 4.1: Coordinate System Used in the Stability Analyses.

in planes perpendicular to the body axis. Hence, the body-fitted coordinates are nonorthogonal whenever the slope of the body in the axial direction is nonzero. This is certainly the case for any cone of nonzero half-angle. We note this here because virtually the same coordinate system (Section 4.2) was used for the stability analyses in order to simplify the problem of interpolating the basic state solution onto the disturbance grid.

4.1.2 Initial Conditions

Two methods, each applicable to a different type of geometry, can be used to generate initial data for the PNS equations. One of these is the “step-back” procedure of Schiff and Steger (1979). Another is the solution of the governing equations in the forebody region.

The “step-back” procedure of Schiff and Steger (1979) has been implemented in the AFWAL PNS code. It can be used for pointed forebodies which have an almost conical flowfield about them. In this case, a conical coordinate system is chosen which includes the initial plane and a guess is made for the initial data. A step is

then taken in the marching direction to obtain the solution immediately downstream. Approximating the solution as locally conical, the solution in the downstream plane should be the same as that in the initial plane along the same conical rays. Hence, the initial plane of data is overwritten with the solution downstream along the same conical rays. This yields a new guess for the initial data which, upon stepping back to the initial station, can be used to begin the integration anew. Repeating this process until the gradients of the solution vanish along the conical rays to some prescribed level gives the locally conical flow. This is how the initial data were generated for the sharp cone studies presented here.

For blunt bodies, a different solution methodology must be used because the governing equations in the nose-tip region are elliptic. A thin-layer Navier-Stokes (TLNS) code developed by Rizk, Scott, and Newman (1983) can and has been used for this purpose. In particular, their code was used to generate the starting data for the blunt cone PNS solution used in Section 5. However, this TLNS code uses a variation of spherical coordinates while the AFWAL PNS code uses a variation of cylindrical coordinates. Multidimensional interpolation must, thus, be done to transfer the data from the TLNS grid to the AFWAL PNS initial plane. Routines supplied with the AFWAL PNS code were used for this purpose.

4.1.3 Basic State Results

In all the PNS calculations, the equations were first transformed to cylindrical coordinates and then to computational coordinates I, J, K . In the computational coordinates, the cone surface and bow shock appear as the surfaces $K = 1$ and $K = KMAX$, respectively. The 251 points were used in the radial direction, K , and 19 points in the circumferential direction, J . The equations were then discretized and solved with the Beam-Warming algorithm in conjunction with the Vigneron technique to suppress the “departure solutions.” The gas was assumed perfect and the cone adiabatic. Finally, PLOT3D FORTRAN unformatted planes files (Walatka, et al., 1990) were created and used to inspect the computed solution. These PLOT3D files were then input to the stability codes for the stability analyses.

Some of the basic state windward profiles and their first and second derivatives with respect to ξ^2 are shown in Figures 4.2 through 4.4.

The length scale for ξ^2 is $\sqrt{Re_L}$, where Re_L is the Reynolds number based on the free-stream shock conditions and length $L = 40"$ of the cone. The scales for the dependent variables are all taken to be the corresponding free-stream values. The bow shock is at $\xi^2 = 26.7$ in each figure, very near the last plotted point.

The profiles have been obtained from the PNS data by interpolating them with fifth order polynomials in ξ^1 , ξ^2 , and ξ^3 . Most of the data are reasonably smooth, but the same anomalies seen in the blunt cone ξ^1 contravariant velocity profiles near the wall (Figure 4.3 b) are also seen here.

The leeward interpolated profiles at $R = 712$ are shown in Figures 4.5 through 4.7.

The bow shock is at $\xi^2 = 37.44$ at this station, much further from the body than it is on the windward meridian.

Note that the boundary layer is approximately twice as thick on the leeward meridian as it is at the same station on the windward meridian. This is because the boundary layer is compressed much more on the windward side by the higher pressure behind the stronger bow shock created by the greater local deflection of the flow. In addition to the boundary layer being thicker on the leeward side, the corresponding basic state derivatives are also, in general, smaller. Finally, the computed derivatives appear to have some small numerical oscillations in them in the lower half of the boundary layer. However, no effort was made to improve upon these results by rerunning the AFWAL PNS code as our experience with the blunt body calculation indicated that this was very difficult to do.

4.2 Disturbance Coordinate System

The disturbance coordinate system is *nonorthogonal* and almost identical to the algebraic one that the AFWAL PNS code uses. It is given by:

$$\begin{aligned} x^1 &= \xi^1 \\ x^2 &= R \sin(\xi^3 - \pi) = -R \sin(\xi^3) \\ x^3 &= R \cos(\xi^3 - \pi) = -R \cos(\xi^3) \\ R &= r_b(\xi^1, \xi^3) + \xi^2 \end{aligned} \quad (4.4)$$

where ξ^1 is the distance measured along the body axis, ξ^3 is the circumferential angle measured in radians from the windward meridian in the $-\xi^1$ direction, r_b is the local body radius, and ξ^2 is the radial distance from the body surface. See Figure 4.1. The similarity between the AFWAL PNS algebraic grid and the coordinate system used for the stability analysis is intentional and enables the basic state to be interpolated with greater ease and accuracy.

4.3 Local Linear Stability Analyses

As mentioned earlier, the nonparallel effects for the sharp cone at angle of attack are so large (see Section 4.4) that we performed a number of tests to check the consistency of the results. Virtually all of these tests were conducted for the flow along the windward meridian.

4.3.1 Windward Meridian

One consistency check we performed was that the computed eigenvalue should be the same regardless of whether the velocity components or the mass fluxes are used as dependent variables in the disturbance equations *as long as all of the derivatives of the basic state flow with respect to ξ^1 and ξ^3 are neglected*.¹ When these derivatives are neglected, the density is approximated as being independent of ξ^1 and ξ^3 and so the transformation matrix between the different dependent variables is independent of

¹and as long as the truncation errors in the solution of the disturbance equations are negligible.

ξ^1 and ξ^3 . In this case, the assumption of normal modes for the velocity components is equivalent to the assumption of normal modes for the mass fluxes. However, if the transformation matrix is a function of any independent variable in which the stability equations are assumed to be separable, the normal mode approximation for the pre- and post-transformed dependent variables is *different*.¹ In this case an inconsistency appears in the equations which cannot be avoided.

That the eigenvalues are the same when the ξ^1 and ξ^3 derivatives of the basic state flow are *neglected* has been confirmed. Some supporting results are shown in Figure 4.8. Figure 4.8 shows the local spatial growth rate variation of a 70kHz second mode versus the local Reynolds number based on $x^1/\sqrt{Re_x}$. Although there appear to be only three curves in Figure 4.8, there are in fact four. Two of the curves are virtually coincident. The coincident curves are the results obtained from the described test.

While the results shown agree, this test revealed that the interpolation must be done very carefully. When the basic state ξ^2 derivatives were determined by differentiating the interpolating polynomials, the eigenvalues agreed. Other interpolation schemes that used central-differenced derivatives at the basic state grid points and more compact higher order interpolants gave eigenvalues differing by about 10%.

When the ξ^1 and ξ^3 derivatives of the basic state are *included*, they lead to quasi-parallel terms in the equations which are different in each dependent variable formulation. The computed solutions are then different. The two quasi-parallel solutions obtained from these different formulations are also shown in Figure 4.8. The discrepancy in the quasi-parallel results is, thus, some indication of the inaccuracy of the parallel flow approximation.

Finally, although all of the results shown in Figure 4.8 vary smoothly with R , they may not if the interpolation is not of high enough order. The results shown in Figure 4.8 were all obtained by interpolating the basic state solution with fifth order Lagrange polynomials in ξ^1 , ξ^2 , and ξ^3 . However, if the order of the Lagrange interpolants in ξ^1 and ξ^3 is lowered to 1 (linear), some of the results are not as accurate. Refer to Figure 4.9.

Figure 4.9 shows the results obtained when the derivatives of the basic state with respect to ξ^1 and ξ^3 are neglected. Here, the order of the ξ^1 and ξ^3 interpolating polynomials does not seem to have much of an effect on the accuracy. However, when the derivatives of the basic state with respect to ξ^1 and ξ^3 are included (Figure 4.10), the higher order interpolants are needed to obtain accurate results. This is especially true if the order of the Lagrange interpolant in ξ^2 is reduced to 3 from 5. See Figure 4.11. The higher order accuracy is necessitated by the large effect that the ξ^1 derivatives of the basic state have on the stability analysis and which, thus, must be computed accurately. This requirement also took some time to identify.

The tests described above indicate that self-consistent results may be obtained with the local stability code as long as consistent approximations are made. This

¹Another example is: the normal mode approximation for the Cartesian velocity components is not the same as the normal mode approximation for the curvilinear velocity components because the direction and magnitude of the basis vectors of the curvilinear coordinate system are in general functions of position.

holds true not only for the formulation of the problem via the selection of a set of dependent variables, but also for the basic state interpolation scheme. That the results agree in the final analysis helps validate our work.

Similar validation tests of the PSE software were also performed and are presented in Section 4.4. Before proceeding to them, however, we present the local linear results we obtained on the leeward side of the cone.

4.3.2 Leeward Meridian

More limited results were obtained on the leeward side as the contract period was ending. Figure 4.12 shows the spatial growth rates obtained from different local analyses. Two of the local analyses include curvature but exclude the derivatives of the basic state with respect to ξ^1 and ξ^3 . They use different dependent variables, though. The remaining two analyses include the basic state derivatives in a quasi-parallel manner.

As expected, the results obtained are the same regardless of which dependent variables are used as long as the basic state derivatives with respect to ξ^1 and ξ^3 are neglected. However, the results are very different when these derivatives are included in a quasi-parallel manner. Moreover, although not shown, the predicted values of the real part of α , also differ much more than usual (about 5%). These large differences make it difficult to determine whether the results all correspond to the same family of disturbances. Preliminary results seem to indicate that there may be other neighboring families of disturbances.

4.4 Linear PSE Analyses

As mentioned earlier, the nonparallel effects that we have found are unusually large in the flows along the windward and leeward meridians. Similar testing of the windward meridian results with different sets of dependent variables was done to confirm that these nonparallel effects are real. In each test, the partition (2.47) between the shape function and exponential variation was applied to the same variable: the disturbance density.

4.4.1 Windward Meridian

As with the local stability analyses, we checked our results using two different sets of variables: ρ , T , and the physical contravariant *velocity components*; and ρ , p , and the physical contravariant *mass fluxes*. However, no longer is the disturbance assumed to depend solely on the local properties of the flow profiles. The modulations of the mode amplitude and phase due to the nonparallel basic flow are now taken into account.

If the basic state derivatives with respect to ξ^1 and ξ^3 are *neglected* while the true (nonparallel) profiles are used in integrating the disturbance downstream, the results shown as dotted lines in Figure 4.13 are obtained. Although the results obtained using different dependent variables are *initially* the same as discussed in Section 4.3,

they diverge downstream. Note that this would not be the case if the basic state flow were actually parallel for then both results would be equivalent to the local stability results which are identical. Hence, it appears that the derivatives of the basic state with respect to ξ^1 and ξ^3 are, in fact, not necessarily negligible.

If the profiles are allowed to vary and the *first* derivatives of the basic state with respect to ξ^1 and ξ^3 are *retained* in the equations, then the differences vanish. This is shown by the agreement of the two solid lines in Figure 4.13 further downstream. These lines initially disagree because they both began with the results of a quasi-parallel local analysis. The local quasi-parallel analyses, as discussed in Section 4.3 yield inconsistent results. Given these different transients, the agreement between the two PSE results is some indication that the PSE approximation is valid for this disturbance. In other words, the viscous terms in the stability equations which involve the *second* derivatives of the shape function with respect to ξ^1 and/or ξ^3 are indeed negligible.

Finally, the growth rate predicted by the PSE analyses which included the ξ^1 and ξ^3 derivatives of the basic state are compared directly in Figure 4.14 to the local analyses which neglected the same terms. The large nonparallel effects are clearly evident.

4.4.2 Leeward Meridian

Finally, some linear PSE results are shown for the 30 kHz disturbance along the leeward ray that was investigated earlier with the local analyses. The nonparallel flow effects seem even larger here than they did along the windward ray. These effects are shown in Figure 4.15. Figure 4.15 compares the results from the linear PSE analysis which included the ξ^1 and ξ^3 derivatives of the basic state to the local linear results which neglected the same derivatives. (The linear PSE analysis used the physical velocity components). The linear PSE and local analyses are clearly very different.

4.5 Summary

Extensive stability results including calculations along lines other than the windward and leeward meridians could not be obtained within the contract period. Nevertheless, our calculations support the contention of Stetson, et al (1992) that the wavelength and period of the second mode scale approximately with the boundary layer thickness for the same edge velocity. At angle of attack, the windward boundary layer is much thinner (compressed greater) and the leeward boundary layer is much thicker (compressed less). Hence, the wavelength of the most unstable second mode in the windward boundary layer is much shorter and the frequency much higher than at zero angle of attack. Conversely, the wavelength of the most unstable mode in the leeward boundary layer is much longer and the frequency much lower than at zero angle of attack.

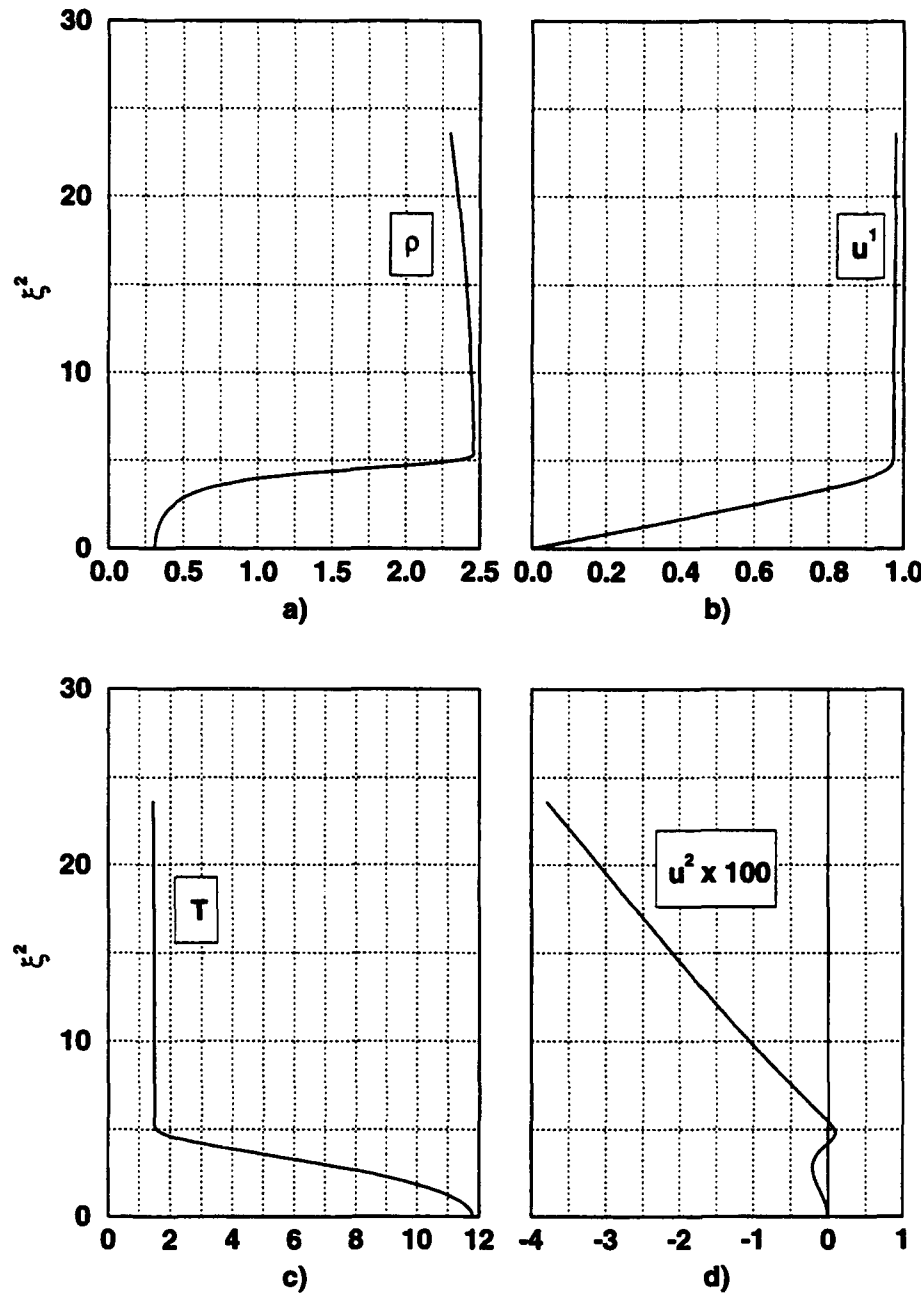


Figure 4.2: AFWAL PNS Basic State Profiles of the Flow Over a Sharp, 7° Half-Angle Cone at 2° Angle of Attack. Windward meridian, $R = 746$ (interpolated). Bow shock at $\xi^2 = 26.7$. a) Density. b) ξ^1 contravariant velocity component. c) Temperature. d) ξ^2 contravariant velocity component $\times 100$.

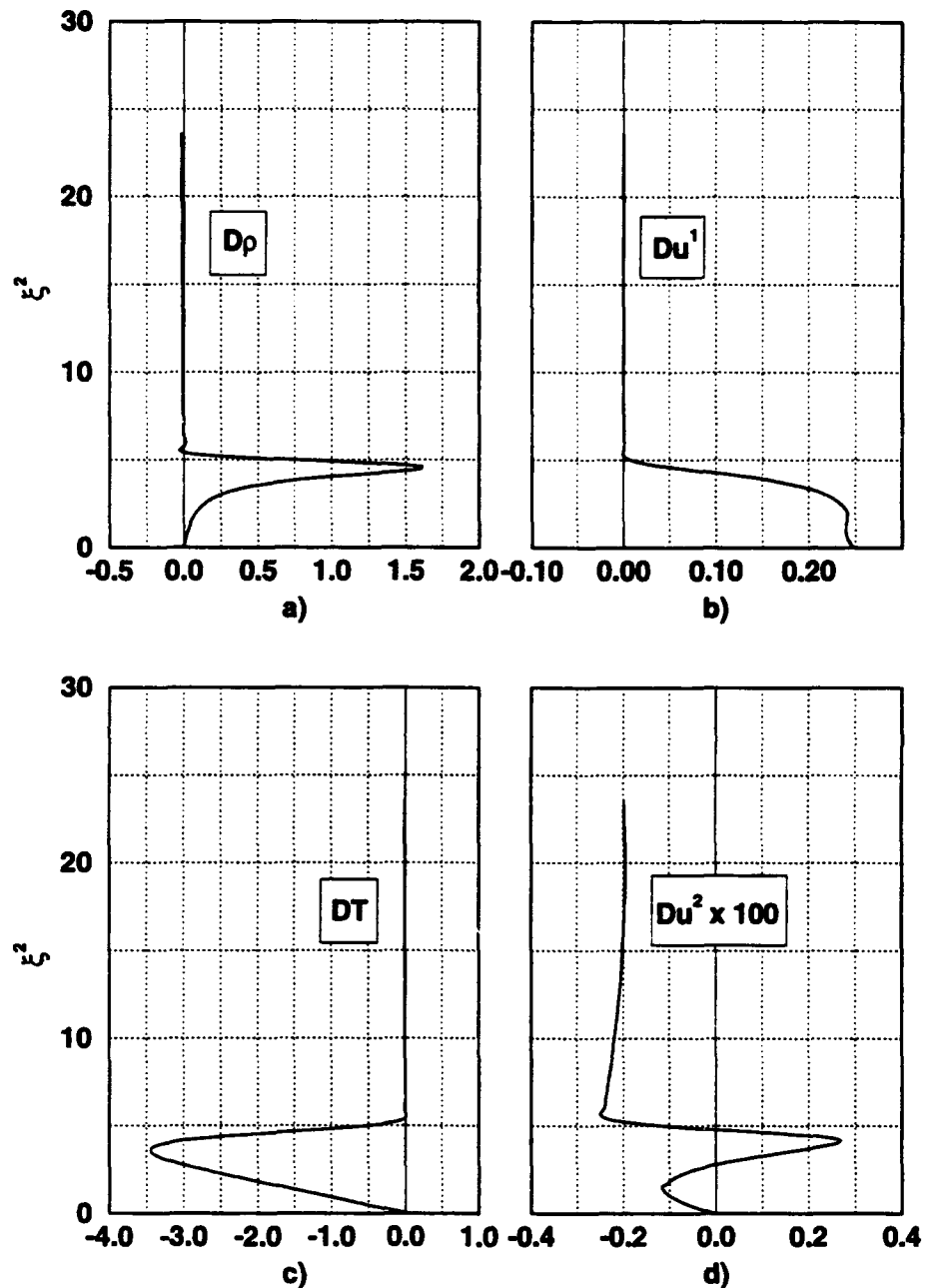


Figure 4.3: AFWAL PNS Basic State Profiles of the Flow Over a Sharp, 7° Half-Angle Cone at 2° Angle of Attack. First derivatives with respect to ξ^2 , windward meridian, $R = 746$ (interpolated). Bow shock at $\xi^2 = 26.7$. a) Density. b) ξ^1 contravariant velocity component. c) Temperature. d) ξ^2 contravariant velocity component x 100.

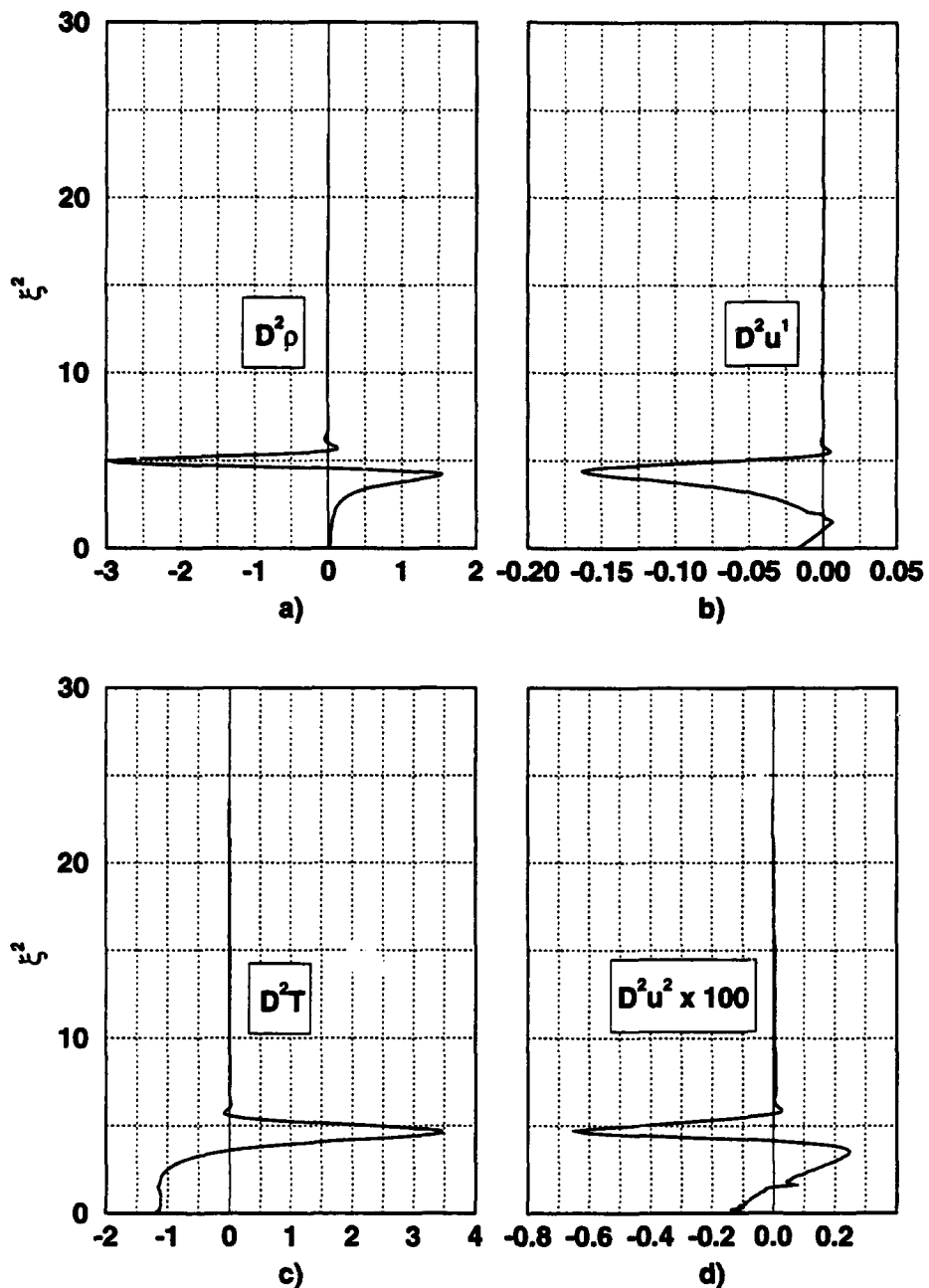


Figure 4.4: AFWAL PNS Basic State Profiles of the Flow Over a Sharp, 7° Half-Angle Cone at 2° Angle of Attack. Second derivatives with respect to ξ^2 , windward meridian, $R = 746$ (interpolated). Bow shock at $\xi^2 = 26.7$. a) Density. b) ξ^1 contravariant velocity component. c) Temperature. d) ξ^2 contravariant velocity component $\times 100$.

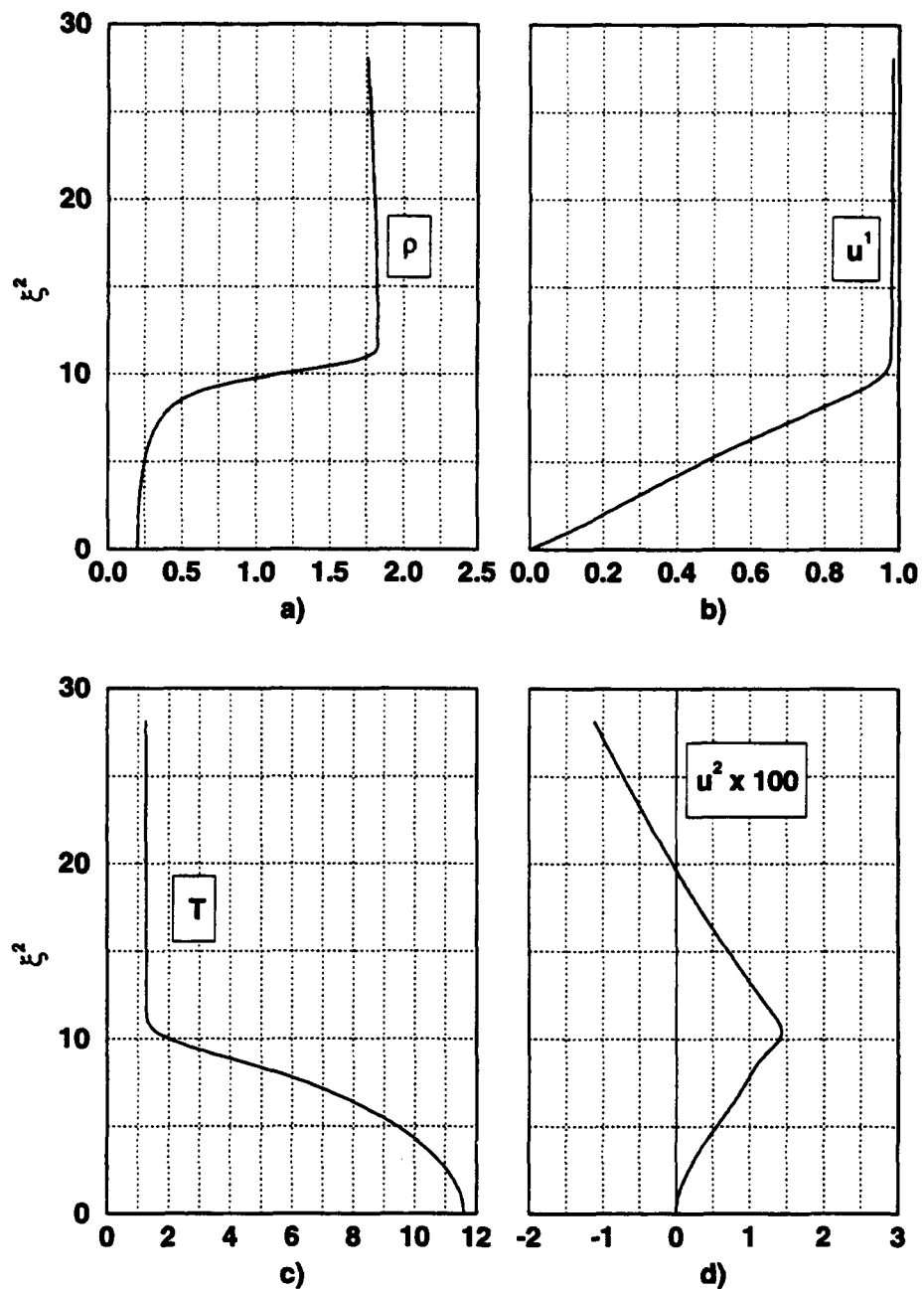


Figure 4.5: AFWAL PNS Basic State Profiles of the Flow Over a Sharp, 7° Half-Angle Cone at 2° Angle of Attack. Leeward meridian, $R = 712$ (interpolated). Bow shock at $\xi^2 = 37.44$. a) Density. b) ξ^1 contravariant velocity component. c) Temperature. d) ξ^2 contravariant velocity component $\times 100$.

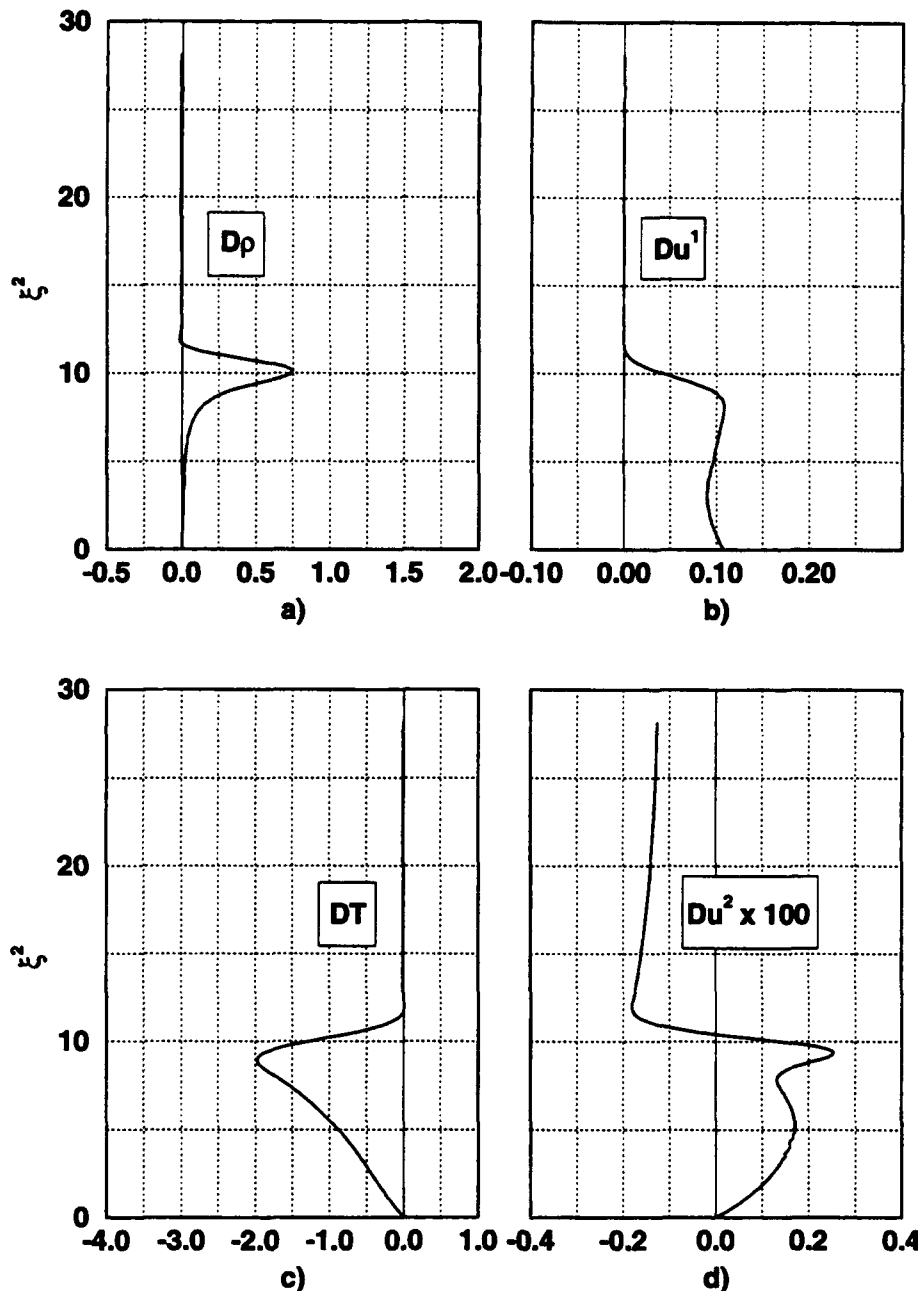


Figure 4.6: AFWAL PNS Basic State Profiles of the Flow Over a Sharp, 7° Half-Angle Cone at 2° Angle of Attack. First derivatives with respect to ξ^2 , leeward meridian, $R = 712$ (interpolated). Bow shock at $\xi^2 = 37.44$. a) Density. b) ξ^1 contravariant velocity component. c) Temperature. d) ξ^2 contravariant velocity component $\times 100$.

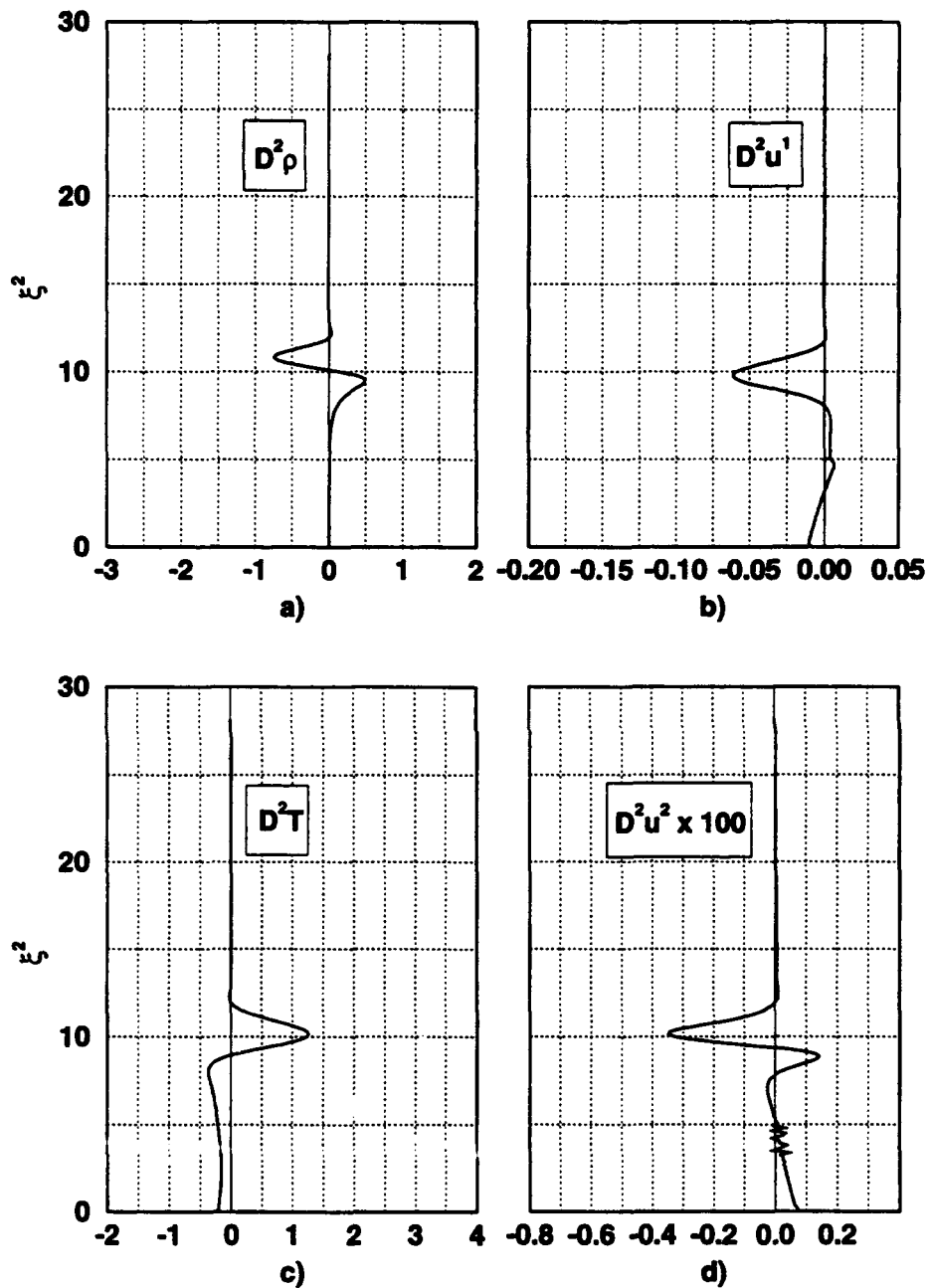


Figure 4.7: AFWAL PNS Basic State Profiles of the Flow Over a Sharp, 7° Half-Angle Cone at 2° Angle of Attack. Second derivatives with respect to ξ^2 , leeward meridian, $R = 712$ (interpolated). Bow shock at $\xi^2 = 37.44$. a) Density. b) ξ^1 contravariant velocity component. c) Temperature. d) ξ^2 contravariant velocity component $\times 100$.

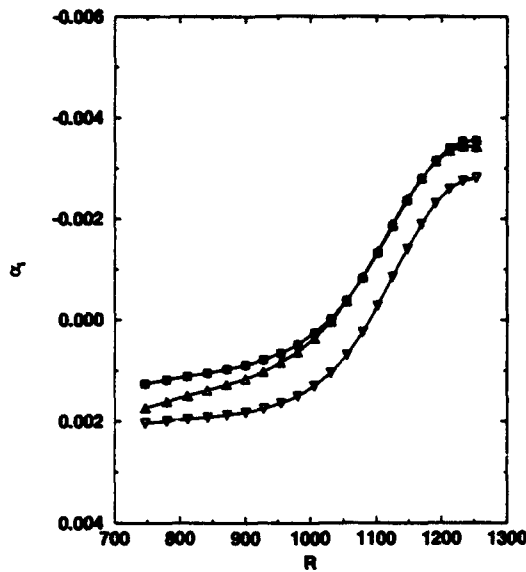


Figure 4.8: Comparison of Spatial Growth Rates of 70 kHz Disturbance Along Windward Meridian. $\beta = 0$, length scale = $x^1/\sqrt{Re_{x^1}}$. \square Physical velocity components (parallel), \diamond Physical mass fluxes (parallel), \triangle Physical velocity components (quasi-parallel), ∇ Physical mass fluxes (quasi-parallel).

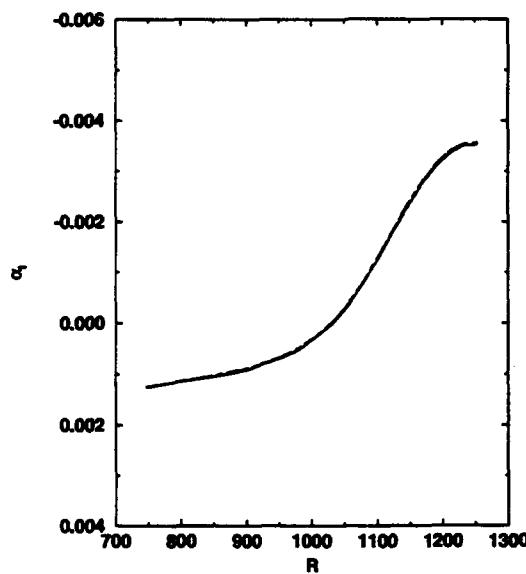


Figure 4.9: Comparison of Spatial Growth Rates of 70 kHz Disturbance Along Windward Meridian. Physical components, locally parallel flow, $\beta = 0$, length scale = $x^1/\sqrt{Re_{x^1}}$, fifth order interpolants in ξ^2 . Solid line: First order interpolants in ξ^1 and ξ^3 ; Dashed line: Third order interpolants in ξ^1 and ξ^3 ; Dot-dashed line: Fifth order interpolants in ξ^1 and ξ^3 .

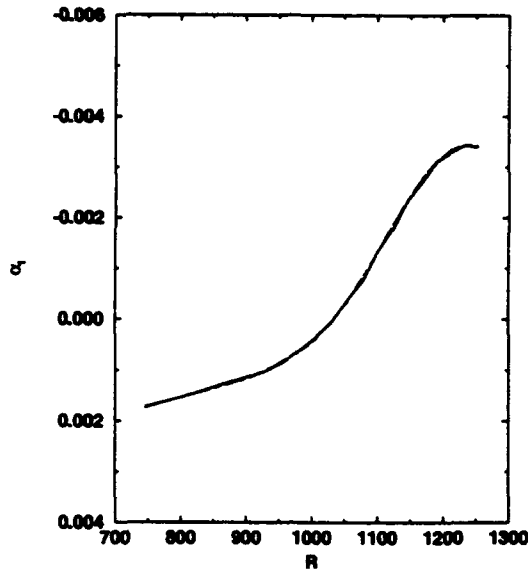


Figure 4.10: Comparison of Spatial Growth Rates of 70 kHz Disturbance Along Windward Meridian. Physical components, quasi-parallel flow, $\beta = 0$, length scale = $x^1/\sqrt{Re_{x^1}}$, fifth order interpolants in ξ^2 . \square) First order interpolants in ξ^1 and ξ^3 , \diamond) Third order interpolants in ξ^1 and ξ^3 , \triangle) Fifth order interpolants in ξ^1 and ξ^3 .

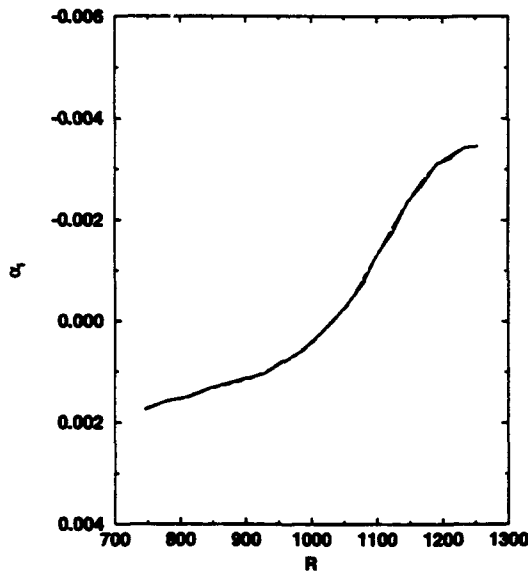


Figure 4.11: Comparison of Spatial Growth Rates of 70 kHz Disturbance Along Windward Meridian. Physical components, quasi-parallel flow, $\beta = 0$, length scale = $x^1/\sqrt{Re_{x^1}}$, fifth order interpolants in ξ^2 . Solid line: First order interpolants in ξ^1 and ξ^3 ; Dashed line: Third order interpolants in ξ^1 and ξ^3 ; Dot-dashed line: Fifth order interpolants in ξ^1 and ξ^3 .

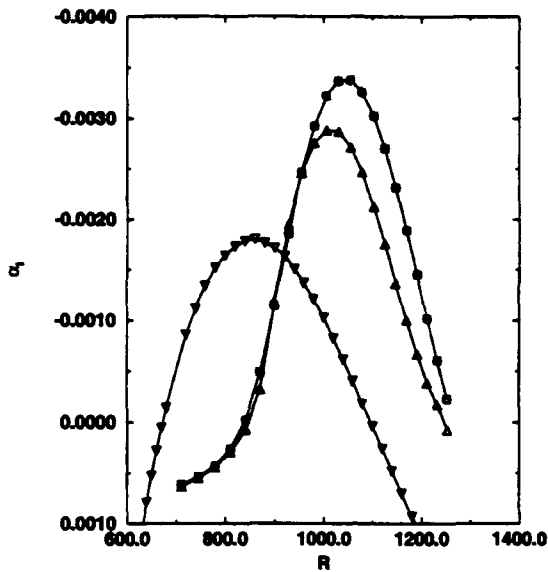


Figure 4.12: Comparison of Spatial Growth Rates of 30 kHz Disturbance Along Leeward Meridian. $\beta = 0$, length scale = $x^1/\sqrt{Re_{x^1}}$. \square Physical velocity components (parallel), \diamond Physical mass fluxes (parallel), \triangle Physical velocity components (quasi-parallel), ∇ Physical mass fluxes (quasi-parallel).

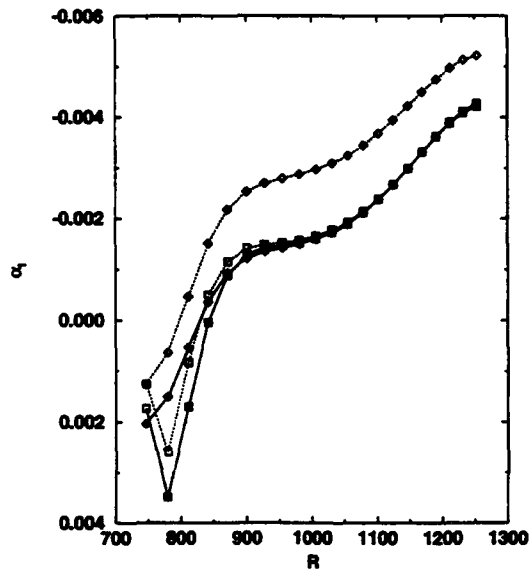


Figure 4.13: Comparison of Spatial Growth Rates of 70 kHz Disturbance Along Windward Meridian. $\beta = 0$, length scale = $x^1/\sqrt{Re_{x^1}}$. Dotted lines: locally parallel basic state. Solid lines: nonparallel basic state. \square) Physical velocity components, \diamond) Physical mass fluxes.

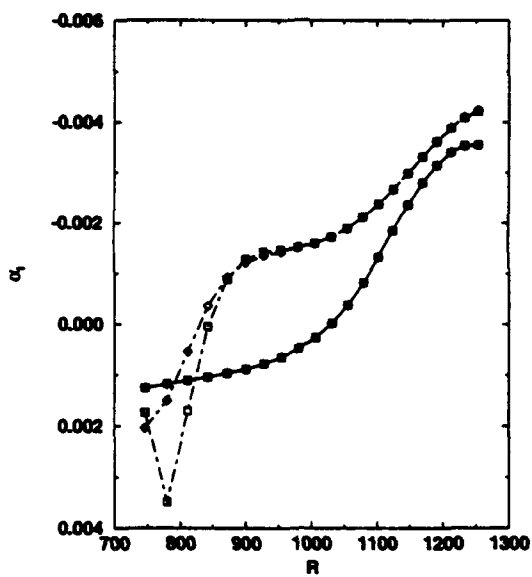


Figure 4.14: Comparison of Spatial Growth Rates of 70 kHz Disturbance Along Windward Meridian. $\beta = 0$, length scale = $x^1/\sqrt{Re_{x^1}}$. Solid lines: local analyses. Dot-dashed lines: linear PSE analyses. \square) Physical velocity components, \diamond) Physical mass fluxes.

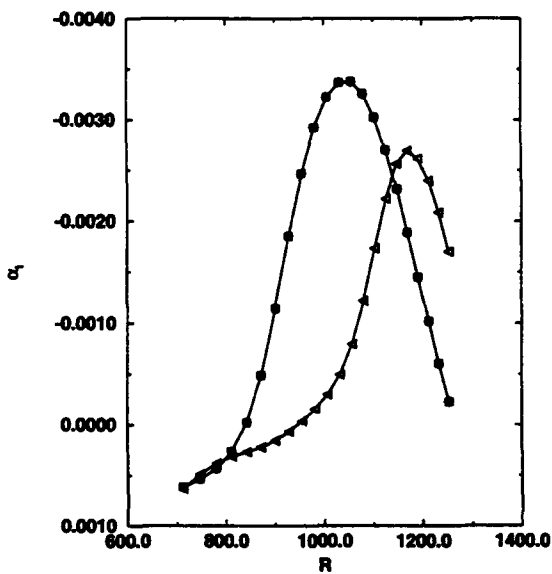


Figure 4.15: Comparison of Spatial Growth Rates of 30 kHz Disturbance Along Leeward Meridian. $\beta = 0$, length scale = $x^1/\sqrt{Re_{x^1}}$. \square) Physical velocity components, local, \diamond) Physical mass fluxes, local, \triangleleft) Physical velocity components, PSE.

Chapter 5

Hypersonic Flow over a Blunt Cone

Stetson et al. (1984)(STDS) has carried out stability experiments on flow over blunt cones at freestream Mach number of 8.0. The half angle of the cone θ_c is 7° . It is 40 inches long and 9.823 inches in base diameter. The effect of nose bluntness on stability was studied by using different nose radii (R_N) of 0.15, 0.25, 0.50, and 0.70 inches. The stability of the mean flow in one of the experiments, the flow over the blunt cone with a 0.15-inch nose tip, is analyzed in this section. In this experiment, freestream stagnation temperature is 1350 deg R , freestream temperature is 96 deg R (54.3 deg K), freestream velocity (calculated from freestream Mach number) is 1181.67 m/s and the unit Reynolds number is $2.5 \times 10^6/\text{ft}$. The physical interfaces and insert files for this problem are in the subdirectory *w.wpafb*.

5.1 Mean Flow Calculation

The basic flow has been calculated using two different codes: a Thin Layer Navier-Stokes (TLNS) code developed by Esfahanian (1991); and the AFWAL Parabolized Navier-Stokes (PNS) code.¹

Esfahanian's code solves the Thin Layer Navier Stokes (TLNS) equations using the second order accurate central difference algorithm of Beam and Warming (1978). It also uses a scheme to fit the bow shock as a discontinuity in the flow so that the rest of the shock layer can be computed accurately with no numerical oscillations and minimal artificial viscosity. Esfahanian (1991) has established grid convergence of the solution, and the results from his finest grid calculation (1300 by 200) are used here for the stability analysis. Some representative profiles are presented below.

The AFWAL PNS code is briefly discussed in Section 4.1. This code uses a bow-shock fitting scheme also, and has the option of using the Beam-Warming algorithm or the Roe flux-differenced upwind scheme (Rajendran, 1989) to solve the equations. Different runs were tried using each algorithm on different grids. One grid had 251 and the other 501 grid points in the radial direction. The grid with the greater number

¹see Section 4.1 for references.

of radial grid points required smaller and, hence, more marching steps because of the practical limit on the CFL number. At the same time, the PNS code implements some logic to enforce a minimum step size so that departure (exponentially divergent) solutions are avoided. This minimum step size requirement makes it impossible to arbitrarily refine the grid in the radial direction and, hence, more difficult to compute accurate solutions. Finally, only runs with the Beam-Warming algorithm completed successfully, and only with significant levels of implicit smoothing, explicit artificial viscosity, and implicit matrix conditioning. The runs with the Roe upwind scheme did not converge.

Figures 5.1, 5.2, and 5.3 compare the TLNS and PNS basic state profiles and their first two derivatives with respect to ξ^2 . Here, ξ^2 has the meaning assigned to it in each code respective coordinate system. See Figures 5.7 and 4.1. While the meaning of ξ^2 is different in each case - the TLNS body-intrinsic ξ^2 coordinate being normal to the body *surface* and the AFWAL ξ^2 coordinate being normal to the body *axis* - the error in comparing them this way is small because the cone angle is only 7° and the boundary layer is thin. Since $\cos(7^\circ) = 0.9925$ and $\sin(7^\circ) = 0.1219$, one has $\xi_{TLNS}^2 = 0.9925\xi_{PNS}^2$. This should have only a very minor effect on the comparison of the scalar quantities such as the density and temperature. However, the velocity components are also different. The velocity components shown for the TLNS solution are the physical components tangent and normal to the body surface, whereas those of the PNS solution are the ξ^1 and ξ^2 contravariant (axial and radial) velocity components. This difference also has some very minor effect on the comparison which the reader should be aware of.

Some errors in the AFWAL PNS solutions are clearly evident in the derivatives of the axial velocity component near the wall (Figures 5.2 b and 5.3 b). These errors are most likely caused by the high levels of matrix conditioning required, especially considering what the conditioning does to the Parabolized Navier-Stokes equations. Stalnaker, et al. (1986) (p. 110) show that the matrix conditioning effectively changes the eigenvalues of the inviscid flux vector Jacobians by a small amount ϵ in the subsonic region of the boundary layer. The high levels of artificial viscosity required may also contribute to the errors in the results.

Some of the differences between the two solutions may also be attributable to the transport properties used in the basic state calculations. Although the same transport properties were used in the *stability* analyses, we do not know what transport properties the AFWAL PNS code uses.

As will be seen later, all of these errors and differences together have a significant effect on the stability analysis. This is especially true since the largest errors or differences occur near the edge of the boundary layer, close to the critical layer of the disturbance.

Finally, some additional TLNS results are shown in Figure 5.4. Figure 5.4 compares the TLNS predicted temperature along the cone surface with measurements of STDS experiments. Discrepancies here are mainly due to two reasons. First, the adiabatic wall boundary condition is used in the calculations, while experimental conditions may not be 100 percent adiabatic. Secondly, the thermodynamic model used in the calculations (e.g., Sutherland's Law for viscosity) may not accurately repre-

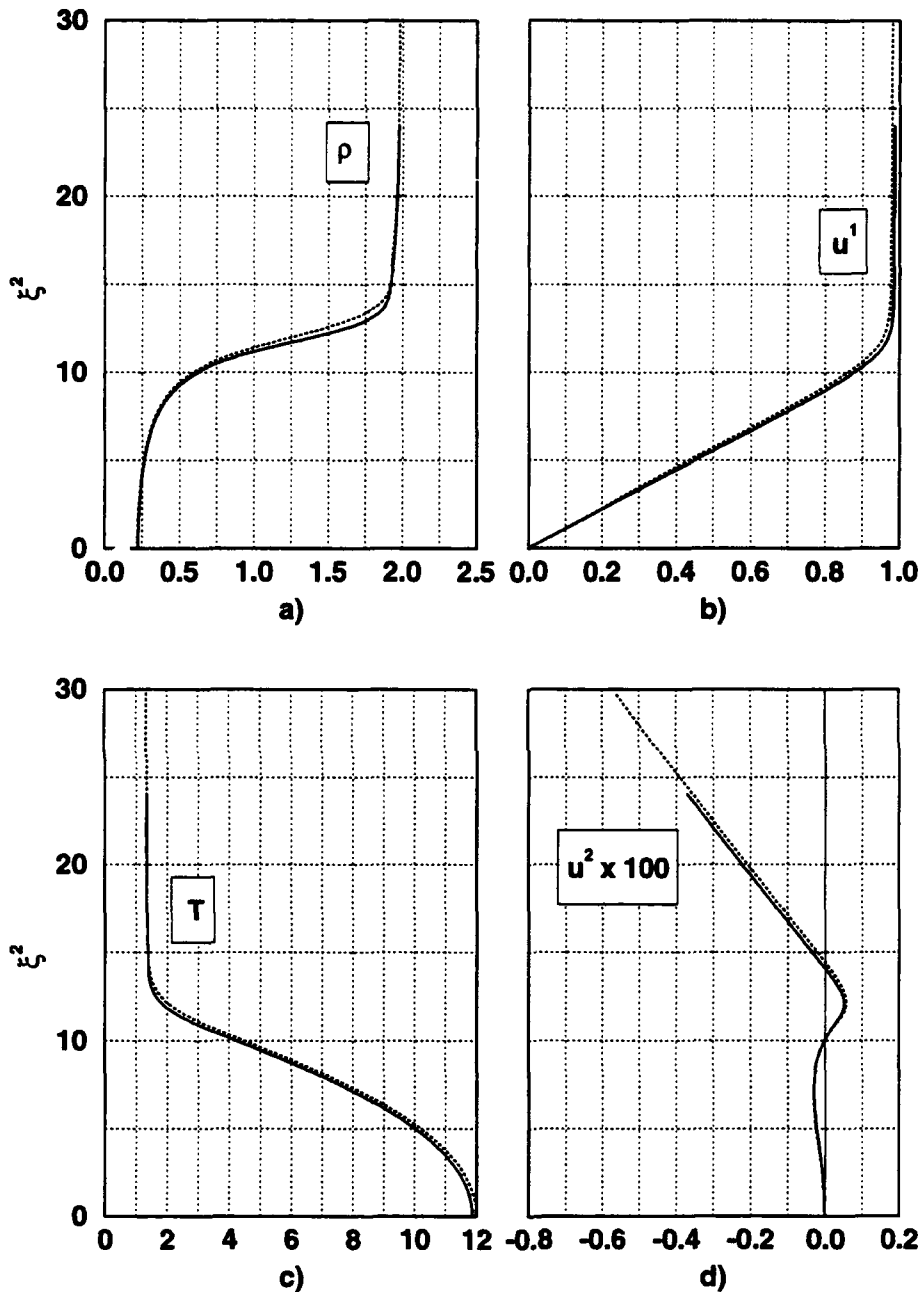


Figure 5.1: Comparison of TLNS and AFWAL PNS Basic State Profiles of the Flow Over a Blunt, 7° Half-Angle Cone. $s/R_N = 175$ (interpolated). Bow shock at $\xi^2 \approx 150$. Solid line: TLNS solution. Dotted line: AFWAL PNS solution. a) Density. b) ξ^1 contravariant velocity component. c) Temperature. d) ξ^2 contravariant velocity component $\times 100$.

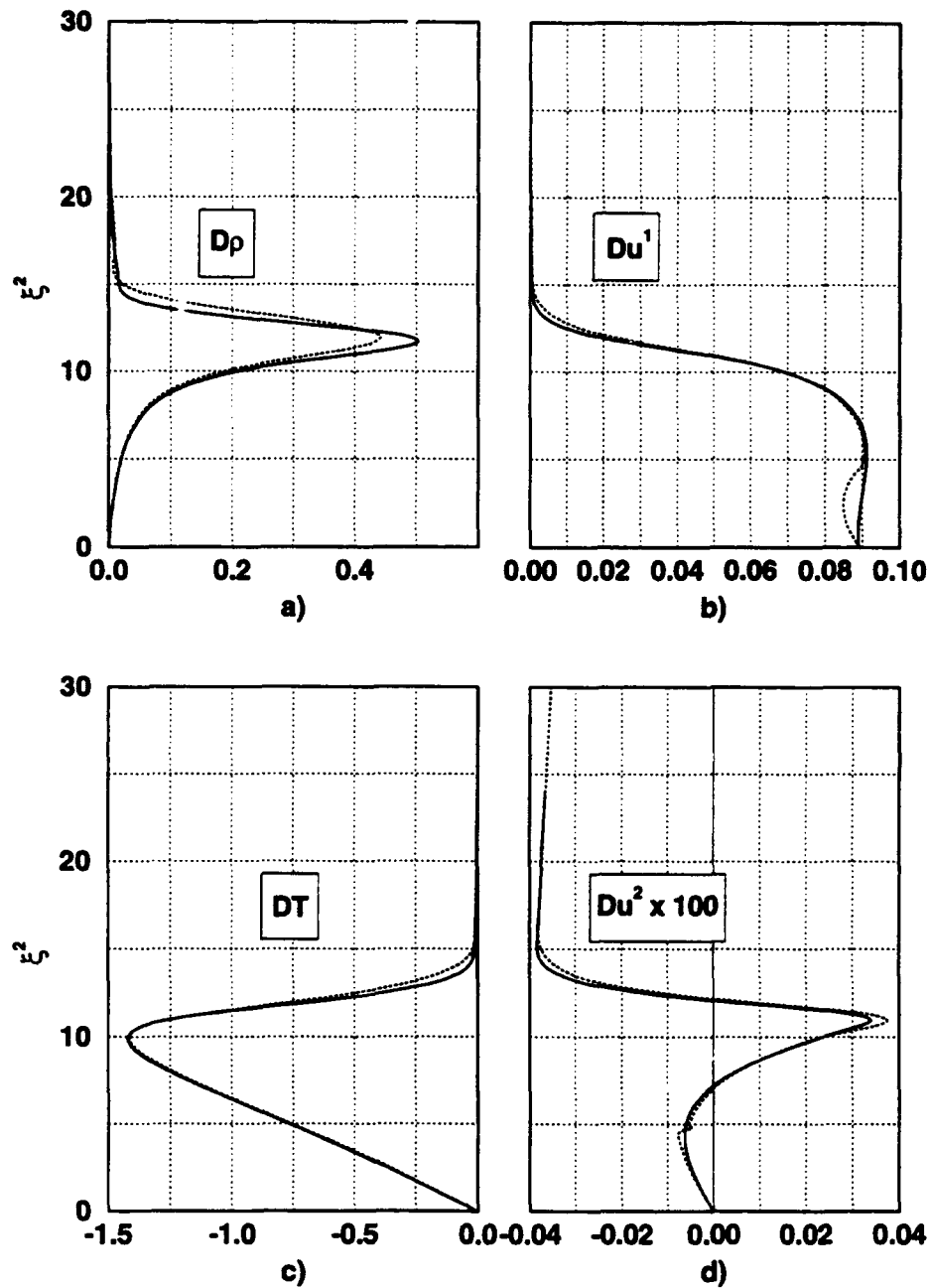


Figure 5.2: Comparison of TLNS and AFWAL PNS Basic State Profiles of the Flow Over a Blunt, 7° Half-Angle Cone. $s/R_N = 175$ (interpolated). Bow shock at $\xi^2 \approx 150$. First derivatives with respect to ξ^2 . Solid line: TLNS solution. Dotted line: AFWAL PNS solution. a) Density. b) ξ^1 contravariant velocity component. c) Temperature. d) ξ^2 contravariant velocity component $\times 100$.

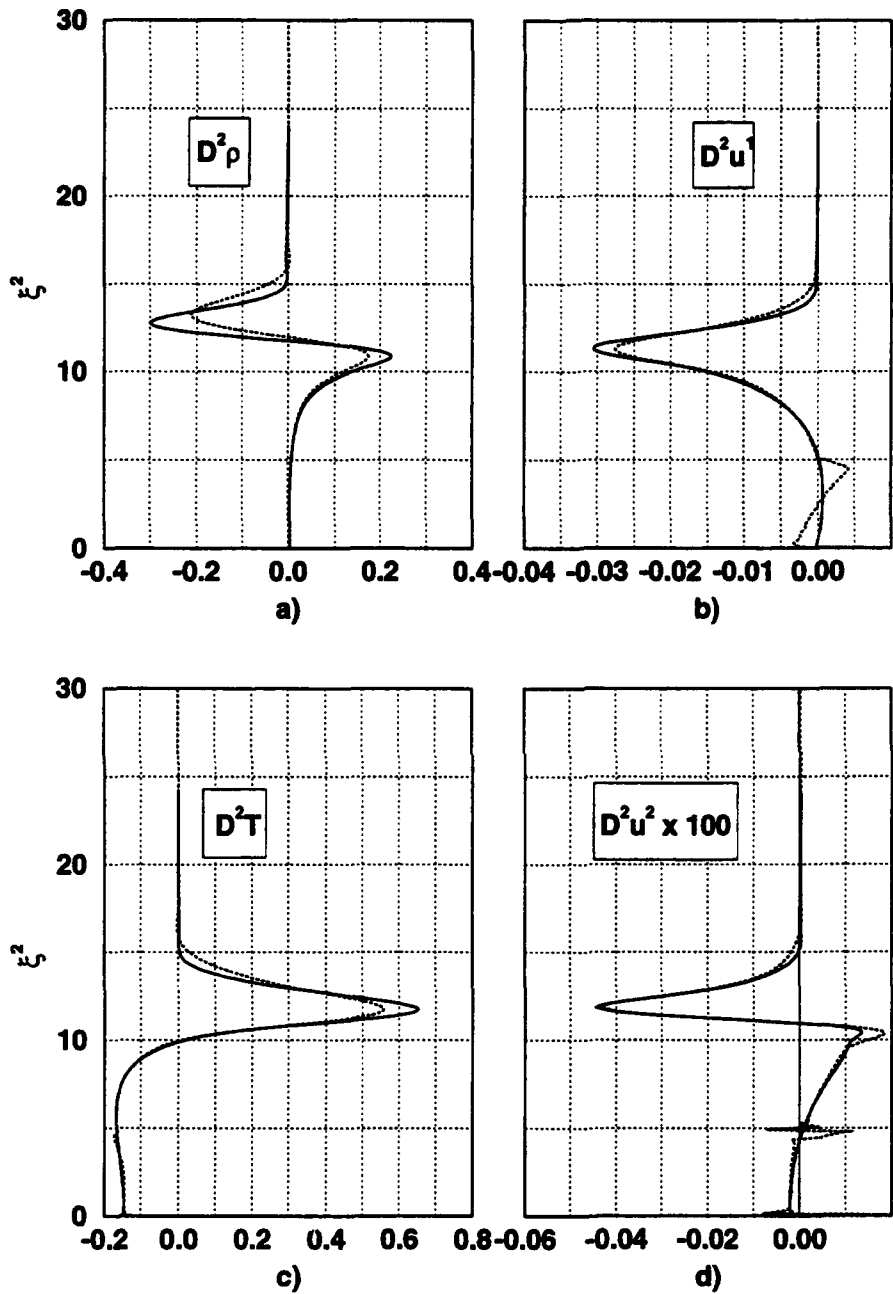


Figure 5.3: Comparison of TLNS and AFWAL PNS Basic State Profiles of the Flow Over a Blunt, 7° Half-Angle Cone. $s/R_N = 175$ (interpolated). Bow shock at $\xi^2 \approx 150$. Second derivatives with respect to ξ^2 . Solid line: TLNS solution. Dotted line: AFWAL PNS solution. a) Density. b) ξ^1 contravariant velocity component. c) Temperature. d) ξ^2 contravariant velocity component x 100.

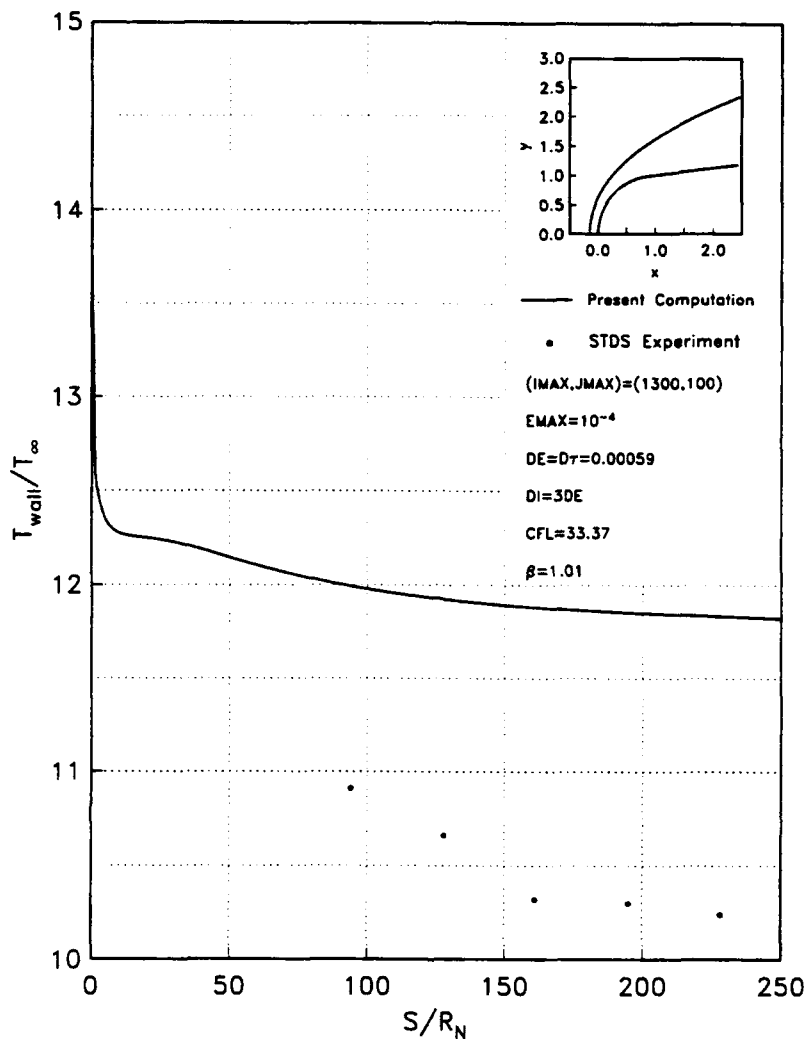


Figure 5.4: Temperature Along the Cone Surface.

sent the experimental properties. Typical mean-flow velocity (parallel to the surface) profiles are compared in Figure 5.5. Differences near the wall are due to inaccuracies in experimental measurements near the wall due to the large probe size. Figure 5.6 shows that the shock shape predicted by the TLNS solution is in good agreement with the experimental result.

Virtually all of the blunt cone stability analyses were conducted with the TLNS basic state solution. The stability analysis of the AFWAL PNS blunt cone basic state was performed mainly to test and validate the software modules developed for the studies of the sharp cone at angle of attack. As an additional benefit, this work also provided some indication of the relative accuracy of the eigenvalues that can be expected when using the AFWAL PNS basic state profiles.

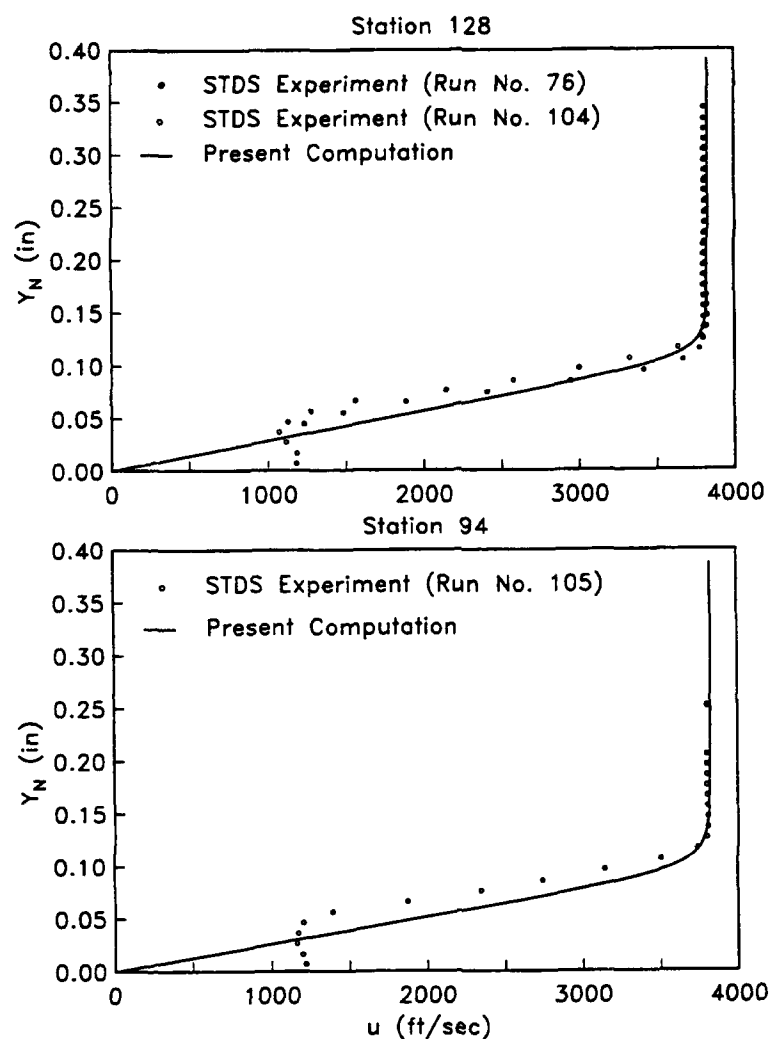


Figure 5.5: Basic State Streamwise Velocity Profiles at $s^*/R_N = 128$ and 94.

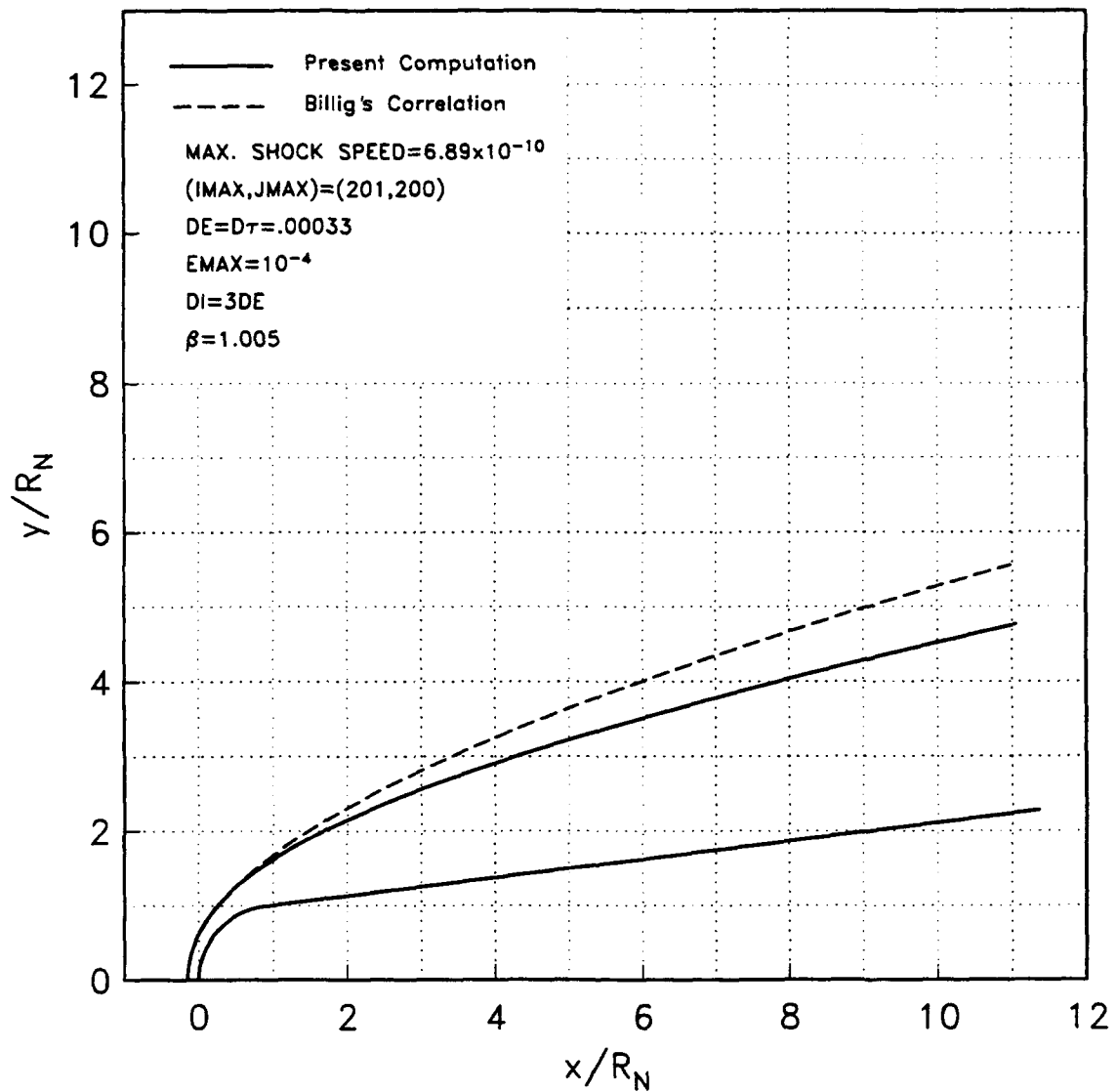


Figure 5.6: Shock Shape Comparison with Billig's Correlation and the STDS Experiment.

5.2 Reference Scales for Stability Analysis

Boundary-layer edge values of the basic state vary with streamwise distance for a blunt cone, unlike those for a sharp cone. Therefore, instead of using edge values (as in the experiments of Stetson et al.) fixed basic-state freestream values of temperature ($T_\infty^* = 54.3\text{ K}$) and pressure ($p_\infty^* = .004082743\text{ atm.}$) are used as reference values. The station at $s^*/R_N = 175$, where R_N is the radius of the spherical nose ($s^* = 0.66675\text{m}$). was input as a reference station. The reference length scale $r1$, is the boundary-layer length scale

$$\sqrt{\frac{\nu s^*}{U_\infty}} = 2.8511 \times 10^{-4} \text{ m}$$

at this reference station, $s^*/R_N = 175$. Hence the square-root of local Reynolds number $R = \sqrt{R_{s^*}}$ is related to the length scale as $r1 = s_{ref}^*/R_{ref}$ and nondimensional distance $s = s^*/r1$ is related to R as

$$R = \sqrt{s R_{ref}}$$

The Prandtl number is specified as 0.72, the same value used in basic state solution.

5.3 Stability Analysis Coordinates

Two different coordinate systems are used for the local stability and PSE analyses here. They are axisymmetric body-intrinsic coordinates ($\xi^1 = s$, $\xi^2 = \eta$, $\xi^3 = \phi$). and local Cartesian coordinates aligned with the cone surface.

Body-Intrinsic Coordinates

This coordinate system (Figure 5.7) is used when `icoord=1` is specified in the input file **Definitions**. Transformation from Cartesian coordinates:

$$\begin{aligned} x^1 &= x \\ x^2 &= y \\ x^3 &= z \end{aligned}$$

to:

$$\begin{aligned} \xi^1 &= s; \text{ arc-length along the body} \\ \xi^2 &= \eta; \text{ normal distance from the body surface} \\ \xi^3 &= \phi; \text{ azimuthal angle} \end{aligned}$$

is given by the following equations.

$$\begin{aligned} x &= \{x_b(s) - \eta \sin(\theta_c(s))\} \\ y &= \{r_b(s) + \eta \cos(\theta_c(s))\} \sin(\phi) \\ z &= \{r_b(s) + \eta \cos(\theta_c(s))\} \cos(\phi) \end{aligned}$$

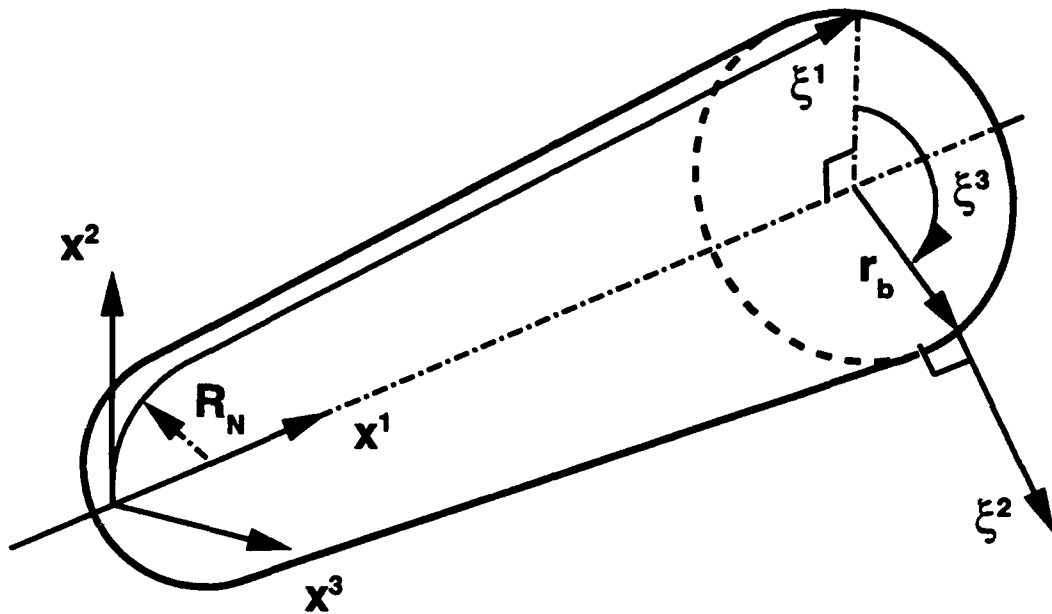


Figure 5.7: Body-Intrinsic Coordinate System Used for Stability Analysis

where $r_b(s)$ is the radius of the body, $x_b(s)$ is the axial distance, and $\tan\{\theta_c(s)\}$ is the slope, at the body surface ($\eta = 0$). Since the basic flow is axisymmetric, and disturbances are periodic in ξ^3 direction with a wave number n_ϕ .

Local Cartesian Coordinates

This coordinate system is used for stability analysis when `icoord=0` is specified. Here, all curvature terms and cone divergence are neglected.

$$x = s$$

$$y = \eta$$

$$z = z$$

$$\begin{aligned}\frac{\partial x^1}{\partial \xi^1} &= \frac{\partial x}{\partial s} = 1 \\ \frac{\partial x^2}{\partial \xi^2} &= \frac{\partial y}{\partial \eta} = 1 \\ \frac{\partial x^3}{\partial \xi^3} &= \frac{\partial z}{\partial z} = 1\end{aligned}$$

5.4 Dependent Variables

The codes LSH and PSH provide several sets of disturbance variables to be used in the analysis. The results presented for the blunt cone are obtained using $\tilde{\rho}$, \tilde{T} and physical contravariant velocity components in curvilinear coordinates as dependent variables. For this hypersonic flow, grid resolution is required not only near the wall, but also at the boundary-layer edge. Results here are obtained using 200 to 220 grid points in the normal direction with uniform spacing. A mild logarithmic stretching is used in some cases.

5.5 Linear Stability Analysis

Different families of eigensolutions exist for hypersonic boundary layers, as pointed out by Mack (1986). Hence careful guesses of eigenvalues are required for local eigenvalue calculations to converge to the desired (usually unstable) eigenvalue. Three families of spatial eigenvalues for two-dimensional waves at a fixed streamwise (ξ^1) station ($s^*/R_N = 175, R = 2338.535$) are shown in Figure 5.8. Nonparallel effects due to basic-state streamwise gradients and normal velocity are taken into account in these calculations. Spatial growth rates $\sigma = -\alpha_r$ and wavespeed are plotted against wavenumber α_r in the top and bottom plots, respectively. The family S_u consists of stable first-mode solutions and unstable second-mode solutions. The phase speed of this family approaches $1 - \frac{1}{M_e}$ as the wavenumber approaches zero. Two families (S_{d1}, S_{d2}) are damped for all wavenumbers. The wavespeeds of these families approach $1 + \frac{1}{M_e}$ as the wavenumber decreases.

Typical amplitude profiles of eigenfunctions $\tilde{\rho}$, \tilde{T} , \tilde{u} and \tilde{v} , for an unstable second mode are shown in Figure 5.9. It is clear that large gradients exist not only near the wall but also near the boundary layer edge where the critical layer is. Either homogeneous conditions or asymptotic conditions for disturbances are used at the freestream boundary. Amplitude profiles are predicted accurately by both boundary conditions but small oscillations in phase near η_{max} are observed in solutions obtained with homogeneous boundary conditions. Note that the phase is obtained by taking the inverse tangent of the ratio between real and imaginary parts of eigenfunctions. Errors are not visible in real and imaginary parts themselves as they are very small near the outer boundary. But errors are amplified enough to be observed when the ratio is taken. The use of asymptotic boundary condition gives phase profiles that are free of these oscillations and allows the use of a shorter domain in η .

Growth rate vs. frequency plots for disturbances of different azimuthal wavenumbers n_ϕ at the reference station is shown in Figure 5.10. Basic-state nonparallel terms are included in the calculations. For three-dimensional (3D) waves, both first mode and second mode disturbances are found to have unstable frequency ranges. For the 2D wave, the first mode is stable (with basic-state nonparallel terms included). For the second-mode instability, 2D waves ($n_\phi = 0$) are found to be the most unstable.

The growth rate of 2D second-mode disturbances computed using the AFWAL PNS code is compared to that obtained with the TLNS solution in Figure 5.11. Two different curves are shown for the AFWAL PNS solutions. One curve corresponds to

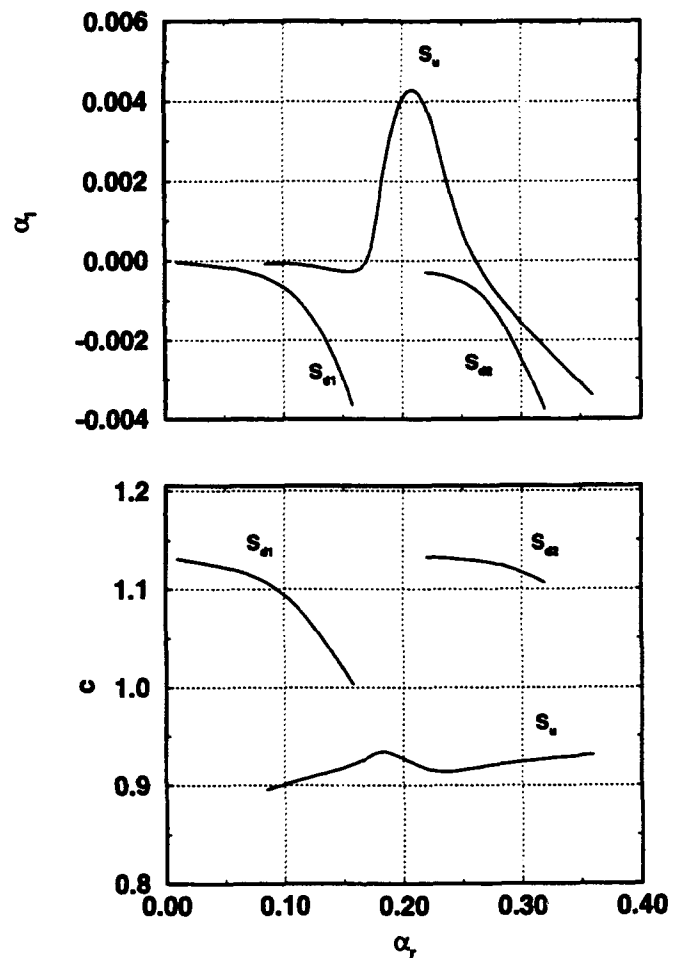


Figure 5.8: Families of Eigensolutions at Station $s^*/R_N = 175$

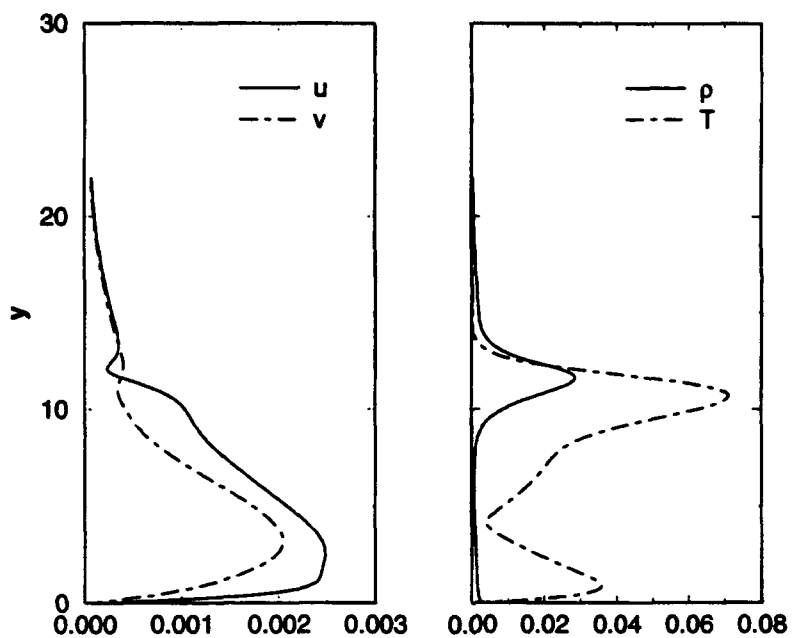


Figure 5.9: Amplitude Profiles of the Eigensolution at Station $s^*/R_N = 175$ and $F \times 10^6 = 82.7$.

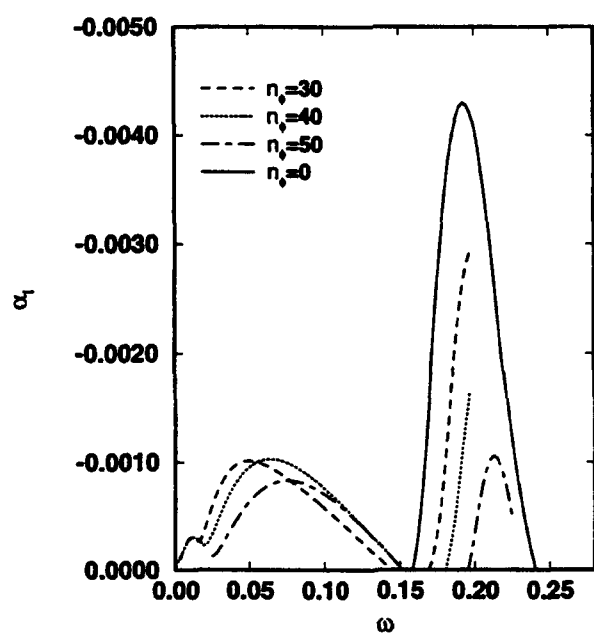


Figure 5.10: Growth Rate Variation with Frequency at $s^*/R_N = 175$.

the AFWAL PNS solution with 251 radial grid points, and the other corresponds to the AFWAL PNS solution with 501 radial grid points. All of the stability analyses include the effects of the transverse curvature of the cone but neglect the ξ^2 velocity component (radial or normal) and the ξ^1 derivatives of the basic state. (The ξ^3 derivatives of the basic state are, of course, identically zero because the flow is axisymmetric.) Moreover, the analyses use homogeneous boundary conditions near the shock.

The Reynolds number R shown on the abscissa in Figure 5.11 is the square root of the Reynolds number based on the free-stream conditions and the arc length s^* measured along the body surface.¹ Also, the growth rate in Figure 5.11 has been nondimensionalized with the length scale $r_1 = s^*/R_{ref}$.

The first thing to note is that the growth rates computed with the different AFWAL PNS solutions are more stable than the growth rate computed with the TLNS solution. Moreover, the errors in the AFWAL PNS solutions lead to quite significant errors in the growth rates. In fact, the growth rate obtained with the 501 point AFWAL PNS solution is approximately 10% low at the local maximum. The analyses of the AFWAL PNS solutions also predict that the local maximum occurs at a station slightly closer to the apex of the cone. Nevertheless, the growth rate computed from the AFWAL PNS solutions appears to be converging to the result obtained from the TLNS solution.

Most of the differences between the computed growth rates are, thus, likely attributable to inaccuracies in the basic state solutions. However, if the AFWAL PNS grid is refined even more, it may be that the different nonparallel effects in the slightly different coordinate systems will still cause the growth rates to be slightly different. This issue could be resolved by comparing the PSE results. In the interest of studying a three-dimensional basic state flow (Section 4) within the contract period, though, we did not spend any additional time solving the PSE for the AFWAL PNS basic state. Instead, the TLNS blunt cone solution was used for all of the following detailed local and PSE analyses.

Variations of growth rate with Reynolds number R at a fixed frequency ($F \times 10^6 = 82.7$) for 2D second-mode disturbances are plotted in Figure 5.12 and Figure 5.13. The effect of including cone curvature terms is to decrease the growth rate from that obtained using local Cartesian coordinates (Figure 5.12). Including basic-state nonparallel terms shifts the growth rate curve to the left, resulting in a lower value of R at branch I neutral point (Figure 5.13). Both types of boundary condition at the far-field, asymptotic and homogeneous conditions, essentially give the same results.

Next, variations of growth rate (Figure 5.14) and wave speed (Figure 5.15) with Reynolds number R for different values of frequency parameter F are presented. Basic-state nonparallel terms are included in these calculations. The range of unstable frequencies gets lower with increasing R while the range of wave speeds increases. This is in accord with the fact that the wavelength of unstable modes scales with boundary-layer thickness which increases with Reynolds number. Corresponding amplitude

¹The results from the PNS coordinate system had to be transformed according to $s/R_N = \arccos(1 - x^1/R_N)$ for $0 \leq x^1/R_N \leq 1 - \sin(\theta_c)$ and $s/R_N = \frac{\pi}{2} - \theta_c + (x^1/R_N - (1 - \sin(\theta_c)))$ for $x^1/R_N \geq 1 - \sin(\theta_c)$

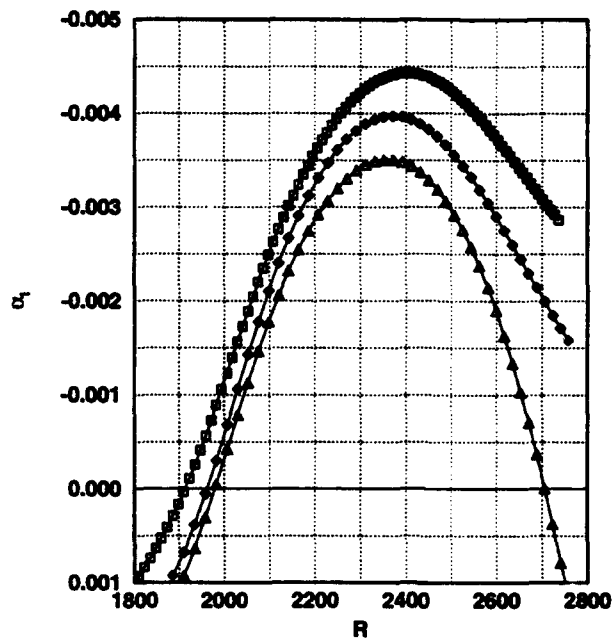


Figure 5.11: Comparison of Computed Spatial Growth Rates as a Function of Surface Arc Length Using Two Different Basic State Solutions. $F = 82.7$. \square) TLNS solution, 200 wall normal points. \diamond) AFWAL PNS solution, 501 radial points. \triangle) AFWAL PNS solution, 251 radial points.

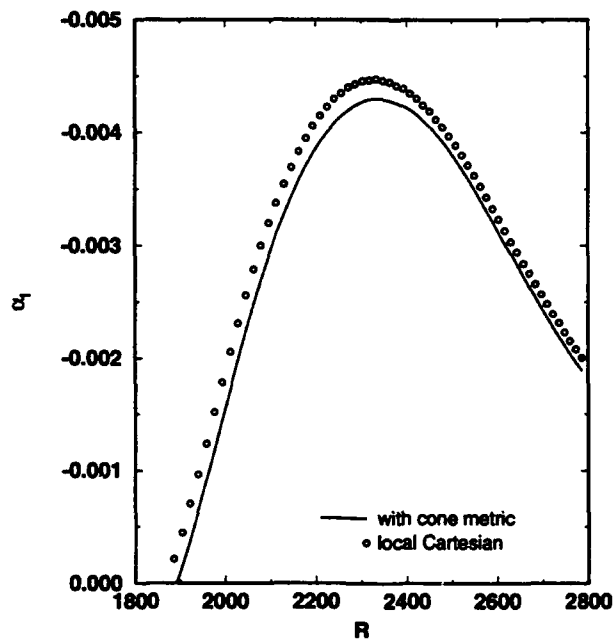


Figure 5.12: Effect of Curvature on Second-Mode Growth Rate Variation with R at $F \times 10^6 = 82.7$.

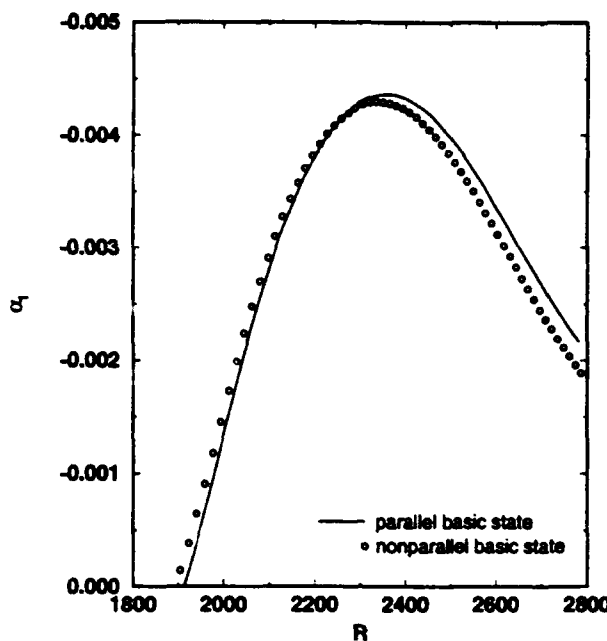


Figure 5.13: Effect of Nonparallel Basic State on Second-Mode Growth Rate Variation with R at $F \times 10^6 = 82.7$.

ratio curves (N factor curves) are given in Figure 5.16. The maximum N-factor according to this linear stability theory is about 5.6 near the end of the cone ($s^*/R_N = 235$).

Figure 5.17 gives growth rate vs. R curves for 3D second-mode waves at $F=82.7$ and for different azimuthal wave numbers n_ϕ . Difference in growth rates between different oblique modes becomes less at large R . This is due to the fact that for the fixed n_ϕ the wave angle approaches zero as the radius of the cone decreases. Neutral stability curves for these 2D second-mode disturbances including nonparallel effects of basic state are plotted in Figure 5.18. Minimum critical Reynolds number for the second-mode instability is predicted to be at $R_{\text{crit}} = 1480$. This value is lower than that observed by Stetson et al. Note that the Reynolds number in their experiments is defined in terms of the boundary-layer edge reference value. Reynolds number in our case can be related to theirs by

$$R = R_{\text{Stetson}} \sqrt{(U_\infty \rho_\infty \mu_e) / (U_e \rho_e \mu_\infty)}$$

5.6 Results of Linear PSE

Local solutions obtained from LSH, taking nonparallel effect of mean flow into account when appropriate, are specified as initial conditions for the PSE calculating PSH. In addition to streamwise gradient of the mean flow, nonparallel effects due to streamwise variations of shape function f and amplitude modulation are properly taken into

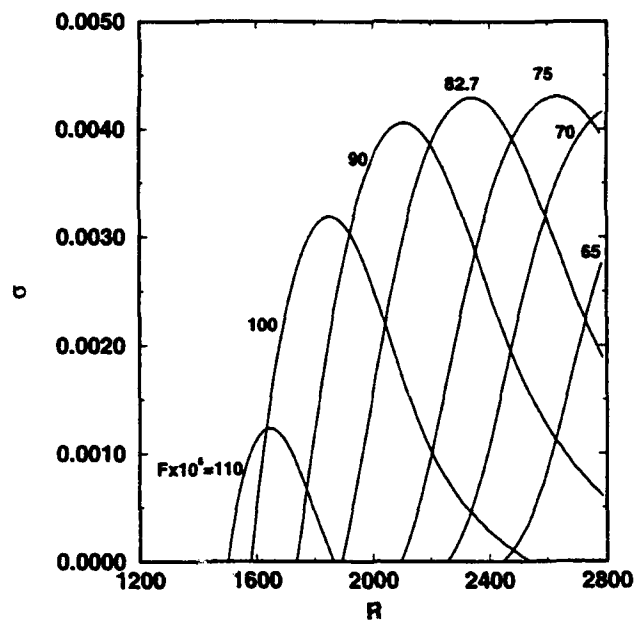


Figure 5.14: Second-Mode Growth Rate Variation with R at Different Frequencies.

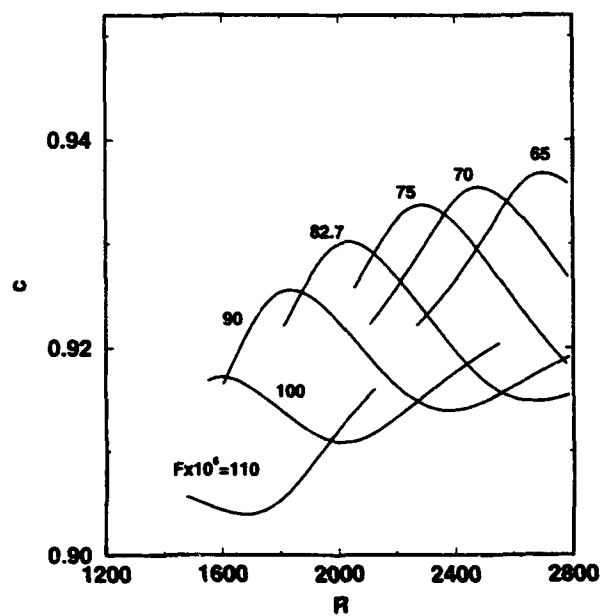


Figure 5.15: Wave Speed Variation with R at Different Frequencies.

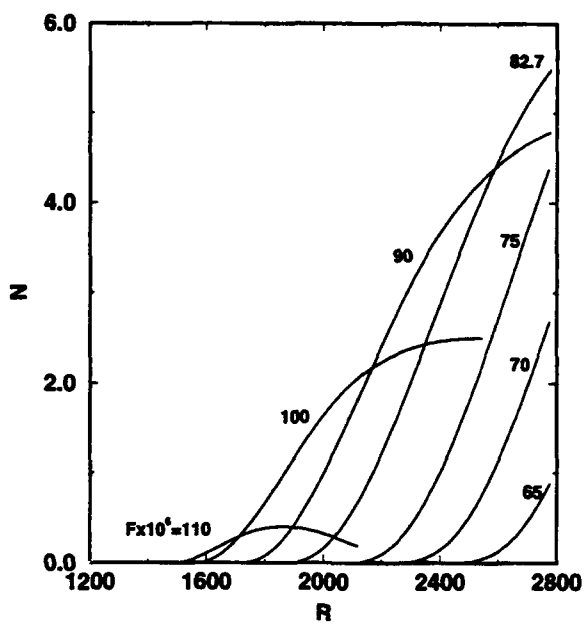


Figure 5.16: N-Factor Variation with R at Different Frequencies.

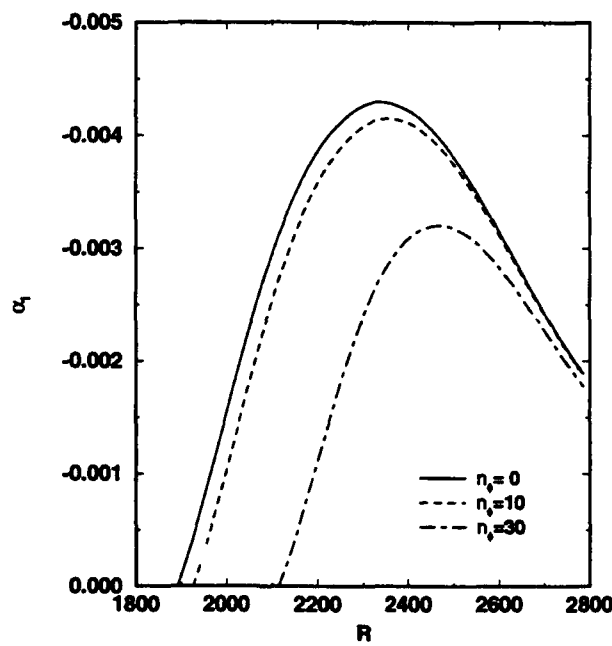


Figure 5.17: Second-Mode Growth Rate Variation with R for Different Azimuthal Wavenumbers.

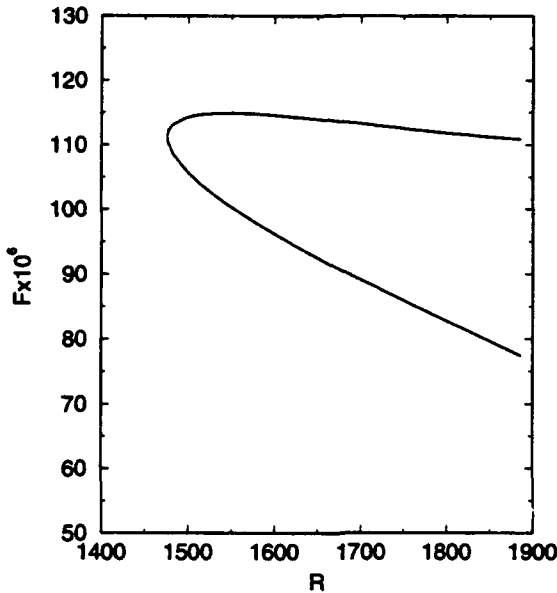


Figure 5.18: Neutral Stability Curve for Second-Mode 2D Disturbances.

account in PSE analyses. Effective growth rate for a disturbance variable \tilde{q}^i is defined as

$$\sigma_{q^i} = Re \left\{ \frac{1}{\tilde{q}^i} \frac{\partial \tilde{q}^i}{\partial s} \right\} - Im \{ \alpha_i \}$$

where α_i is the imaginary part of the streamwise wavenumber and s is the body intrinsic direction. Due to nonparallel effects (of basic-state and disturbance), growth rates of different variables will be different. These will depend not only on s (R), but also on normal distance from the wall η .

Variation of growth rates based on maximum streamwise disturbance velocity \tilde{u}_{max} at different frequency parameters F , is presented in Figure 5.19. Corresponding amplitude ratios (N factors) are given in Figure 5.20. The difference between this PSE result and that of LSH (Figure 5.16) is larger at lower Reynolds numbers R (or higher frequency range) where nonparallel effects are the larger. For each frequency parameter F , the location of branch I neutral point is predicted by linear PSE at a higher Reynolds number than that by local analysis.

In experiments of Stetson et al. (1984), mass flow fluctuations are measured for growth rate. In our calculations, massflow fluctuation is defined as

$$\tilde{m} = \tilde{\rho} \tilde{u} = \tilde{\rho} u + \rho \tilde{u}$$

where \tilde{u} is the disturbance velocity component in s -direction of the stability coordinates. Figure 5.21 shows amplitude profile and massflow fluctuation and its growth rate variation with normal distance η at a fixed station $R = 2309$ and $F \times 10^6 = 82.7$. In Stetson et al. (1984) growth rate is defined in nomenclature as

$$\sigma = \frac{2}{R_{Stetson}} \frac{\partial A}{\partial R_{Stetson}}$$

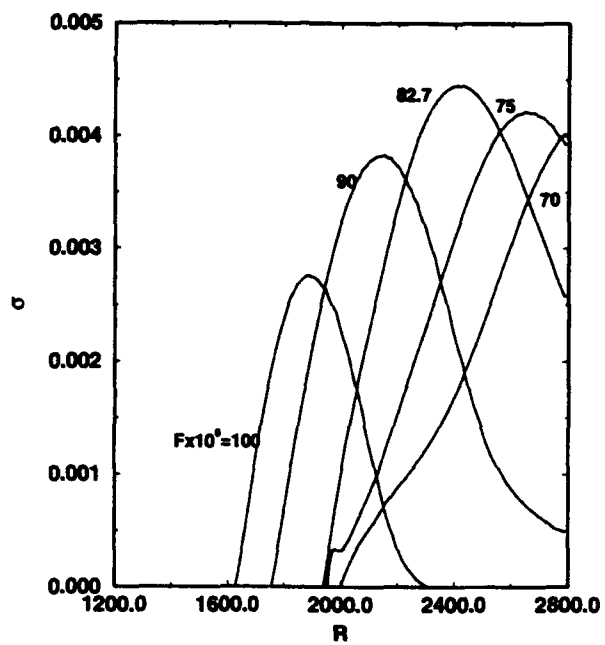


Figure 5.19: Variation of Growth Rate of Maximum u with R at Different Frequencies.

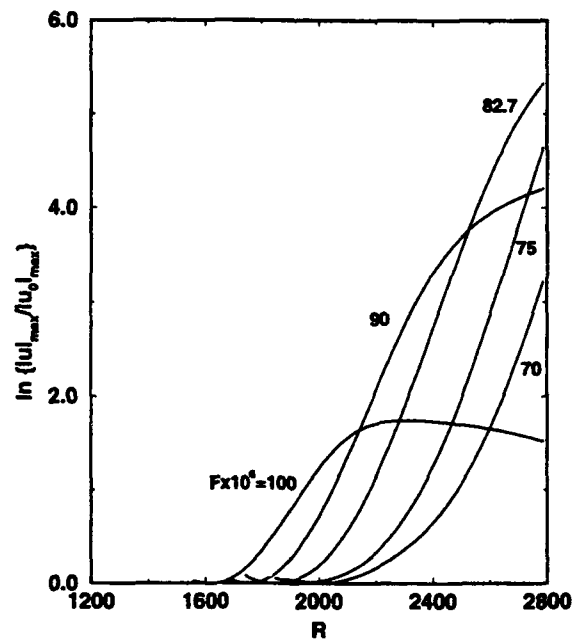


Figure 5.20: Variation of Maximum Amplitude of u with R at Different Frequencies.

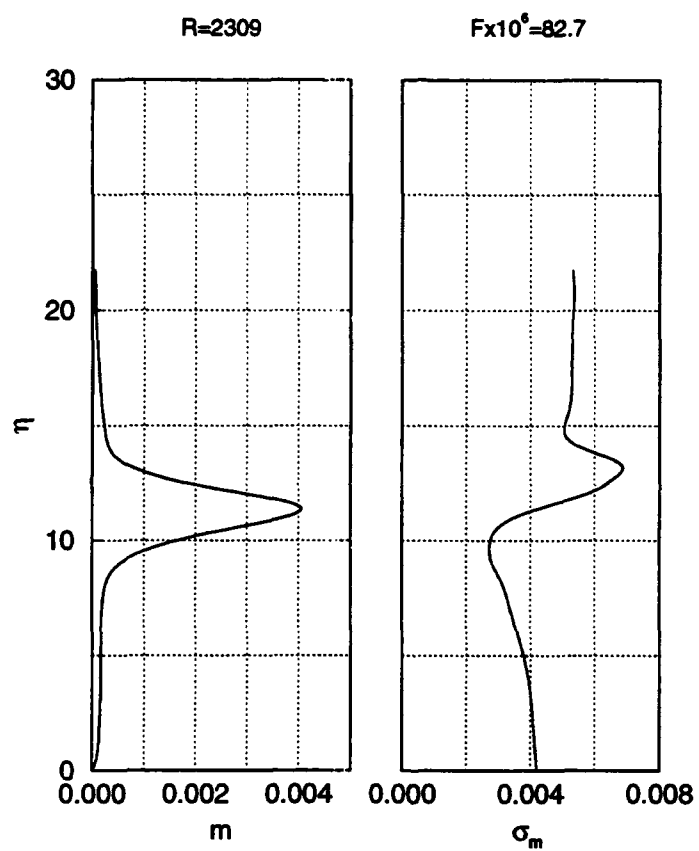


Figure 5.21: Profiles of Amplitude and Growth Rate of Massflow Fluctuations at $R = 2309, F \times 10^6 = 82.7$.

where $R_{Stetson}$ is based on edge values and distance measured in surface direction s . This implies that differentiations is in s direction holding η constant. On the other hand, they are obtained by measuring the maximum in massflow fluctuations which occurs near the boundary layer edge. Therefore, it is not clear whether normal distance from wall η in our notation is held constant in their growth rate evaluation. In any case, since the growth rate varies rapidly in η near this location, slight variation in measurement position will cause large variation in measured growth rate.

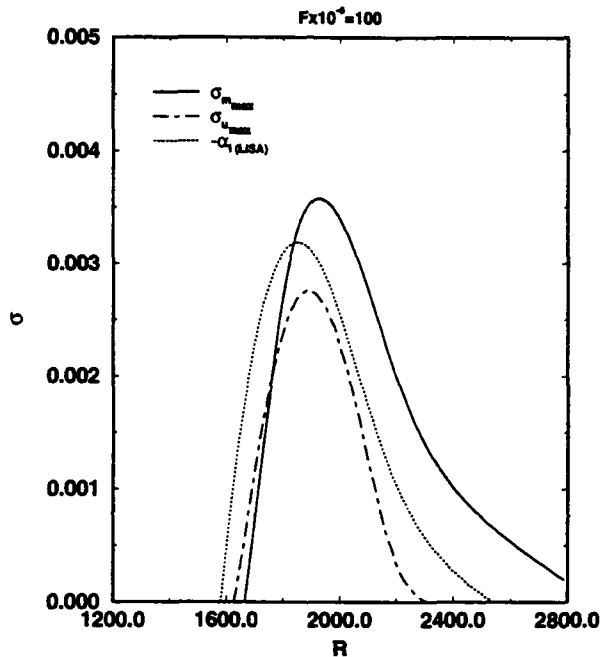


Figure 5.22: Variation of Growth Rates with R at $F \times 10^6 = 100$.

Variation of growth rates with R , based on maximum massflow fluctuations, (\tilde{m}_{max}) and maximum streamwise velocity (\tilde{u}_{max}), are given in Figure 5.22. Growth rate obtained from LSH is also shown for comparison. Note that simply measuring a different variable i.e., \tilde{m} instead of \tilde{u} , results in a shift in predicted branch I and branch II neutral points further downstream (higher R). Using \tilde{m} gives higher growth rates than using \tilde{u} . Amplitude ratios at different frequencies are plotted vs. R in Figure 5.23. The maximum N-factor is higher than that predicted with \tilde{u}_{max} and the evolution is quite different high values of F (compare with Figure 5.20).

Figure 5.24 shows evolution of maximum amplitude for different variables. Again, all amplitudes are scaled by freestream (preshock) fixed scales as opposed to experiments where boundary-layer edge values are used as a reference. Initial maximum amplitude for u at $R = 1520$ is specified at 0.01 percent of mean flow freestream value. This gives the initial amplitude of massflow disturbance of about 0.07 %. As observed in by Stetson et al., velocity fluctuations are much smaller than temperature fluctuations and massflow (or density) fluctuations. At the last streamwise station, the maximum amplitude of \tilde{T} is about 6.56 percent and that of \tilde{m} is about 1.55 per-

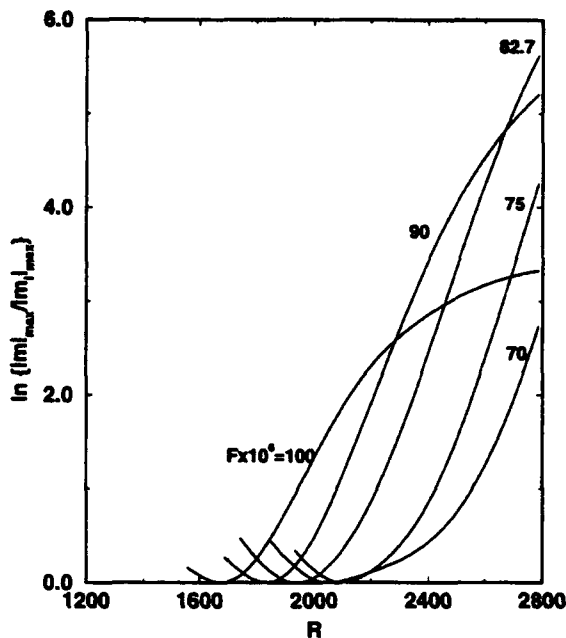


Figure 5.23: Variation of Maximum Amplitude of m with R at Different Frequencies.

cent. The slopes of the curves indicate that the growth rate of the maximum \tilde{u} is slower compared to that of the other three variables.

5.7 Results of Nonlinear PSE

Linear PSE calculations indicate that the use of different variables for calculating (or measuring) growth rates will give different results. It also shows a small shift in branch I neutral point downstream due to nonparallel effects. But growth rates obtained by linear PSE are still higher than experimental values, and, hence, this discrepancy cannot be accounted for by nonparallel effects alone. In experiments, the harmonics of the dominant frequency are observed at large R , indicating nonlinear effects are present. The branch I is also further downstream of that predicted by either local stability analysis or linear PSE analysis. In this section, Nonlinear PSE simulations are performed to explain the observance of higher harmonics in experiments.

5.7.1 2D waves

Nonlinear evolution of a 2D second-mode disturbance of fundamental frequency $F \times 10^6 = 82.7$ is first investigated. The fundamental frequency chosen is close to the dominant (fundamental) frequency in experimental measurements. The initial disturbance at $F \times 10^6 = 82.7$ is calculated by LSH at $R=1809.4$ ($s=1400$) including basic-state nonparallel terms. This disturbance is specified as an initial mode for PSH. The maximum index of temporal modes is $modt = 4$, i.e., first, second, and third

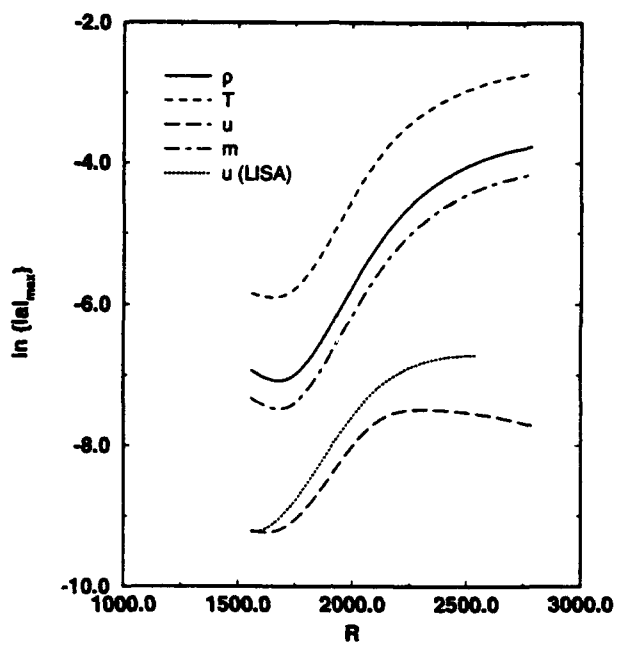


Figure 5.24: Evolution of Maximum Amplitude with R for Different Variables at $F \times 10^6 = 100$.

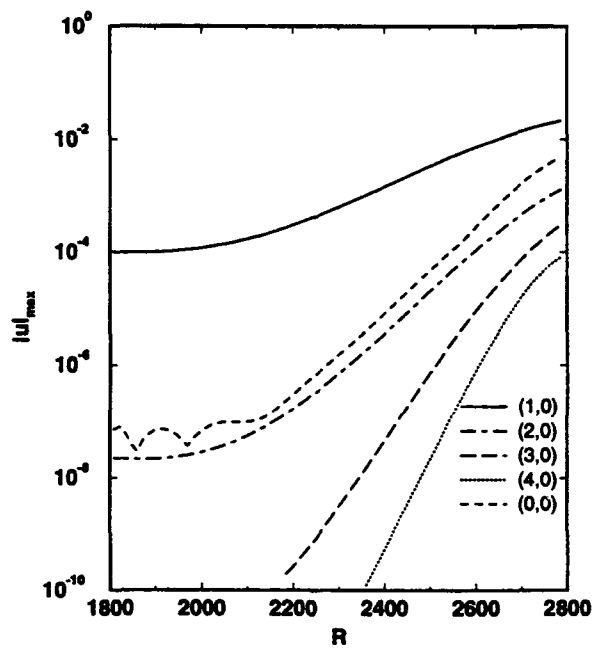


Figure 5.25: Variation of Amplitude of \tilde{u} with R for the Initial Amplitude of 10^{-4} .

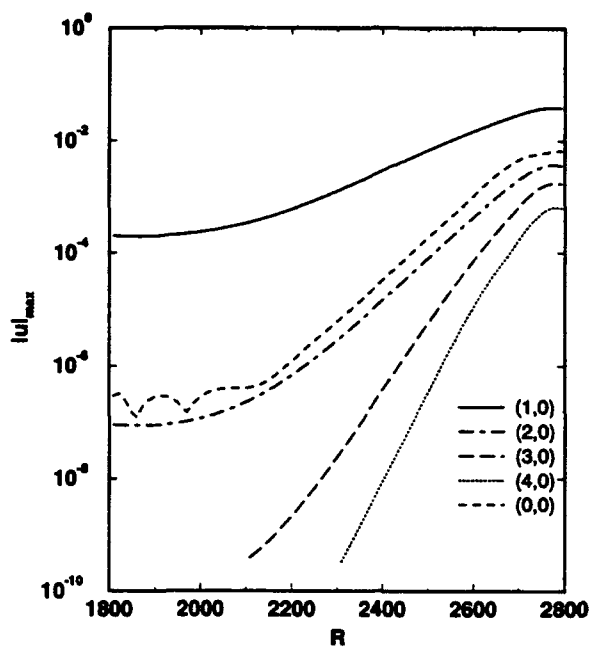


Figure 5.26: Variation of Amplitude of \tilde{u} with R for the Initial Amplitude of 2×10^{-4} .

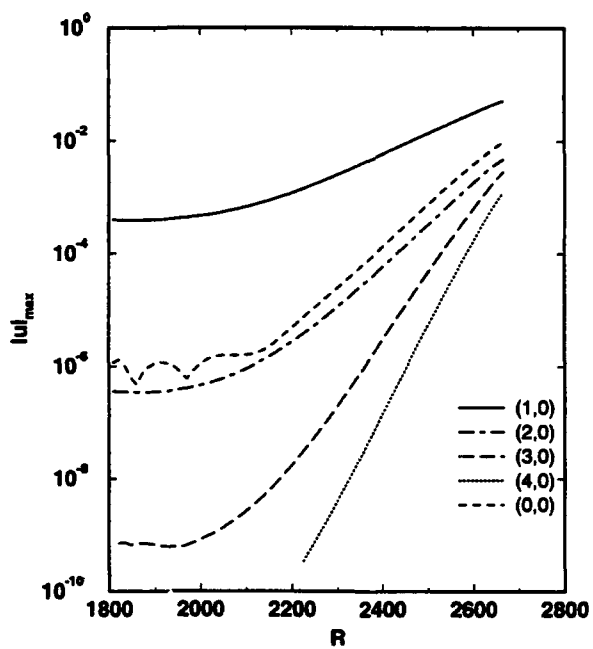


Figure 5.27: Variation of Amplitude of \tilde{u} with R for the Initial Amplitude of 4×10^{-4} .

harmonics of the initial mode are created by nonlinear forcing terms and followed as integration proceeds. Amplitude variation of the fundamental wave and its harmonics is given in Figure 5.25 to Figure 5.27 for three different initial amplitudes. Growth rate variation with R is plotted in Figure 5.28 for the initial \tilde{u} amplitude of 2×10^{-4} .

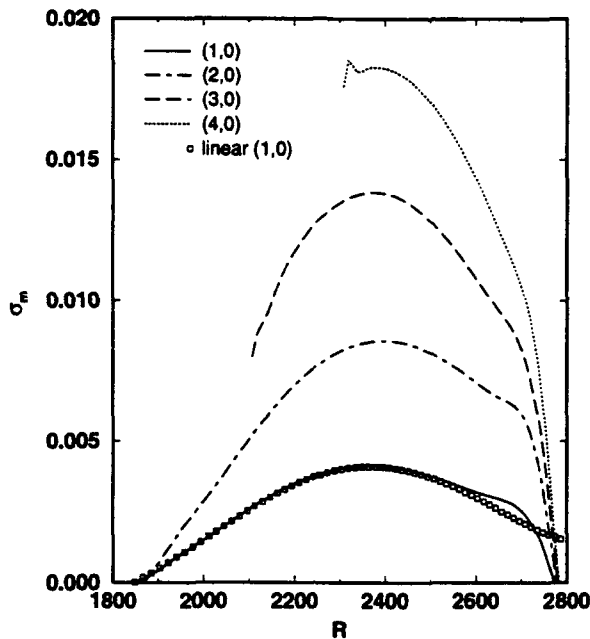


Figure 5.28: Variation of Growth Rates of \tilde{m} with R for the Initial \tilde{u} Amplitude of 2×10^{-4} .

Linear growth of the second-mode disturbance for the same initial amplitude of 10^{-4} is also given for comparison. For the case of lowest initial amplitude, nonlinear growth rate of the fundamental wave is close to that predicted by linear PSE, as expected. The main feature is that disturbances tend to decay at some value of R downstream (Figure 5.29) for larger initial amplitudes. This decay in amplitude is not apparent for initial amplitude of 4^{-4} . Even though the growth rate in this case is decreasing more rapidly than other case (Figure 5.29), large amplitudes of different modes cause transition to begin earlier before decay or saturation can be observed. The unstable range of R is decreased as the amplitude is increased, branch I moving downstream and branch II moving upstream.

The variation of skin friction coefficient for three-different initial amplitudes is given in Figure 5.30. The rapid rise in skin friction near the end of these plots can be taken as the beginning of the transition process. This shows that transition location is dependent on initial conditions.

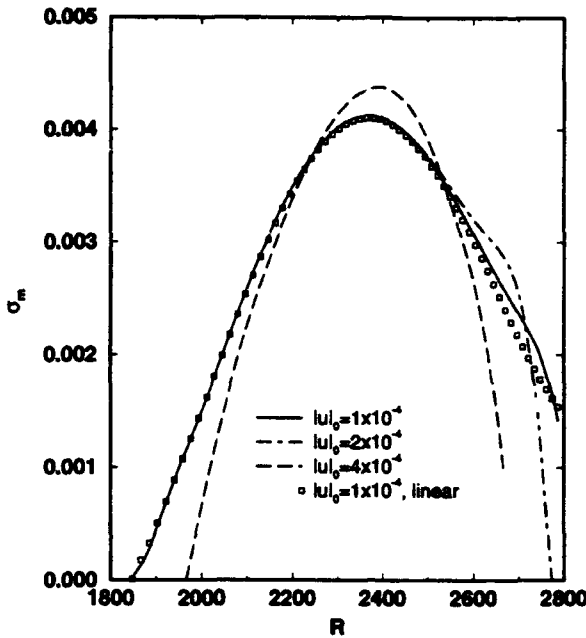


Figure 5.29: Variation of Growth Rate of \tilde{m} for Fundamental Mode with R for Different Initial \tilde{u} Amplitude.

5.7.2 3D waves

Since the actual transition process involves three dimensional structures, nonlinear development of 3D modes are studied here. First, nonlinear interaction of a 2D second-mode disturbance at $F \times 10^6 = 82.7$ and a 3D first-mode disturbance of half that frequency is investigated. The azimuthal wavenumber for the 3D disturbance is specified as 20. This value is kept constant in the integration process, in accord with the irrotationality condition. The initial \tilde{u} amplitudes of these two modes are set at 10^{-4} and 2×10^{-4} . No parametric excitation of the subharmonic wave is observed for this case. In fact, the growth rate (based on massflow fluctuation) of the first mode is decreased by nonlinearity, eventually leading to its decay around $R=2580$.

In the above calculation, higher harmonics of both first and second mode disturbances are neglected, except for the distortion. Moreover, the behavior of this first mode depends on its obliqueness, i.e., azimuthal wavenumber. Therefore, a similar run is performed, with the wavenumber increased to 30, and keeping the next order harmonics, i.e., modes (2,2), (3,1), (0,2), and (4,0) in the interactions. Evolution of maximum amplitude of \tilde{u} fluctuations for this case is given in Figure 5.33. Here, the subharmonic mode (1,1) does not decay. It grows but the growth rate is lower than that of the second mode (2,0) or the steady vortex (0,2) or oblique higher modes (3,1) and (2,2). The fundamental second mode amplitude remains an order of magnitude larger than those of the rest of the modes. Hence, unless the initial amplitude of the 3D subharmonic mode is significantly larger than the 2D wave, rapid rise in mean

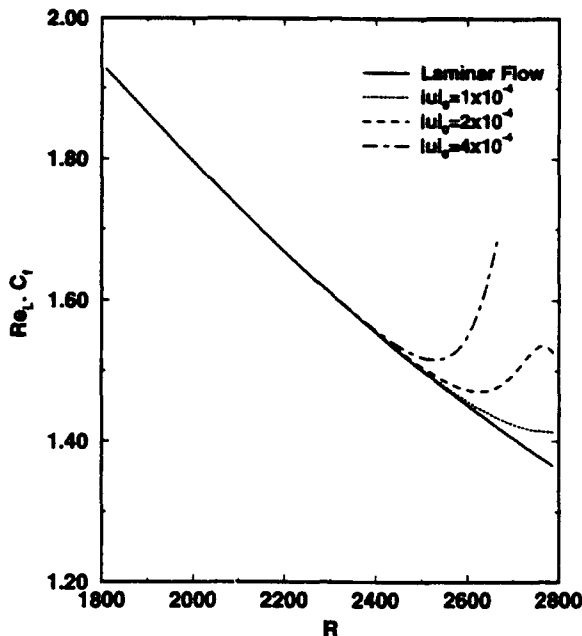


Figure 5.30: Variation of Mean Skin Friction Coefficient with R for Different Initial Amplitudes.

skin friction, and the beginning of breakdown is due to distortion by the 2D wave.

Since the dominant frequency observed in experiments is not as low as the first-mode 3D wave considered above, transition process occur most likely due to 3D second-mode waves and their harmonics. Hence, the interaction of two oblique second-mode disturbances of the same initial amplitude, the same frequency and symmetric in azimuthal direction is considered next. The azimuthal wavenumber, n_ϕ is chosen to be 16. This gives a wave angle of about 40 degrees at the initial location $s_0 = 900$. The frequency is $F = 82.7$ ($\omega = 0.1934$). Maximum index for temporal modes is 3 and maximum index for azimuthal wavenumber is 4. Therefore, there are 10 modes in the calculations. Amplitude evolution with R for various modes are shown in Figure 5.34. Three-dimensional modes are found to grow rapidly near the end of the cone, filling up the spectrum. In particular, steady streamwise vortices (0,2) and (0,4) modes are found to be growing very rapidly.

The skin friction coefficient for the mean flow is given in the next figure. Since steady vortices (0,2) and (0,4) modes contribute to streamwise component of the wall shear stress, steady skin friction is periodic in azimuthal direction. The maximum (peak in ϕ variation) amplitudes of skin friction is given in the same figure. It is evident that these vortices play a significant role in the rise of mean skin friction. The meanflow temperature at the wall is set to zero at the wall. Near this location of breakdown, heat transfer normal to the wall is found to increase rapidly. A similar run was conducted with adiabatic boundary condition for steady modes at the wall, giving similar results. In this case, mean wall temperature, instead of wall heat transfer, rises rapidly near breakdown.

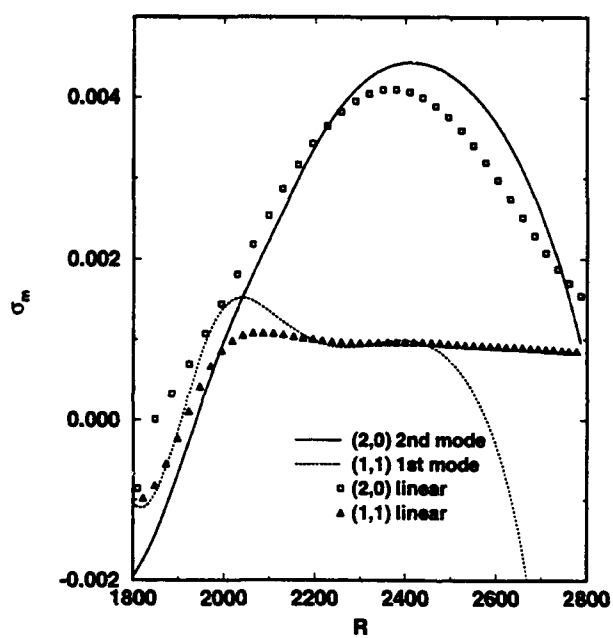


Figure 5.31: Interaction Between 2D Second Mode and a 3D First Mode of Half Frequency; Growth Rates of Massflow Fluctuations Measured at the Maximum Massflow Fluctuation for the Fundamental (2,0) Mode.

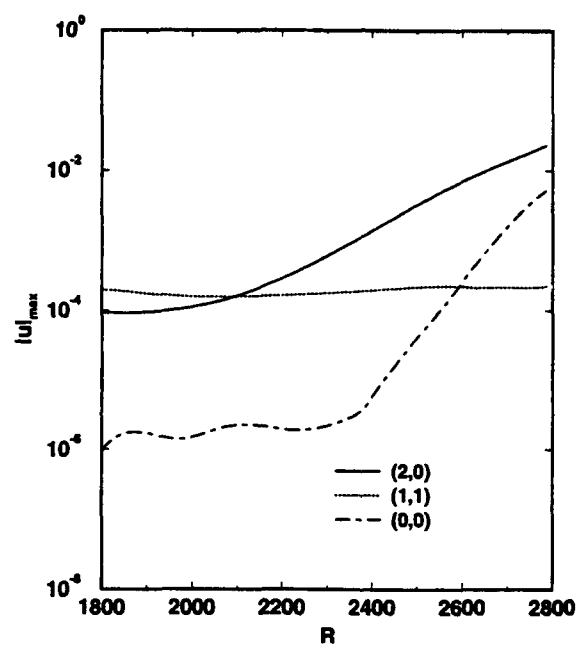


Figure 5.32: Interaction Between 2D Second Mode and a 3D First Mode of Half Frequency; Amplitudes of Massflow Fluctuations Measured at the Maximum Massflow Fluctuation for the Fundamental (2,0) Mode.

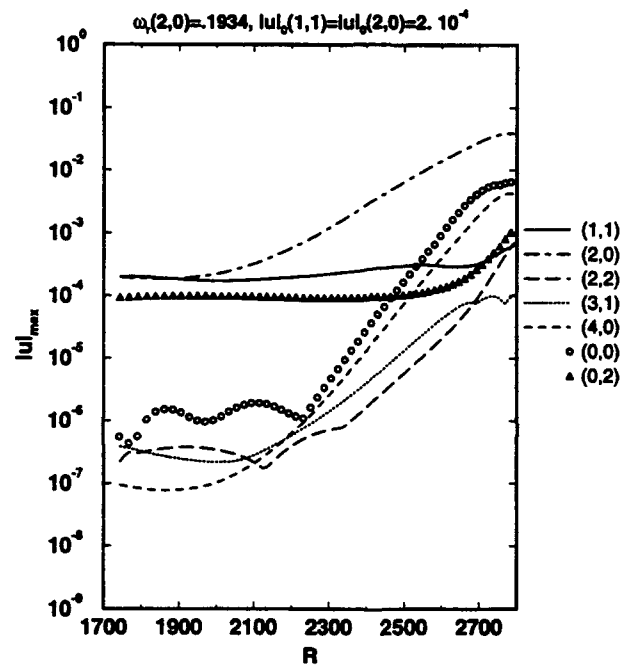


Figure 5.33: Interaction Between 2D Second Mode and a 3D First Mode Including More Harmonics; Amplitudes of Massflow Fluctuations Measured at the Maximum Massflow Fluctuation for the Fundamental (2,0) Mode.

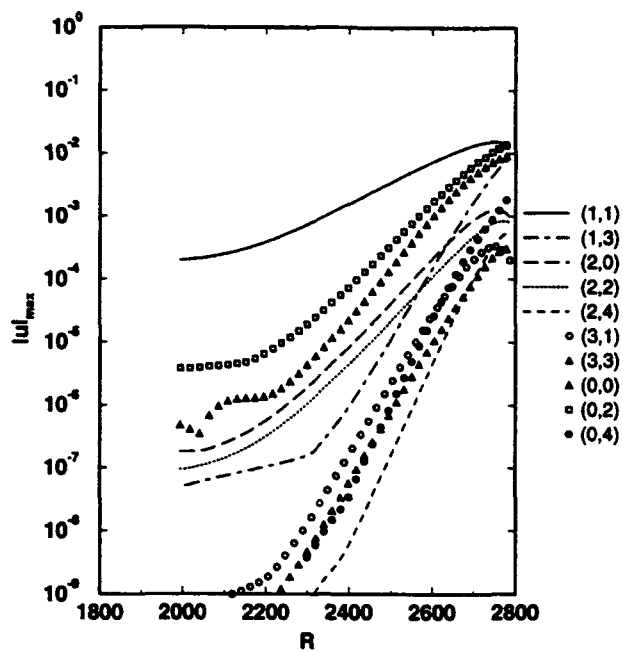


Figure 5.34: Nonlinear Interaction Between Two Oblique Second-Mode Waves: Amplitudes of Massflow Fluctuations Measured at the Maximum Massflow Fluctuation for the Fundamental (2,0) Mode.

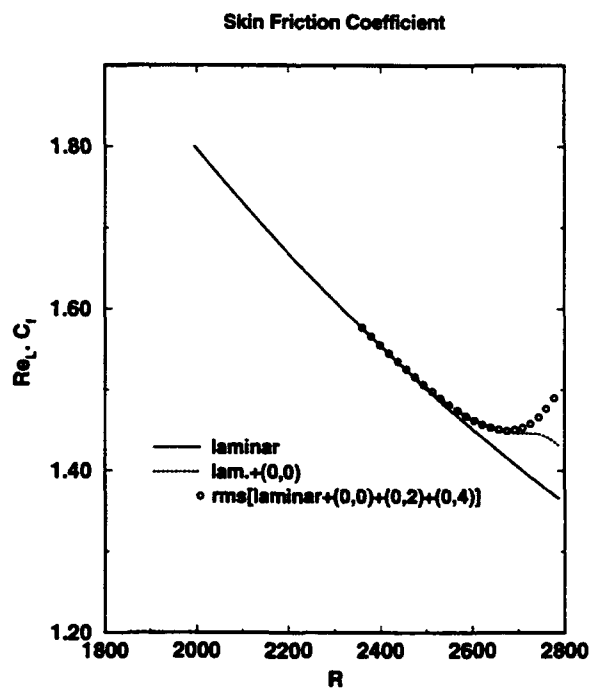


Figure 5.35: Nonlinear Interaction Between Two Oblique Second-Mode Waves: Mean Skin Friction Coefficient at the Wall.

Chapter 6

Concluding Remarks

An efficient method for predicting transition in high-speed flows over fairly general bodies has been developed. The major objectives set out in the contract have been achieved. Instead of having different codes for different problems, we have developed two codes which can perform two functions, the local linear stability analysis (LSH) and PSE analysis (PSH), and provide for physics interfaces to different problems. Interfaces for the flow over a flat plate and hypersonic flow over sharp and blunt cones are built in. The user's manual describes in detail how to set up new problems. The code has been extensively validated and used to study the stability of the compressible flow over a flat plate and hypersonic flows over sharp and blunt cones.

Most of the results obtained are consistent with existing theoretical and numerical results. Typical results for the flat plate boundary layer agree with those of Malik et al. (1990) and El-Hady (1991). Some of the calculations on hypersonic flows over the cone explains (partially) some observations in experiments. The results reveal the sensitivity of growth rates measured in experiments due to high nonparallel effects near the critical layer where the growth rate is typically measured. A downstream shift of the branch I neutral curve and branch II neutral points due to nonparallel effects is also apparent.

The appearance of harmonics of the fundamental second mode in experiments is simulated by both 2D and 3D nonlinear PSE calculations. The results show a rapid filling of the spectrum near breakdown at the end of the cone and saturation of the modes due to nonlinearity. These characteristics have been observed in sharp-cone experiments of Stetson et al (1983). The earlier decay of disturbances compared to the linear results, and, hence, the shift in branch II neutral point upstream (narrowing of unstable region) due to nonlinearity is also seen. The results indicate that transition over a blunt cone is most likely due to interaction of oblique second-mode disturbances. Similar nonlinear phenomena were observed in results on a sharp cone by Chang and Malik (1993).

The results of applications not only validate both method and code but also serve as examples for the user in solving new problems as described in the user's manual. In all applications, the PSE methodology has been found to be a useful and sound concept. Input models for nonlinear calculations still require more experience with receptivity and transition in high-speed flows. In contrast to the range of subsonic

speeds, studies on stability and transition at high speeds are currently more research than routine. While the development and utilization of the full capabilities of the PSE methodology will require some time and effort, the combination of the codes LSH and PSH is a major step toward an efficient tool for the engineers, researchers, and scientists to analyze and predict the transition process of high-speed flows over fairly general bodies.

Chapter 7

References

Bertolotti, F. P. 1991 "Linear and Nonlinear Stability of Boundary Layers with Streamwise Varying Properties," *Ph.D. Thesis*, The Ohio State University, Columbus, Ohio.

Bippes, H. and Müller, B. 1989 "Disturbance growth in an Unstable Three-Dimensional Boundary Layer," *Proc. 4th Symp. on Phys. and Num. Aspects in Aerodyn.*, Long Beach, CA, Jan.

Borisenko, A. I. and Tarapov, I. E. 1979 "Vector and Tensor Analysis with Applications." Translated from the Russian by R. A. Silverman. Published by Dover Publications, Inc., New York.

Chang, C. L., Malik, M. R., Erlebacher, G. and Hussaini, M. Y. 1991 "Compressible Stability of Growing Boundary Layers Using Parabolized Stability Equations," *AIAA-91-1636*.

Chang, C. L. and Malik, M. R. 1993 "Non-parallel Stability of Compressible Boundary Layers," *AIAA-93-2912*.

El-Hady, N. M. 1989 "Evolution of Resonant Triads in Three-Dimensional Boundary Layers," *Phys. Fluids A*, Vol. 1, No. 3, pp. 549-563.

El-Hady, N. M. 1991 "Spatial three-dimensional secondary instability of compressible boundary-layer flows," *AIAA J.*, Vol. 29, No. 5, pp. 688-696.

Esfahanian, V. 1991 "Computation and stability analysis of laminar flow over a blunt cone in hypersonic flows", *Ph.D. Thesis*, The Ohio State University, Columbus, Ohio.

Fischer, T. M., Hein, S. and Dallmann, U. 1993 "A Theoretical Approach for Describing Secondary Instability Features in Three-Dimensional Boundary-Layer Flows," *AIAA-93-0080*

Gregory, N., Stuart, J. T. and Walker, W. S. 1955 "On the Stability of Three-Dimensional Boundary Layers with Application to the Flow Due to a Rotating Disk,"

Phil. Trans. R. Soc. London, Vol. 248, pp. 155-199.

Herbert, T. 1991 "Boundary-Layer Transition - Analysis and Prediction Revisited," *AIAA-91-0737*.

Herbert, T. 1990 "Linear.x - A Code for Linear Stability Analysis," in *Instability and Transition*, Eds. M.Y. Hussaini and R.G. Voigt, pp. 121-144, Springer Verlag.

Kachanov, Y. S. and Trararykin, O. J. 1990 "The Experimental Investigation of Stability and Receptivity of a Swept Wing Flow," in: *Laminar-Turbulent Transition*, IUTAM Symp., Toulouse, France. Springer-Verlag

Kaups, K. and Cebeci, T. 1977 "Compressible Laminar Boundary Layers on Swept and Tapered Wings," *Journal of Aircraft*, Vol. 14, pp. 661-667.

Lancaster, P. and Salkauskas, K. 1988 "Curve and Surface Fitting - An Introduction." Academic Press Ltd., San Diego, CA 92101

Mack, L. M. 1975a "Linear Stability and the problem of supersonic boundary layer Transition" *AIAA J* vol. 13, pp.278-289

Mack, L. M. 1975b "A numerical Method for the Prediction of High-speed Boundary-layer Transition using Linear Theory," in: *Aerodynamic Analyses requiring Advanced Computers NASA SP-347*

Malik, M. R. 1990 "Numerical methods for hypersonic boundary-layer stability," *J. Comp. Phys.*, Vol. 86, pp 376-413.

Malik, M. R. and Li, F. 1992 "Three-Dimensional Boundary Layer Stability and Transition," *SAE 921991*.

Müller, B. and Bippes, H. 1988 "Experimental Study of Instability Modes in a Three-Dimensional Boundary Layer," *AGARD-CP-438*.

Rajendran, N. 1989 "Implementation of the Roe Upwind Algorithm in the AFWAL PNS Code," WRDC-TR-89-3108, Flight Dynamics Laboratory, Wright Research and Development Center, Air Force Systems Command, Wright-Patterson Air Force Base, Ohio 45433-6553.

Rizk, Y. M., Scott, J. N. and Newman, R. K. 1983 "Numerical Solution of Viscous Supersonic Flows in the Vicinity of Embedded Subsonic or Axially Separated Regions, User's Manual for the Three-Dimensional Viscous Nose Tip Code," AFWAL-TR-83-3113, Volume II, Flight Dynamics Laboratory, Wright Research and Development Center, Air Force Systems Command, Wright-Patterson Air Force Base, Ohio 45433-6553.

Smith, A. M. O. and Gamberoni, A. H. 1956 "Transition, Pressure Gradients and Suction," AGARD CP-224, Paper No. 6.

Stalnaker, J. F., Nicholson, L. A., Hanline, D. S. and McGraw, E. H. 1986 "Improvements to the AFWAL Parabolized Navier-Stokes Code Formulation," AFWAL-TR-86-3076, Flight Dynamics Laboratory, Wright Research and Development Center, Air Force Systems Command, Wright-Patterson Air Force Base, Ohio 45433-6553.

Stetson, K. F. and Kimmel, R. L. 1992 "On Hypersonic Boundary-Layer Stability," *AIAA-92-0737*

Stetson, K. F., Thompson, E. R., Donaldson, J. C. and Siler, L. G. 1984 "Laminar Boundary Layer Stability Experiments on a Cone at Mach 8, Part 1: Blunt Cone," *AIAA-83-1761*

Stetson, K. F., Thompson, E. R., Donaldson, J. C. and Siler, L. G. 1984 "Laminar Boundary Layer Stability Experiments on a Cone at Mach 8, Part 2: Blunt Cone," *AIAA-84-0375*

Stetson, K. F., Thompson, E. R., Donaldson, J. C. and Siler, L. G. 1985 "Laminar Boundary Layer Stability Experiments on a Cone at Mach 8, Part 3: Sharp Cone at Angle of Attack," *AIAA-85-0492*

Stuckert, G. K., Herbert, T. and Esfahanian, V. 1993 "Stability and Transition on Swept Wings," *AIAA-93-0078*.

Van Ingen, J. L. 1956 "A Suggested Semi-empirical Method for the calculation of the Boundary Layer Transition Region," Report UTHI-74, University of Technology, Dept. Aero. Eng.

Walatka, P. P., Buning, P. G., Pierce, L. and Elson, P. A. 1990 "PLOT3D User's Manual," *NASA Technical Memorandum 101067*, NAS Documentation Center, M/S 258-6, NASA Ames Research Center, Moffet Field, CA 94035-1000. Report UTHI-74, University of Technology, Dept. Aero. Eng.